

FILE COPY

4

**INVESTIGATION OF NEAR-SURFACE
CHEMICAL, PHYSICAL AND MECHANICAL
PROPERTIES OF SILICON CARBIDE
CRYSTALS AND FIBERS MODIFIED BY ION
IMPLANTATION**

**J. A. Spitsnagel and S. Wood
Materials Technology Division**

August 17, 1988

**Final Report
Contract No. N00014-85-C-0021**

**Office of Naval Research
Arlington, VA 22203**

AD-A200 613

**DTIC
ELECTE
S OCT 11 1988 D
D**

DISTRIBUTION STATEMENT A
Approved for public release
Distribution Unlimited



**Westinghouse R&D Center
1310 Beulah Road
Pittsburgh, Pennsylvania 15235**

88 9 19 005

88-9M4-SCIMP-R1

INVESTIGATION OF NEAR-SURFACE
CHEMICAL, PHYSICAL AND MECHANICAL
PROPERTIES OF SILICON CARBIDE
CRYSTALS AND FIBERS MODIFIED BY ION
IMPLANTATION

J. A. Spitznagel and S. Wood
Materials Technology Division

August 17, 1988



Accession For	
NTIS	<input checked="" type="checkbox"/>
DTIC	<input type="checkbox"/>
Unannounced	<input type="checkbox"/>
Justification	
By <i>per ltr</i>	
Distribution	
Availability Codes	
Date	
A-1	



Westinghouse R&D Center
1310 Beulah Road
Pittsburgh, Pennsylvania 15235

INVESTIGATION OF NEAR-SURFACE CHEMICAL, PHYSICAL
AND MECHANICAL PROPERTIES OF SILICON CARBIDE CRYSTALS
AND FIBERS MODIFIED BY ION IMPLANTATION

J. A. Spitznagel and S. Wood
Materials Technology Division
Westinghouse R&D Center
Pittsburgh, PA 15235

ABSTRACT

Modification of chemical, physical and mechanical properties of ceramic/semiconductor surfaces by ion implantation provides an opportunity to define and obtain desirable properties for a variety of applications. These include: interfaces in composite materials, electrical properties of devices and contacts, and specialized surfaces for optical waveguides, wear and corrosion resistance, etc. In this study, single crystals (6H), and whiskers of high purity silicon carbide were implanted with a variety of n- and p-type dopants (B, N, Al, P) an isovalent dopant (Ti), inert species (Ne) and hydrogen. Isochronal anneals at temperatures up to 1173 K permitted systematic evaluation of thermal effects in the implanted region. Implants fluences were normalized to permit comparisons on the basis of equal concentrations of displaced Si atoms for each ion. Microstructural, mechanical and chemical effects were studied by a series of RBS/channeling, TEM, SEM, microhardness, microtensile, AES, SIMS, and wetting (sputtered and molten metal) measurements. Recovery of crystalline structure during annealing is shown to be relatively independent of the implant species but depends upon the number of atomic displacements in the Si sublattice. Near-surface mechanical and chemical effects, however, are very dependent on the chemical/electrical nature of the implanted ions. Applications to ceramic/metal interfaces in metal matrix composites are discussed.

Aluminum phosphorus

→ (high) ←

CONTENTS

1. INTRODUCTION.....	1-1
2. EXPERIMENTAL APPROACH.....	2-1
2.1 Ballistic Considerations.....	2-1
2.2 Single Crystal Implantation Conditions.....	2-5
and Procedures	
2.3 Post-Implantation Analysis and Annealing.....	2-11
2.3.1 RBS/Channeling.....	2-13
2.3.2 Microhardness Measurements.....	2-13
2.3.3 Characterization by TEM, AES and SIMS.....	2-14
2.4 The Whisker Experiment.....	2-15
2.4.1 Implantation Procedures and Conditions.....	2-15
2.4.2 Post-Implantation Analysis of Whiskers.....	2-18
3. RESULTS AND DISCUSSION.....	3-1
3.1 Phase I: 300 K Nitrogen and Aluminum Implants.....	3-1
3.1.1 RBS/Channeling.....	3-1
3.1.2 Microhardness Measurements.....	3-7
3.1.3 Characterization by XTEM and AES.....	3-14
3.2 Phase II: Implantation Experiments.....	3-25
3.2.1 Hydrogen Effects.....	3-26
3.2.2 Residual Compressive Stresses.....	3-29
3.2.3 Donor, Acceptor, Isovalent Dopant Effects.....	3-34
3.2.4 Response to Composite Fabrication.....	3-47
3.3 Mechanical Properties and Wetting of Ion.....	3-49
Implanted SiC Whiskers	
4. SUMMARY AND CONCLUSIONS.....	4-1
5. ACKNOWLEDGMENT.....	5-1
6. REFERENCES	6-1

APPENDICES:

- A. Paper: Ion Beam Modification of 6H/15R SiC Crystals
- B. Paper: Surface Modification of SiC by Ion Implantation

LIST OF FIGURES

- Figure 1 — Macrophotographs of as-polished and cleaned single crystal 6H <0001> SiC used for ion-implantation.
- Figure 2 — Typical mounting arrangement for single crystal SiC on aluminum holders. The "n-i" and "i" regions refer to non-implanted and implanted, respectively.
- Figure 3 — Calculated damage energy per ion at the peak damage depth for various ions implanted into SiC at the energies indicated; EDEP - 1 Code.
- Figure 4 — Calculated damage energy per ion at the surface of SiC for various ions and energies indicated; EDEP - 1 Code.
- Figure 5 — Los Alamos whiskers mounted for ion implantation; a) as-received, b) after implanting with $8 \times 10^{16} \text{ Al}^+/\text{cm}^2$ at 150 keV. (Different lighting conditions were used.)
- Figure 6 — RBS/channeling spectra from N-implanted and annealed SiC.
- Figure 7 — RBS/channeling spectra from Al-implanted and annealed SiC.
- Figure 8 — Fraction of Si atoms displaced as a function of depth at different fluences for 75 keV N implants into 6H SiC <0001> at 300 K.
- Figure 9 — Fraction of Si atoms displaced as a function of depth at different fluences for 150 keV Al implants into 6H SiC <0001> at 300 K.
- Figure 10 — Knoop hardness of implanted and annealed SiC.
- Figure 11 — Knoop hardness of implanted and annealed SiC.
- Figure 12 — Knoop hardness of implanted and annealed SiC.
- Figure 13 — Knoop hardness of implanted and annealed SiC.

- Figure 14 — Microhardness indents obtained using a 50 g load on a SiC single crystal implanted with 2×10^{17} Al⁺/cm² at 150 keV. All indents are parallel to a [1210] direction:
a) as-implanted; b) after 573 K/0.5 h anneal; c) after 573 K/0.5 h + 893 K/0.5 h anneals; d) after 573 K/0.5 h + 893 K/0.5 h + 1233 K/0.5 h anneals.
- Figure 15 — SEM micrographs of microhardness indents in SiC single crystal using a 50 g load: a) as-implanted with 5×10^{17} N⁺/cm² at 75 keV; b) after 573 K/0.5 h anneal; c) after 573 K/0.5 h + 893 K/0.5 h anneals; d) after 573 K/0.5 h + 893 K/0.5 h + 1233 K/0.5 h anneals.
- Figure 16 — Plan view brightfield TEM micrograph and diffraction patterns of 6H <0001> SiC crystal as implanted with 7.7×10^{14} Al⁺/cm². Top) narrow crystalline layer at bombarded surface; Middle) amorphous implanted region; Bottom) crystalline region beyond R_p.
- Figure 17 — Cross-section TEM micrograph and diffraction patterns of 6H <0001> SiC crystal as-implanted with 5×10^{15} Al⁺/cm²; Top) 230 nm wide band of amorphous SiC extending to bombarded surface; Bottom) crystalline SiC beyond R_p.
- Figure 18 — Cross-section brightfield TEM image and diffraction patterns of 6H <0001> SiC crystal implanted with 1×10^{15} N⁺/cm² and annealed at 573 K/0.5 h + 893 K/0.5 h. Annealing has restored crystallinity in the damage zone.
- Figure 19 — Auger concentration profiles showing the distribution of Si, C, N, and O in specimen D149 μ1, Experiment #1, after implantation and annealing.
- Figure 20 — Auger concentration profiles showing the distribution of Si, C, N and O in the unimplanted side of specimen D149 μ1. Experiment #1.
- Figure 21 — Auger concentration profiles showing the distribution of Si, C, N and O in specimen D149 μ30. Experiment #2.
- Figure 22 — Auger concentration profiles showing the distribution of Si, C, N and O in the unimplanted side of specimen D149 μ30. Experiment #2.

- Figure 23 — RBS/channeling spectra of 6H SiC single crystals implanted with $5 \times 10^{15} \text{ Al}^+/\text{cm}^2$ and $5 \times 10^{15} \text{ Al}^+/\text{cm}^2 + 5 \times 10^{17} \text{ H}^+/\text{cm}^2$ at 300 K.
- Figure 24 — Cross-section TEM micrograph and diffraction patterns of 6H <0001> SiC crystal as-implanted with $5 \times 10^{15} \text{ Al}^+/\text{cm}^2$ plus $5 \times 10^{17} \text{ H}^+/\text{cm}^2$ at 300 K; Top) 260 nm wide band of amorphous SiC extending to bombarded surface; Bottom) crystalline SiC beyond R_p .
- Figure 25 — RBS/channeling spectra for two 6H SiC crystals implanted with either $5 \times 10^{15} \text{ Al}^+/\text{cm}^2$ or $5 \times 10^{15} \text{ Al}^+/\text{cm}^2 + 5 \times 10^{17} \text{ H}^+/\text{cm}^2$ after annealing at 1173 K-0.5 h.
- Figure 26 — RBS/channeling spectra from Ne^+ implanted and annealed SiC.
- Figure 27 — Knoop microhardness measurements of Ne^+ , B^+ , P^+ and Ti^+ implanted and annealed 6H SiC.
- Figure 28 — RBS/channeling spectra from P^+ , B^+ or Ti^+ implanted (300 K) 6H SiC and non-implanted (n-i) masked portion of one of the crystals.
- Figure 29 — RBS/channeling spectra from P^+ implanted and annealed SiC.
- Figure 30 — RBS/channeling spectra from B^+ implanted and annealed SiC.
- Figure 31 — RBS/channeling spectra from Ti^+ implanted and annealed SiC.
- Figure 32 — Temperature dependence of damage recovery calculated from integration over the area under the Si direct back-scattering peak for B^+ , P^+ and Ti^+ implantation.
- Figure 33 — Temperature dependence of damage recovery calculated from integration over the area under the Si direct back-scattering peak for Al^+ and N^+ implantation at different fluences.
- Figure 34 — Comparison of RBS/channeling spectra from Al^+ implanted 6H SiC crystals subjected to isothermal vacuum annealing or metal matrix composite fabrication (hot pressing) thermomechanical cycle.

- Figure 35 — Morphology variability in as-received Los Alamos whiskers.
- Figure 36 — Los Alamos VLS SiC whisker (unimplanted) with as-deposited 100 nm thick Al film (plan view).
- Figure 37 — Los Alamos VLS SiC whisker (unimplanted) with 100 nm Al film after 973 K-0.5 min vacuum anneal. a) plan view; b) 50° tilt.

LIST OF TABLES

- Table 2.1 Projected range, straggling and peak damage depth for various ions incident on SiC at 50, 100, 150 and 300 keV.
- Table 2.2 Implantation conditions and calculated fluences for Phase I experiments based on achieving amorphization at $S_D(x) = 10^{21} \text{ keV/cm}^3$.
- Table 2.3 Parameters for Phase II implantation experiments.
- Table 2.4 Whisker implantation parameters.
- Table 2.5 Calculated temperature rise in SiC whiskers during ion implantation.
- Table 3.1 Calculated maximum fraction of kinetic energy transferred in "Hard-Sphere" collisions of an ion of mass M_1 with silicon and carbon atoms.
- Table 3.2 Calculated average concentrations of implanted solute.

1. INTRODUCTION

This program was initiated because of the need for an improved basic understanding of reinforcement phase/matrix interfaces in metal or ceramic matrix composite systems. Metal composites (MC) generally require a strong interfacial zone to ensure stress transfer between fiber and matrix. Unfortunately, such interfacial strength is often accompanied by low ductility, toughness, impact strength and crack propagation resistance. In ceramic composites (CC), the key to increased toughness has been related to low strength in the fiber-matrix interfacial zone. This permits extensive fiber pullout and frictional sliding of the fiber along the matrix. Thus, in both types of composite systems, the understanding and ability to control the structure and properties of interfacial zones is critical to achieving optimum composite properties.

Ion beam modification of surface properties, which is a rapidly expanding technology that has been and will continue to be applied to many engineering materials, is an ideal way of tailoring near surface structure and chemistry. Many of the early studies in metals and ceramics, however, focused on empirical material behavior after ion implantation, such as the tribological properties, rather than attempting a full understanding of the microstructural and microchemical changes. Nevertheless, these empirical successes were the primary driving force for the emergence of commercial implantation facilities which have facilitated many real engineering applications.

The focus of the present study was to use ion implantation as the basis for selectively tailoring the surface properties of single crystal silicon carbide and to investigate the microstructural and microchemical mechanisms responsible for the observed mechanical property changes. Earlier work by the High Energy Ion Beam Studies (HEIBS) group at Westinghouse and the University of Pittsburgh and,

independently by workers at Cambridge University, which demonstrated surface mechanical changes in brittle materials, was used as the foundation for the work described herein. Implant species, energies and fluences were selected in part, based upon past history, but also based on chemistry and ballistic considerations, as more specifically detailed in Section 2.1. Post-implant anneals were employed to evaluate material recovery and/or stability. Principal diagnostic techniques employed were RBS/channeling to investigate damage structures, and microhardness to characterize mechanical behavior changes. These techniques were further augmented by transmission electron microscopy (TEM), auger electron spectroscopy (AES) and secondary ion mass spectroscopy (SIMS). The data derived from the single crystal experiments were subsequently used to select parameters for the Los Alamos whisker implantations.

The results (Section 3) clearly demonstrate that the surface mechanical properties are altered by ion implantation and that the behavior is dopant dependent. These findings are discussed in relation to interfaces in metal matrix composites.

2. EXPERIMENTAL APPROACH

2.1 BALLISTIC CONSIDERATIONS

The physics of damage production and chemical doping of solid materials by energetic ions has been discussed in numerous texts.⁽¹⁻³⁾ In this section, we describe only briefly the ballistic effects which impacted the selection of ion implantation conditions (ion species, energy, flux and fluence) in the present investigation.

As an energetic ion traverses a solid target, it loses energy through frictional effects due to electronic interactions and elastic collisions with atoms in the solid. The total path length traveled by the incident ion before it comes to rest may be calculated from integral equations first derived by Lindhard, Scharff and Schiott⁽⁴⁾ and incorporated into the "LSS computer code" by Gibbons.⁽⁵⁾ The parameter of experimental interest is usually not the total path length but rather the projection of the total path length in the direction normal to the implanted surface. A monoenergetic beam of ions with energy E_0 incident on the solid will thus come to rest at a depth corresponding to the mean projected range, R_p .

For most combinations of ion and target, the actual distribution of implanted ions is approximately Gaussian-centered at a depth R_p with a root mean square straggle or ΔR_p . Table 2.1 gives some typical values of R_p and ΔR for several ions of different mass and energy incident on silicon carbide. For the ions and ion energies of interest to the proposed study, R_p is typically 0.03 μm to 0.6 μm and ΔR_p is on the order of 10 to 20% of the mean projected range. The average concentration of implanted solute is given approximately by:

$$[\text{solute}] = \frac{\psi}{2.35 \Delta R_p} = \text{atoms/cm}^3 \quad (2-1)$$

where Ψ = ion fluence measured by ions/cm². While the concentration profile and the extent of the doped region can be altered either by changing the angle of incidence of the ion beam during implantation or by performing multiple implants using ions of different energies,⁽⁶⁾ only monoenergetic beams at normal incidence were used in this investigation. For the whiskers, however, which have curved surfaces (circular cross-sections), this implicitly means that the implant was not at a uniform depth around the entire whisker surface. This is briefly discussed further in Section 2.4.

The elastic collisions of the incident ion with atoms of the solid can result in a large number of atoms being irreversibly displaced from their lattice sites. Most of the atomic displacement damage results from collisions of energetic PKA's (primary knock-on atoms) with neighboring atoms of the solid.⁽⁷⁾ A PKA is an atom of the solid that receives its energy by a direct collision with the incident ion and dissipates its energy in a shower of secondary binary collisions with adjacent atoms in the solid. These events occur on the fast collision time scale ($\sim 10^{-14}$ to 10^{-13} seconds) and lead to highly localized damage regions (cascades). In metallically bonded materials, the cascades are vacancy rich regions which can collapse to produce dislocation loops or voids. Only $\sim 1\%$ of the Frenkel pairs survive recombination in metals because of low interstitial atom migration energies and the non-directional bonding.

In covalently bonded ceramics such as silicon or silicon carbide, the results are much more complex. For energy transfers greater than ~ 15 eV per atom, the experimental evidence suggests that the highly localized damage zones may become amorphous.⁽⁸⁾ The very strong, directional bonds are difficult to re-establish for implantation temperatures of $T \leq 800$ K. Extensive post-implantation annealing at elevated temperatures is required to restore crystallinity. This is a key point in ion beam modification of ceramic materials for composite reinforcement.

Table 2.1
PROJECTED RANGE, STRAGGLING AND PEAK DAMAGE DEPTH FOR VARIOUS
IONS INCIDENT ON SiC AT 50, 100, 150 AND 300 keV.

<u>Ion</u>	<u>E_o (keV)</u>	<u>R_p (μm)</u>	<u>ΔR_p (μm)</u>	<u>X_m (μm)</u>
B	50	.1309	.0337	.0920
	100	.2502	.0489	.2000
	150	.3543	.0579	.3000
	300	.6104	.0718	.5490
C	50	.1081	.0292	.0740
	100	.2105	.0438	.1640
	150	.3018	.0529	.2500
	300	.5300	.0675	.4640
N	50	.0918	.0255	.0580
	100	.1823	.0398	.1358
	150	.2652	.0492	.2150
	300	.4770	.0650	.4160
Ne	50	.0618	.0176	.0330
	100	.1268	.0297	.0840
	150	.1903	.0388	.1400
	300	.3639	.0564	.3000
Al	50	.0461	.0127	.0210
	100	.0948	.0223	.0560
	150	.1446	.0303	.0960
	300	.2890	.0477	.2250
Si	50	.0428	.0117	.0190
	100	.0876	.0208	.0500
	150	.1339	.0284	.0870
	300	.2692	.0452	.2050
P	50	.0397	.0106	.0160
	100	.0809	.0189	.0440
	150	.1238	.0260	.0780
	300	.2516	.0424	.1850
Ar	50	.0330	.0080	.0117
	100	.0659	.0144	.0330
	150	.1005	.0202	.0580
	300	.2078	.0346	.1440
Ti	50	.0278	.0063	.0077
	100	.0541	.0112	.0240
	150	.0816	.0158	.0420
	300	.1681	.0278	.1080

The fluence required to obtain complete overlap of the localized amorphous zones depends on the mass and energy of the incident ion and the implantation temperature. For room temperature implantation of silicon carbide, for example, a fluence of $\sim 10^{15}$ ions/cm² is required for ions of mass ~ 14 to 75 amu, at energies of ~ 50 keV to 200 keV, to obtain an amorphous zone. This fluence was selected as one of the benchmark fluences for the Phase I experiment described in Section 2.2. It has been shown previously⁽⁹⁾ that different combinations of ion masses and energies (and temperatures) can produce the same damage levels and damage profiles, but with different chemical dopant concentrations. Thus, it is possible to independently vary (and study) the effects of atomic displacement damage and compositional changes from the implanted ions in single element ceramics such as silicon. This is not generally true for compounds such as SiC where ions of different masses occupy different sublattices. The atomic displacement processes depend on the relative masses of the incident ion and target atom through a relation of the form $T = (4M_1M_2)/(M_1 + M_2)^2$ where T = the fractional energy of an ion of mass M_1 that can be transferred to a target atom of mass M_2 . Thus, in silicon carbide, for example, an incident Al ion will give up a larger fraction of its energy to a silicon atom than to a carbon atom. The result, as observed in a number of compounds, is to produce highly localized changes in stoichiometry. Luminescence data often show evidence of a high proportion of C-C bonds (graphitic regions) in ion bombarded SiC, for example.⁽¹⁰⁾

If the atomic mobility is sufficiently high, the displaced atoms and vacancies may condense to form dislocation loops, voids, or solute-defect features which can appear to be nonequilibrium phases.⁽¹¹⁾ All of these effects can have an impact on the mechanical and chemical properties of the ion beam modified surface. Dislocations can provide unexpected plasticity; voids will alter the effective modulus; and the presence of new phases can either harden or soften, embrittle or toughen the affected region.

These factors were all considered in the selection of implantation conditions described in Section 2.2.

2.2 SINGLE CRYSTAL IMPLANTATION CONDITIONS AND PROCEDURES

For the Phase I experiments, aluminum and nitrogen ions were selected as the bombarding species in part because previous work had shown that nitrogen implantation could introduce near surface plasticity in silicon and silicon carbide⁽¹²⁻¹⁵⁾ while aluminum implantation modified crack propagation behavior in silicon.^(14,15) Additionally, Al and N are p- and n-type dopants, respectively, in SiC. As discussed in Section 2.1, Al is expected to more efficiently damage the Si sublattice whilst N should be more efficient in displacing carbon.

Silicon carbide <0001> crystals were selected from the D149 and D143 sublimation growth run samples, shown in Figure 1, and determined by transmission Laue patterns to be mixed polytype but mostly 6H SiC. These samples are completely transparent, but slightly yellow in color. Those utilized for RBS/channeling measurements were approximately 1 cm x 0.5 cm and 1 mm thick. They are compensated, slightly n-type, with an impurity concentration of $\sim 5 \times 10^{17}/\text{cm}^3$. Crystal faces were lapped flat and parallel to the (0001) plane. For the Phase I experiments, the face utilized for the implantation experiments had a 0.1 μm diamond finish. This surface was further modified for Phase II experiments by an oxidation and acid stripping process to remove any residual damaged layer left after the final diamond polish. Separate transmission electron microscopy (TEM) specimens were cut to approximately 2.5 mm x 2.5 mm and were ≤ 1 mm thick. No polishing and grinding procedures were performed on these samples. All crystals were cleaned thoroughly in HF followed by distilled water and solvent rinses prior to implantation.

Reference samples for the channeling studies were provided by placing a tantalum mask over $\sim 1/3$ specimen surface during implantation. TEM specimens were not masked. Implants were made at ~ 300 K and at a pressure of 1.3×10^{-5} Pa with a 200 kV implanter equipped with post acceleration magnetic mass separation. Current densities were $0.5 \mu\text{A}/\text{cm}^2$ and $0.25 \mu\text{A}/\text{cm}^2$ for N and Al, respectively. A typical specimen configuration is shown in Figure 2 for specimen D149 $\mu 30$.

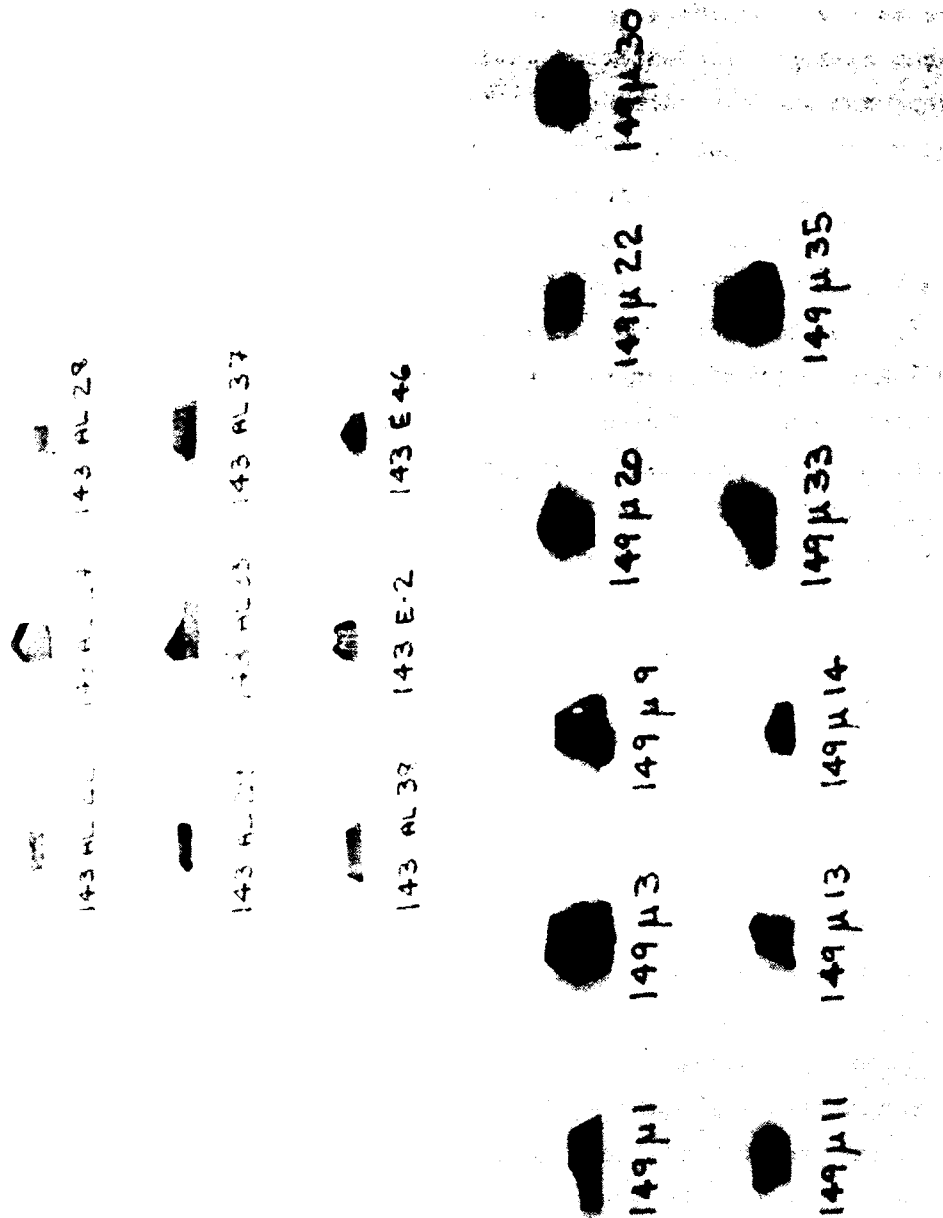


Figure 1 — Macro photographs of as-polished and cleaned single crystal 6H <0001> SiC used for ion-implantation.

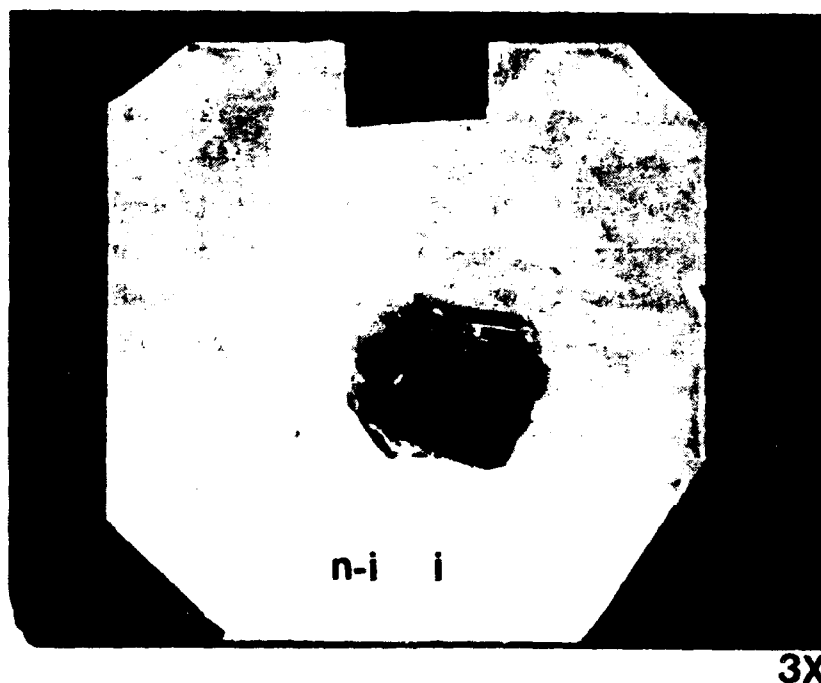


Figure 2 — Typical mounting arrangement for single crystal SiC on aluminum holders. The "n-i" and "i" regions refer to non-implanted and implanted, respectively.

Implantation conditions and calculated fluences are listed in Table 2.2. Accelerating voltages for the N and Al ions were chosen to produce peak damage at a depth of approximately 0.1 μm . The calculation of deposited damage energy and the amorphization criterion for SiC are discussed extensively by Spitznagel et al., in reference 16 which is included in full in Appendix A. A more abbreviated discussion is presented here. Figures 3 and 4 show the damage energy, $S_D(x)$, for various ions implanted into SiC as a function of incident ion energy. The curves were calculated using a modified version of the EDEP-1⁽⁵⁾ code. The damage energy (energy loss due only to atomic displacements) is shown for the surface ($x=0$) and the peak damage depth ($x=x_m$). The calculated $S_D(x)$ curves were used to determine the fluences of 75 keV N^+ and 150 keV Al^+ required to produce equal numbers of displaced atoms in the SiC crystals at a peak damage depth of 0.1 μm . The resultant fluences represent different concentrations of implanted dopant and slightly different values of projected range, R_p . Based on previous results,⁽¹⁶⁾ a critical deposited damage energy of $2 \times 10^{21} \text{ keV/cm}^3$ was used to estimate the fluences of N and Al ions required to produce an amorphous region at x_m and an amorphous zone extending from x_m to the front surface using the following equation:

$$\text{Critical Fluence} = \frac{2 \times 10^{21} \text{ keV/cm}^3}{S_D(x) \times 10^7} \quad (2-2)$$

where $S_D(x)$ is given by Figures 3 and 4.

Table 2.2 summarizes these calculated values and the additional fluences chosen to produce doping beyond complete amorphicity and a damaged but crystalline microstructure for each ion. These are the fluences selected for the Phase I experiment. In a second series of implantation experiments, designated as Phase II, the implantation conditions and species listed in Table 2.3 were utilized. The footnotes indicate specific reasons for the selection of parameters and species. These experiments were both a direct extension of the Phase I nitrogen

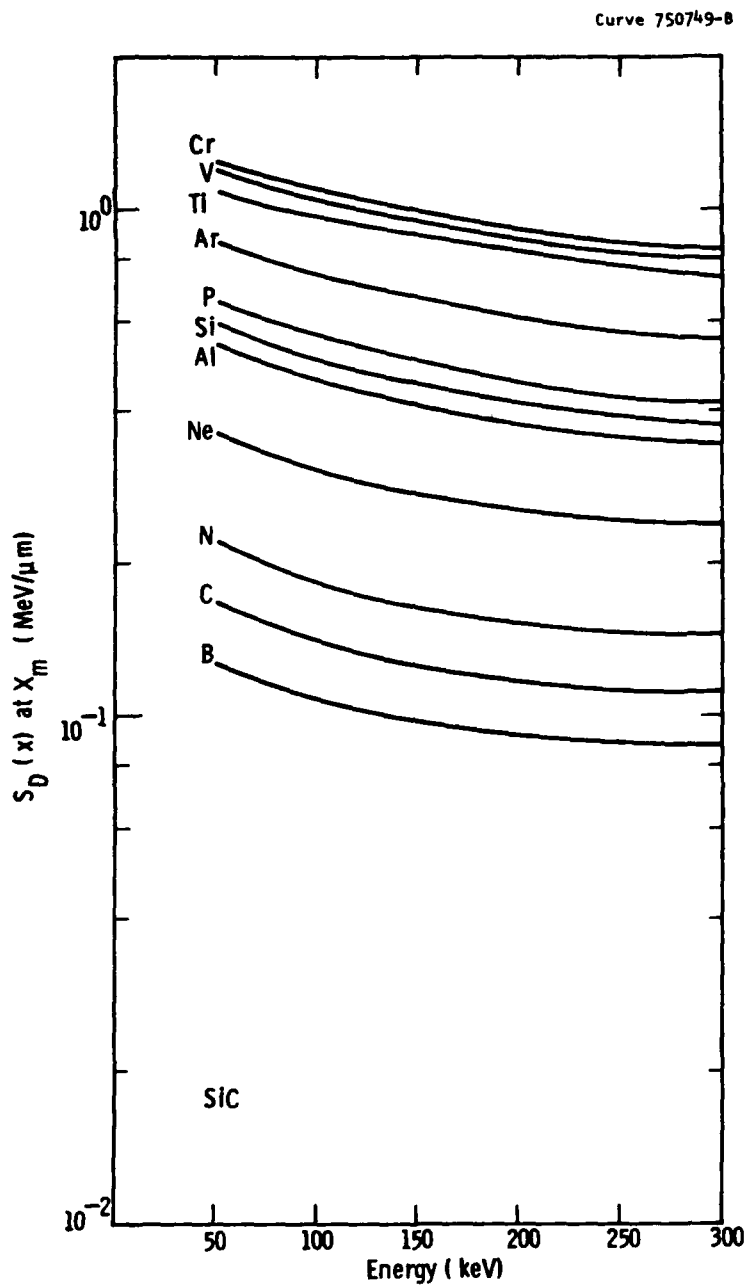


Figure 3 — Calculated damage energy per ion at the peak damage depth for various ions implanted into SiC at the energies indicated; EDEP - 1 Code.

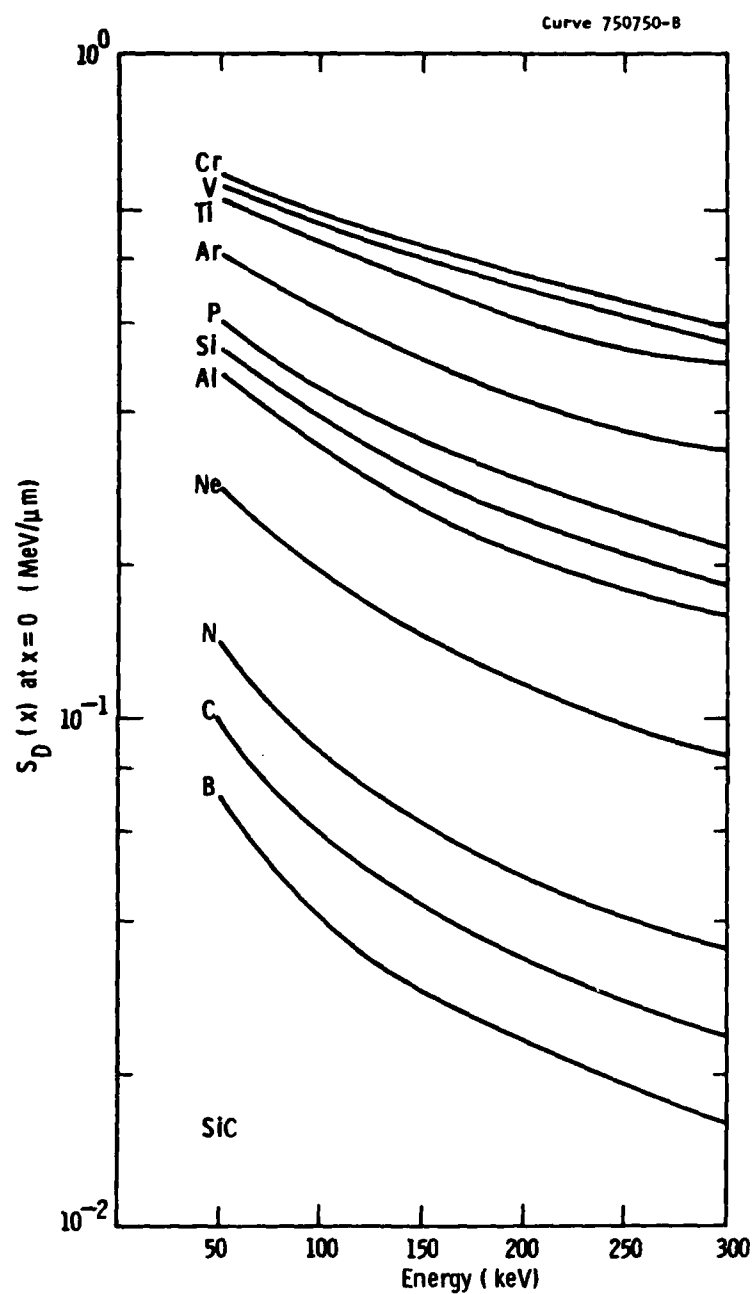


Figure 4 — Calculated damage energy per ion at the surface of SiC for various ions and energies indicated; EDEP - 1 Code.

and aluminum ion work and a broader based ion/dopant scoping study. Implants were also designed to address a) whether surface softening is due entirely to residual compressive stresses or is dopant related; and b) the impact of annealing with applied pressure on amorphous layer regrowth.

Table 2.2
IMPLANTATION CONDITION AND CALCULATED FLUENCES FOR PHASE I
EXPERIMENTS BASED ON ACHIEVING AMORPHIZATION AT
 $S_D(x) = 10^{21} \text{ keV/cm}^3$

Condition	Fluence (ions/cm ²)	
	Nitrogen	Aluminum
No Amorphicity	5×10^{14}	1×10^{14}
Amorphous at Peak Damage Depth ($x = x_m$)	1×10^{15}	4.9×10^{14}
Amorphous from Peak Damage Depth to Surface	1.9×10^{15}	7.7×10^{14}
Beyond Amorphicity	1×10^{16}	5×10^{15}

All ion fluences and energies were chosen to permit direct comparison with Phase I results based on fluences of Al and N ions required to produce amorphous SiC from x_m to the surface. All implants (Phases I and II) were performed at ~300 K.

2.3 POST-IMPLANTATION ANALYSIS AND ANNEALING

Following implantation, all masked (i.e., non TEM) SiC crystals were investigated by RBS/channeling and microhardness, as discussed in more detail below. Post-implantation annealing was performed sequentially on each crystal at 573-1233 K in a vacuum furnace at a pressure of 2.7×10^{-4} Pa. The temperature range was selected to span possible processing temperatures for a variety of metal matrix composite alloys. All crystals were analyzed by RBS/channeling and microhardness measurements after each anneal stage to follow damage recovery and its impact on the surface hardness. Selected TEM specimens were also subjected to various annealing stages. A few, carefully selected,

crystals were also analyzed by either Auger electron spectroscopy (AES) or secondary ion mass spectroscopy (SIMS), after the final annealing stage.

Table 2.3
PARAMETERS FOR PHASE II IMPLANTATION EXPERIMENTS

<u>Experiment</u>	<u>Ion</u>	<u>Fluence</u> <u>ions/cm²</u>	<u>Energy</u> <u>keV</u>	<u>Reason</u>
1	N ⁺	5 x 10 ¹⁷	75	(a)
2	Al ⁺	2 x 10 ¹⁷	150	(a)
	Al ⁺	5 x 10 ¹⁵	150	
3	plus protons	5 x 10 ¹⁷	20	(b)
4	Ne ⁺	7 x 10 ¹⁵	135	(c)
5	B ⁺	3 x 10 ¹⁵	50	(d)
6	P ⁺	9 x 10 ¹⁴	150	(d)
7	Ti ⁺	5 x 10 ¹⁴	250	(d)
8	Al ⁺	5 x 10 ¹⁵	150	(e)

- (a) Extend Phase I study to examine high fluence effects and compare with Cambridge results.
- (b) Determine whether "passivation" of Si bonds in amorphous-SiC by hydrogen affects regrowth of amorphous layer as has been observed in Si crystals.
- (c) Determine whether softening is due solely to residual compressive stresses.
- (d) Determine whether the electronic nature of the dopant (n-type, p-type, isovalent) affects the regrowth of the amorphous layer.
- (e) Determine whether annealing under point contact or hydrostatic pressure affects the regrowth of the amorphous layer as has been observed for Si.

2.3.1 RBS/Channeling

All RBS/channeling studies were performed at the University of Pittsburgh in the HEIBS laboratory. A 1.5 MeV He beam from a 2 MV Van de Graaff was used to conduct these experiments. Beam currents were normally 15 nA and the spot size was 0.8 mm, with a beam divergence of < 0.03 degrees. RBS measurements were made at 168° . Each RBS spectrum obtained from an implanted or implanted and annealed crystal was directly compared with a spectrum from the corresponding non-implanted portion of the crystal. The as-implanted specimen mounting configuration (Figure 2) was, in all cases, used for RBS measurements. For annealing studies, specimens were demounted for the anneal stage, and subsequently remounted for RBS/channeling studies.

2.3.2 Microhardness Measurements

Hardness indentations were obtained on a Tukon hardness tester calibrated for loads ≥ 10 g. A Knoop indenter was used with loads of 10-300 g. Initial measurements on as-polished crystals indicated no significant orientation dependence of the hardness so, for Phase I samples, no fixed orientation was maintained. An additional check was performed on D149 μ -33 (5×10^{15} Al/cm²) after annealing at 1173 K /0.5 h by taking measurements with the long diagonal of the indenter parallel to the $\langle 10\bar{1}0 \rangle$ and $\langle 1\bar{2}10 \rangle$ directions, but no hardness differences were detected. Actual Knoop Hardness Number (KHN) were calculated from micrographs of the indents taken on a Reichert optical microscope at 1000x under constant illumination conditions by the same operator. Indents were too small to be accurately measured with the microscope/filar eye piece attachment on the Tukon tester. Most data are reported showing representative standard deviations. Indentations were always placed towards the edge of the specimen so that adequate indent-free area remained for RBS experiments.

Despite the orientation independence observed in the Phase I sample measurements, Phase II hardness indents were consistently measured parallel to a $[1210]$ facet.

2.3.3 Characterisation by TEM, AES and SIMS

Preparation of cross-section TEM samples was as follows: a ~100 nm thick layer of SiO_2 was evaporated onto the surface of each 2.5 mm x 2.5 mm square sample. The samples were then mounted in a low viscosity embedding medium, cured, and ground and polished to produce wafers ~0.1 mm thick. Subsequent dimpling produced a center portion which was ~50 μm thick. Final thinning to obtain electron transparent regions was achieved by ion milling with 6 KeV Ar ions. Due to excessive edge milling effects in some samples, planar specimens were also prepared by thinning from the backside to the implanted surface using a procedure essentially identical to that used for cross-sections, apart from the use of a single ion gun in the milling process. All TEM studies were performed on a Philips 400T electron microscope operating at 120 kV.

Selected samples (i.e., large crystals) were examined by AES, after their final annealing stage, according to the following procedure. A Physical Electronics Scanning Auger Spectrograph was used for all analyses. After recording the auger electron spectrum from the as-implanted surface, subsequent spectra were recorded after successive sputtering times (usually 1 min intervals). Composition profiles were thus determined by calculating relative atomic % values (using previously determined sensitivity factors) versus depth for each element of interest. The sequential sputtering process was continued until only the stoichiometric SiC composition was obtained in the spectrum (usually at a depth ~300 nm). A 5 kV Ar beam was used for sputtering. Comparative depth profiles were obtained in a similar fashion from the non-implanted portion of each SiC crystal.

The AES characterization described above was feasible only on samples implanted with ion fluences high enough to produce a doping concentration measurable by AES (i.e., significantly above the detection limit). Several other specimens, implanted with lower fluences were submitted to the Physical Electronics Laboratory for SIMS profiling analyses. Most data were obtained using a negative primary ion beam (O^-)

since the elements of interest are electropositive. Concentration profiles were obtained to depths $\geq R_p$ (projected range of implanted species).

2.4 THE WHISKER EXPERIMENT

This experiment was designed to ion implant a number of Los Alamos supplied SiC whiskers with various dopants. The particular ion species, fluences and energies were selected based on results from the Phase I and II experiments so that direct comparison of whisker and single crystal behavior could be made. Justification for these selections is discussed in Section 3.

2.4.1 Implantation Procedures and Conditions

Prior to performing the actual ion implantation, a scheme had to be devised for mounting individual whiskers for insertion into the accelerator. Macrophotographs of a typical specimen configuration are given in Figure 5 which shows one particular sample mount before and after implantation. Indium strips were heated to their melting temperature on an aluminum substrate flashed with gold. The bond developed between the indium and Au/Al was sufficient to ensure good thermal and electrical conduction during implantation. Each whisker was then individually mounted into slots cut into the indium and held securely in place by mechanically pressing indium to fill each slot. As shown in Figure 5, a maximum of 16-18 whiskers were mounted on each holder. The whiskers were mounted over a 1 cm diameter hole (magnitude determined by the accelerator beam size) to permit implantation from both sides of the mount. Thus, although the resulting implanted ion depth is not uniform around the whisker cross-section (since implantation is a line of sight process), all radial directions have received some concentration of implanted species. Four specimen mounts were prepared and implanted according to the parameters listed in Table 2.4.

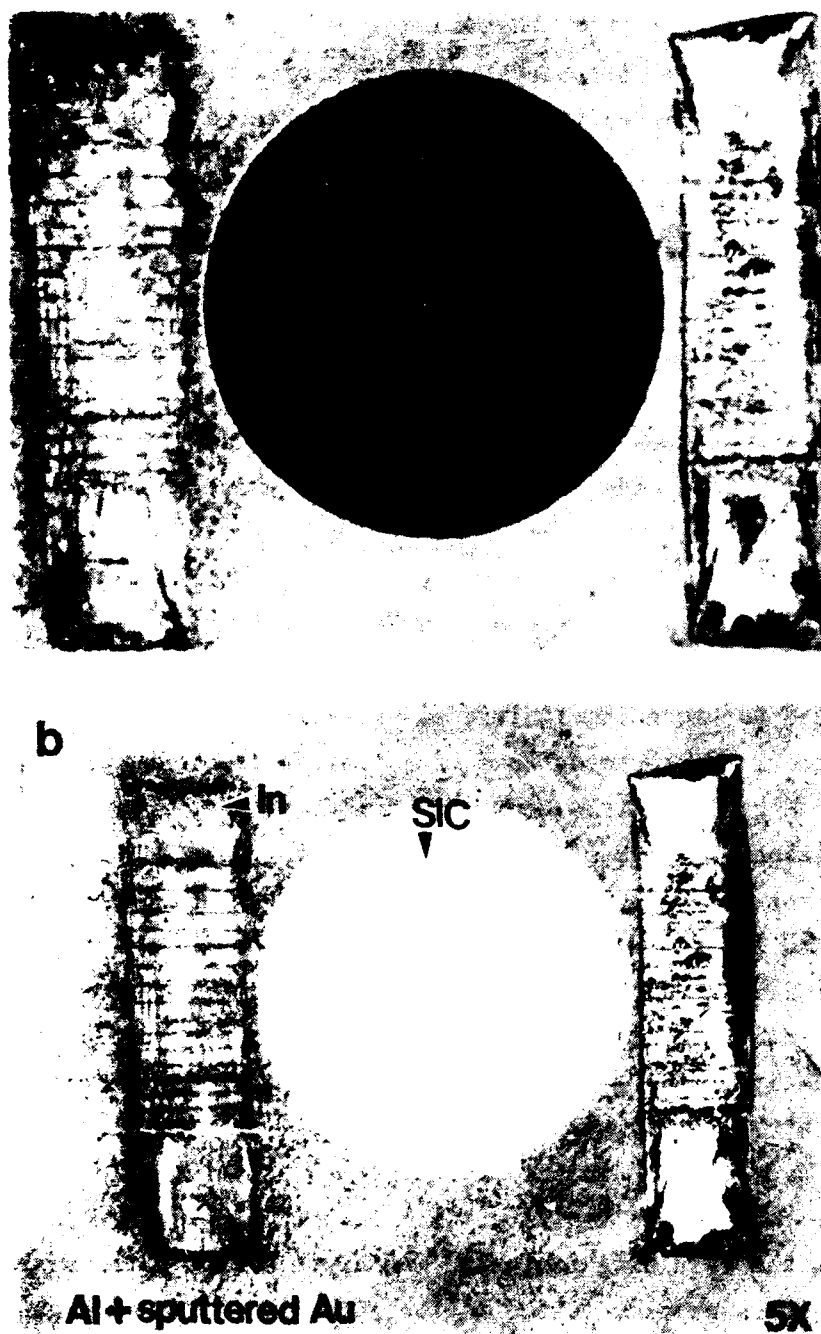


Figure 5 — Los Alamos whiskers mounted for ion implantation; a) as-received, b) after implanting with $8 \times 10^{16} \text{ Al}^+/\text{cm}^2$ at 150 keV. (Different lighting conditions were used.)

Table 2.4
WHISKER IMPLANTATION PARAMETERS

<u>Mount Designation</u>	<u>Fluence</u>	<u>Ion Energy</u> <u>keV</u>	<u>Incident</u> <u>Energy Flux</u> <u>J·s⁻¹cm⁻²</u>
#1	$3 \times 10^{15} \text{ B}^+/\text{cm}^2$	50 keV	1.9
#2	$9 \times 10^{14} \text{ P}^+/\text{cm}^2$	150 keV	13.2
#3	$8 \times 10^{16} \text{ Al}^+/\text{cm}^2$	150 keV	5.6
#4	$2.5 \times 10^{17} \text{ N}_2^+/\text{cm}^2$	150 keV (a)	197.0

(a) Equivalent to a fluence of $5 \times 10^{17} \text{ N}^+/\text{cm}^2$ implanted at 75 keV since N_2 molecule dissociates upon impact.

Despite the rather elaborate mounting procedure outlined here, there was considerable concern about the rise in temperature in individual whiskers during ion bombardment. Hence, modeling calculations were performed to assess the upper limit of incident ion energy deposition rate which would permit a "reasonable" time for ion implantation but not produce an unacceptable rise in temperature. The goal for this latter parameter was set at 873 K maximum, based on typical MC processing temperatures. Assuming an emissivity of 1.0 or 0.5, together with published values of the density, thermal conductivity and heat capacity of SiC, the maximum temperature of a SiC whisker was calculated for incident energy fluxes of 60 and 600 $\text{J} \cdot \text{s}^{-1} \text{cm}^{-2}$. The results are tabulated in Table 2.5 for whisker diameters of 3 and 10 μm (typical of those used for the implantation experiment). The worst case prediction is for a 3 μm diameter whisker which will experience a maximum temperature of 977 K at its center (L/2) for an incident energy flux of 600 $\text{J} \cdot \text{s}^{-1} \text{cm}^{-2}$. Table 2.4 shows that for most implants, the actual deposited energy was $< 60 \text{ J} \cdot \text{s}^{-1} \text{cm}^{-2}$ and that, even for the

nitrogen implant was only $197 \text{ J}\cdot\text{s}^{-1}\text{cm}^2$. Thus, it was concluded that these experimental conditions did not produce an unacceptable temperature rise.

2.4.2 Post-Implantation Analysis of Whiskers

The primary objectives of ion-implanted SiC whisker analysis were to determine: 1) mechanical strength, and 2) wettability compared to unimplanted, virgin material. Pursuit of the first objective is beyond the scope of the present study. Several whiskers from each implantation experiment listed in Table 2.4 have been forwarded to Los Alamos National Laboratory so that mechanical property measurements can be performed. These data will be reported separately at some later date.

The wettability was addressed as part of this investigation in the following manner. Several implanted whiskers were removed from each mount by "clipping" close to the indium. They were subsequently remounted on 304 SS sheets (approximately 2.5 cm wide x 7.6 cm long x 0.15 cm thick), in grooves, with small dots of Saueriasen refractory cement. These whiskers were handled with great care so that only the ends came into contact with the metal tweezers. After a 24 hour cure for the cement, the entire assembly was submerged in a crucible filled with molten 2024 Al alloy held at 973 K. Dipping time was ~10 sec. After removal, and cooling, the aluminum coated sample was transverse sectioned, mounted and metallographically polished to evaluate the wetting behavior. Comparative dipping experiments were performed on unimplanted whiskers.

Table 2.5
CALCULATED TEMPERATURE RISE IN SiC WHISKERS
DURING ION IMPLANTATION

Incident Energy Flux $\text{J} \cdot \text{s}^{-1} \text{cm}^{-2}$		Maximum Temperature*, at L/2	
		3 μm Diameter Whisker	10 μm Diameter Whisker
A	60	386 K	330 K
	600	862 K	583 K
B	60	395 K	331 K
	600	977 K	599 K

A - Emissivity = 1.0

B - Emissivity = 0.5

* Assuming that the anchored whisker ends were maintained at 300 K, the maximum temperature rise occurs at the center of the whisker; i.e., at L/2.

3. RESULTS AND DISCUSSION

3.1 PHASE I: 300 K NITROGEN AND ALUMINUM IMPLANTS

3.1.1 RBS/Channeling

These data have been discussed in detail in previously published papers, references 16 and 17 included in full in Appendices A and B. RBS spectra for aligned, unimplanted (n-i), implanted and annealed specimens are given in Figures 6 and 7 for the nitrogen and aluminum implants, respectively. The observed backscattering is determined entirely by the distribution of displaced Si/C atoms since the concentrations of implanted atoms are small ($< 1 \text{ At\%}$) and make a negligible contribution to the number of backscattered ions. Following the procedure detailed by Spitznagel et al.,⁽¹⁶⁾ the number of displaced Si atoms per unit volume $N_D(x)$ was determined and is plotted in normalized fashion as a function of depth in Figures 8 and 9. The divisor $N_{\text{SiC}}^{\text{Si}}$ is the density of Si atoms in the SiC lattice. These data indicate several important points. Firstly, the nitrogen fluence required to reach the random yield, $N_D(x)/N_{\text{SiC}}^{\text{Si}} = 1$, at $x = x_m$ agrees well with the calculated value used as a criterion in the fluence calculation. Similarly, the fluence at which the saturated damage zone extends to the surface compares favorably with that based on depositing $2 \times 10^{21} \text{ keV/cm}^3$ into atomic displacements. The agreement between experimental and calculated values is slightly less satisfactory for the heavier Al ion.

In both Figures 8 and 9, the low fluence damage region appears to be more closely centered upon projected range, R_p , than x_m . It is suggested that the implanted N and Al atoms are immobile but that they may stabilize the irradiation produced defects against recombination or annealing.

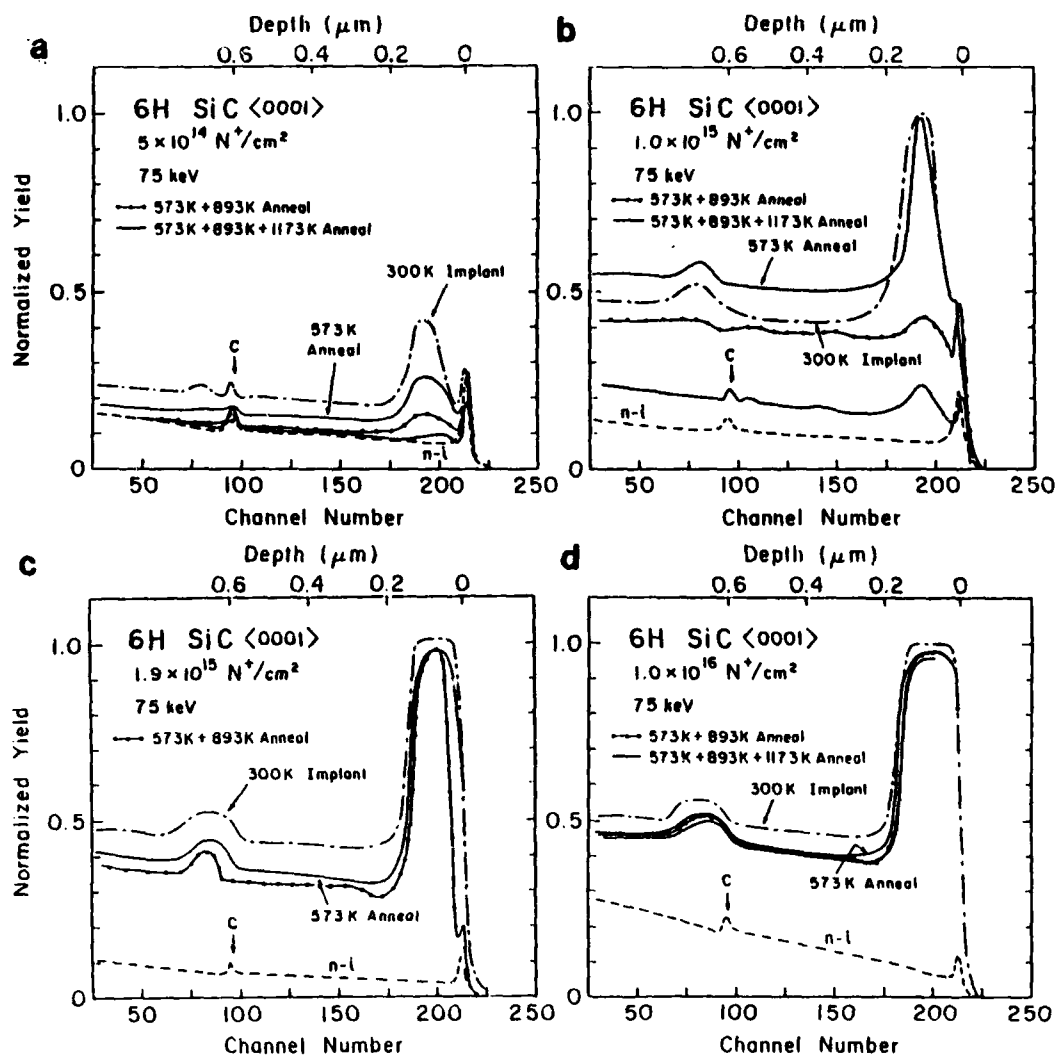


Figure 6 — RBS/channeling spectra from N-implanted and annealed SiC.

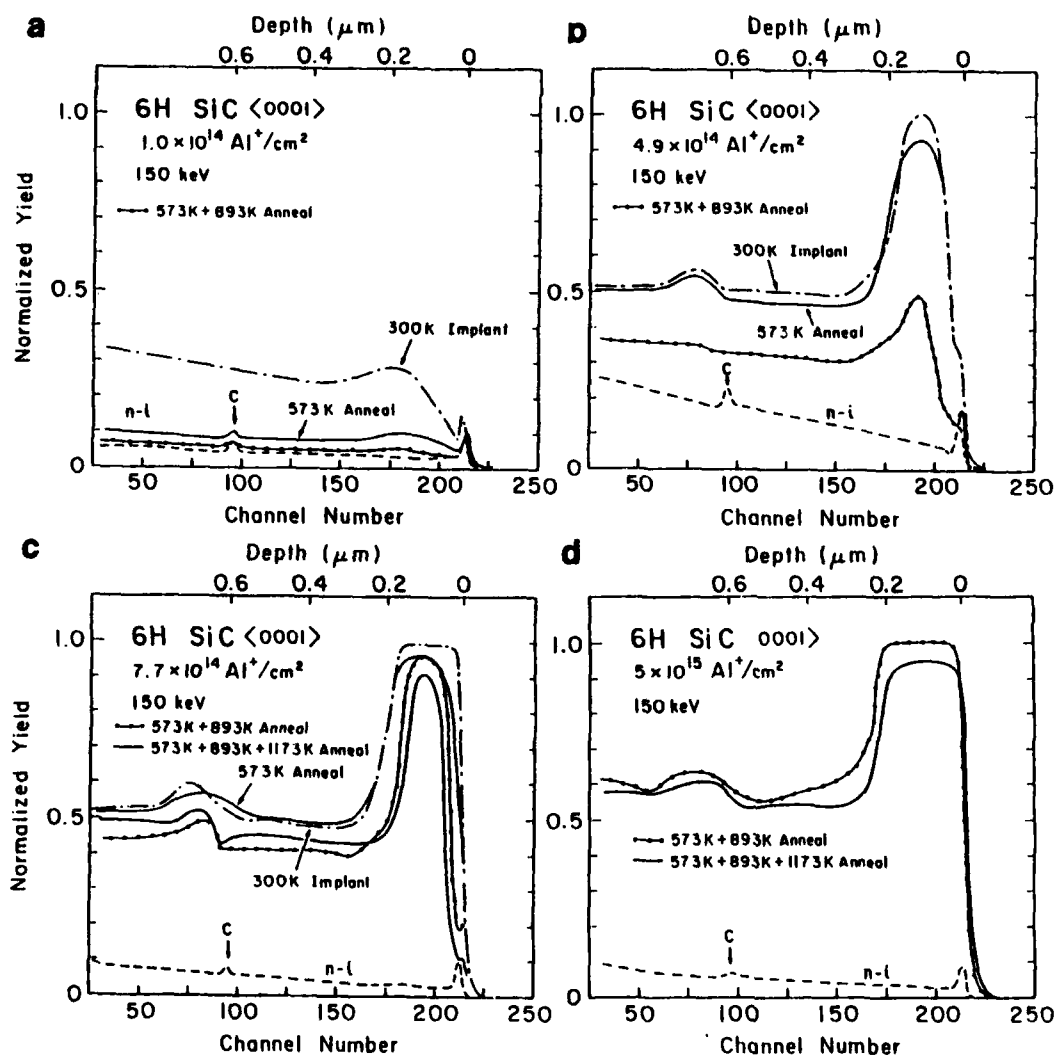


Figure 7 — RBS/channeling spectra from Al-implanted and annealed SiC.

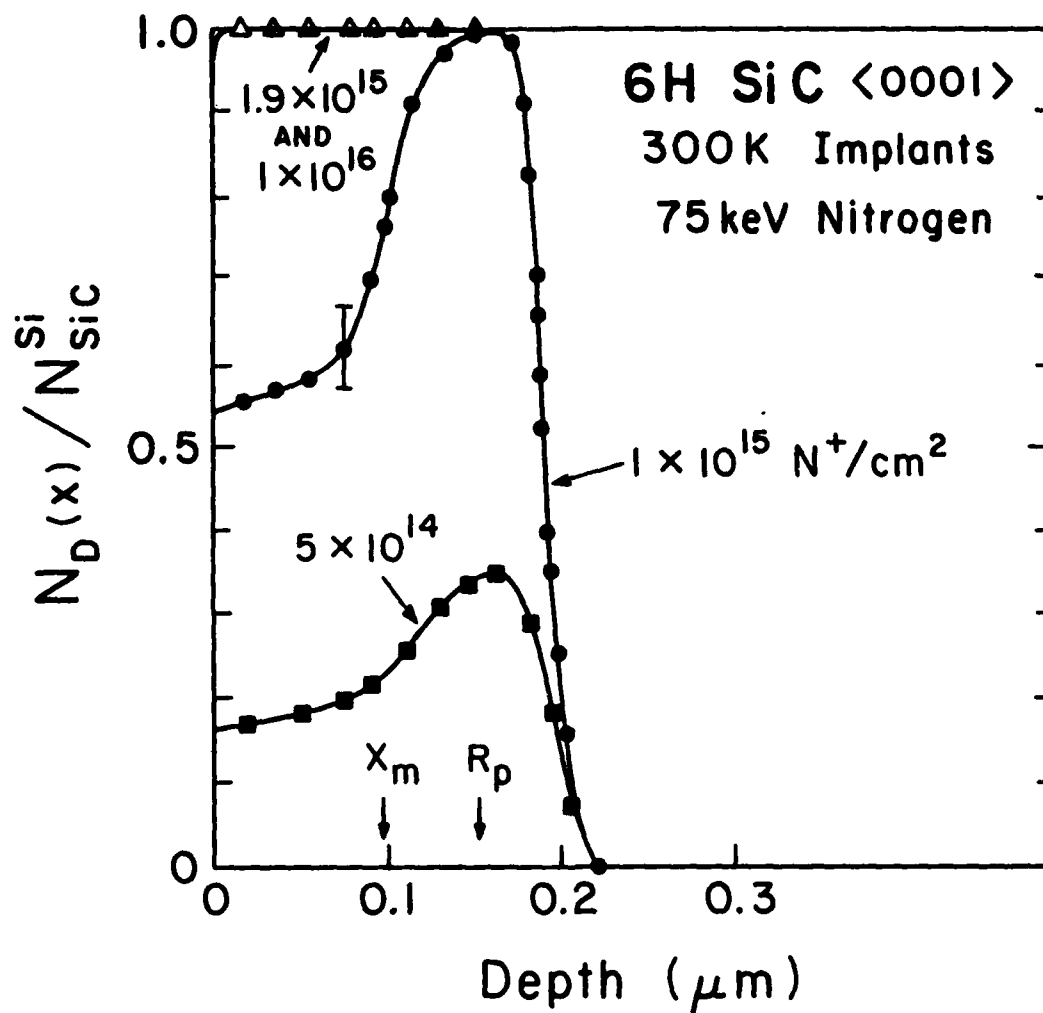


Figure 8 — Fraction of Si atoms displaced as a function of depth at different fluences for 75 keV N implants into 6H SiC <0001> at 300 K.

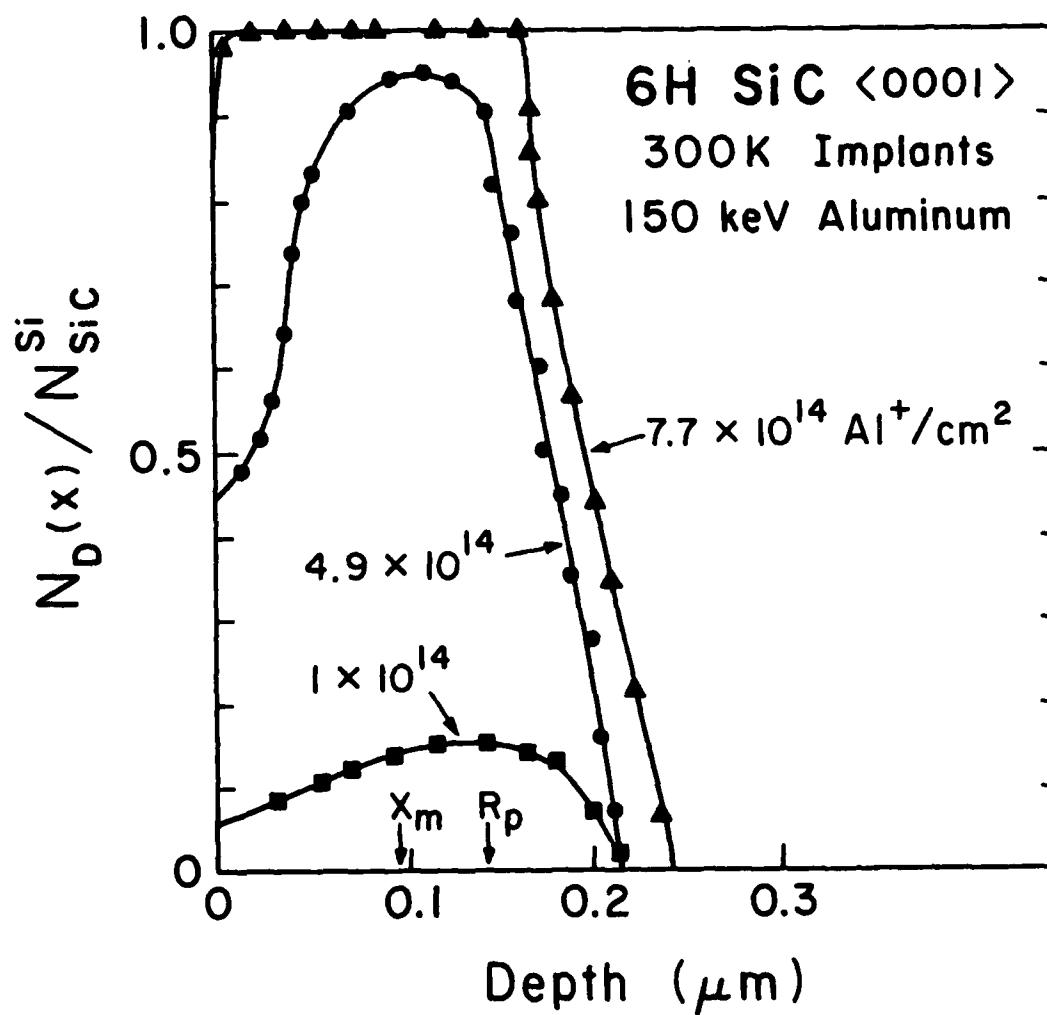


Figure 9 — Fraction of Si atoms displaced as a function of depth at different fluences for 150 keV Al implants into 6H SiC <0001> at 300 K.

Comparison of as-implanted and annealed spectra show that appreciable annealing has occurred in the low fluence implanted (damaged but crystalline) SiC after a 573 K/0.5 h anneal (Figures 6a and 7a). Estimates of the amount of recovery, based on reduction in the area under the direct backscattering Si peak, suggest that approximately 87% of the number of equivalent displaced Si atoms have been restored to lattice sites for the Al ion irradiated sample. Less recovery (approximately 40%) has occurred for the N ion bombarded crystal. Little recovery is seen at 573 K for specimens where the direct backscattering peak reaches the random yield for both ions, Figures 6b and 7b. After a further anneal of 893 K for 0.5 h, however, significant recovery is also observed in the specimens implanted to produce amorphization at x_m .

Dechanneling is further decreased in crystalline and amorphized ($x=x_m$) specimens after the 1173 K/0.5 h anneal, but a small direct backscattering peak still remains. After the same 1173 K/0.5 h anneal, the lowest fluence Al implant appears to show total damage recovery (not shown), while the spectrum from the N-implanted specimen ($5 \times 10^{14} \text{ N}^+/\text{cm}^2$) is approaching that of the non-implanted crystal (Figure 6a).

For the higher fluence implants, such dramatic recoveries are not observed. Spectra obtained from specimens implanted to fluences calculated to produce amorphization from the peak damage region to the front surface at $x = 0$ do show a progressive narrowing and intensity decrease of the direct backscattering peak, as the anneal temperature is increased (Figures 6c and 7c). The results indicate that annealing is progressing from both the front and back of the highly damaged region and may, therefore, suggest the presence of a very narrow residual crystalline layer at the front surface after implantation. In contrast, the highest fluence implants show no recovery at $x = 0$, only a marginal reduction in the direct backscattered intensity, and minimal recovery at the back of the damaged zone (Figures 6d and 7d). This is also true for the very high fluence, $5 \times 10^{17} \text{ N}/\text{cm}^2$ and $2 \times 10^{17} \text{ Al}/\text{cm}^2$ implanted specimens prepared as part of Phase II. The lack of recrystallization

at $x = 0$ is probably related to the lack of residual single crystal "seed".

3.1.2 Microhardness Measurements

In previous work by Roberts and Page,⁽¹³⁾ microhardness data were standardized to a chosen indent diagonal length using the Meyer analysis. The approach addressed the issue of measuring hardness on a composite specimen consisting of a thin surface layer and a substrate expected to have differing mechanical responses. This methodology was considered but not applied to the data obtained in this study because the depth of the damaged zone was $\leq 0.24 \mu\text{m}$. This is smaller than the indent depths produced by using a 25 g load which was the smallest load yielding measurable indent diagonals (10 g load indents could not be photographed sufficiently well, presumably because of their shallow depth, $\sim 0.15 \mu\text{m}$). Thus, the hardness data reported herein always reflect a combination of both implanted layer and substrate properties.

Knoop hardness numbers obtained using a 50 g load are plotted as a function of ion fluence in Figures 10 and 11. Unimplanted reference data are included for comparison. Utilization of a 25 g load produced similar trends in hardness change, but incompleteness of the data precluded its incorporation here. Figure 12 presents hardness obtained from the Al-implanted SiC using a 200 g load, which samples a much larger substrate volume. Some evidence of the trends apparent in Figure 10 are still present. In Figure 13, the microhardness data from the Phase I high fluence Al implant ($2 \times 10^{17} \text{ Al}^+ \text{ cm}^{-2}$, 150 keV) have also been included for comparison.

SiC implanted with Al at 300 K shows an initial increase in surface hardness followed by a decrease over the fluence range corresponding to the development of a highly damaged and predominantly amorphous surface layer. The N-implanted SiC exhibits similar, but smaller hardness changes. The highest fluence nitrogen microhardness data (implanted with $5 \times 10^{17} \text{ N}^+ \text{ cm}^{-2}$ at 75 keV) are not plotted because exfoliation around the indentations precluded accurate measurements. These results are contrary to those reported previously⁽¹³⁾ where

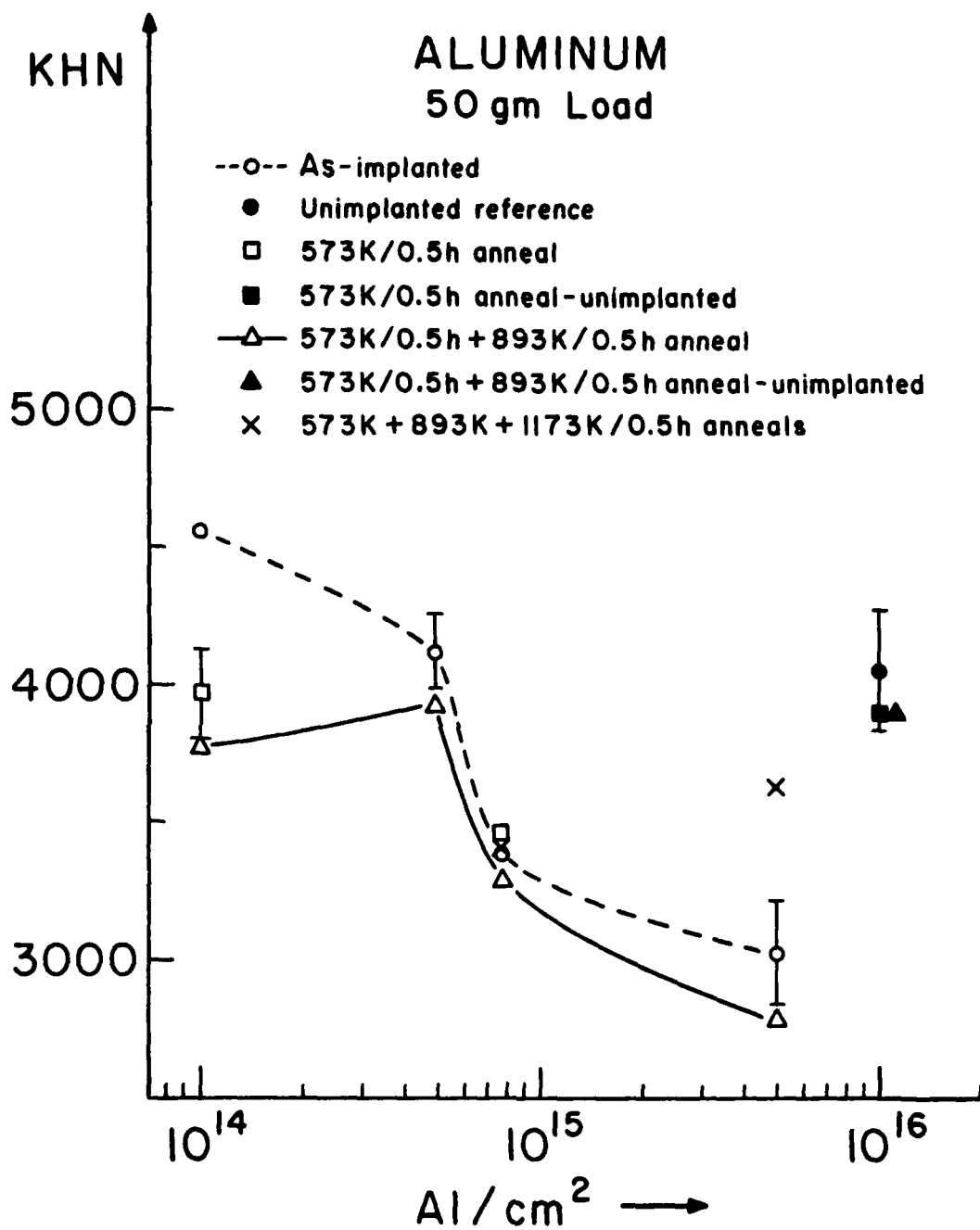


Figure 10 — Knoop hardness of implanted and annealed SiC.

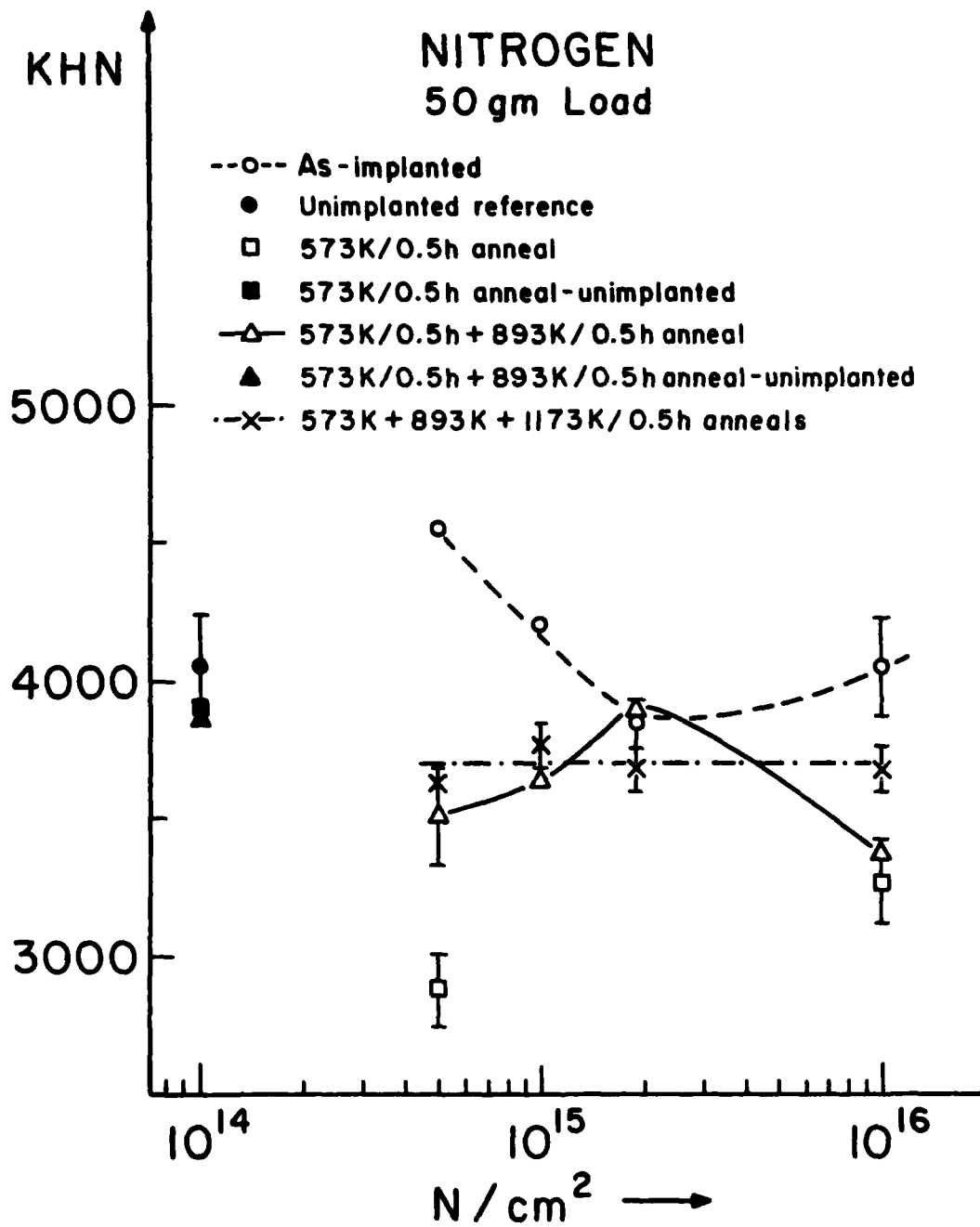


Figure 11 — Knoop hardness of implanted and annealed SiC.

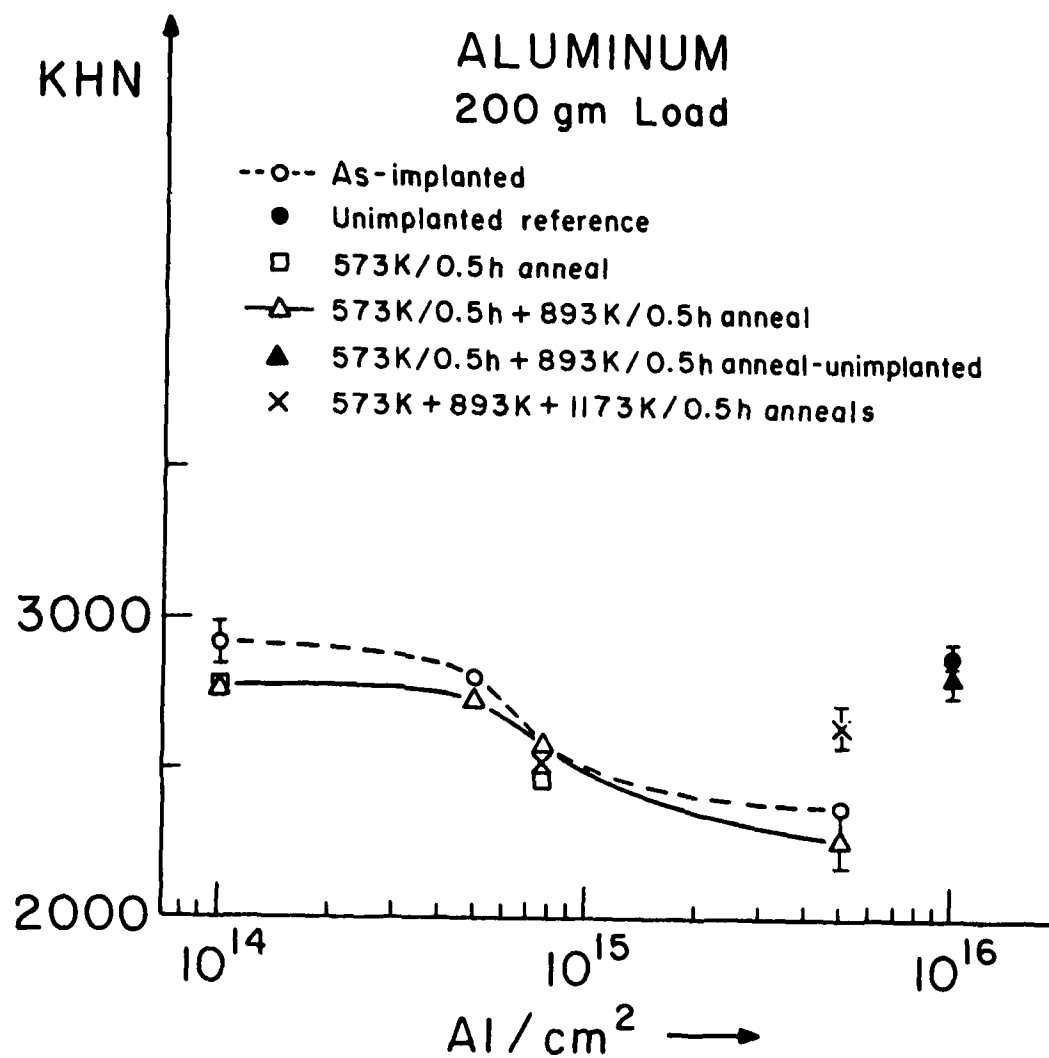


Figure 12 — Knoop hardness of implanted and annealed SiC.

Curve 754806-A

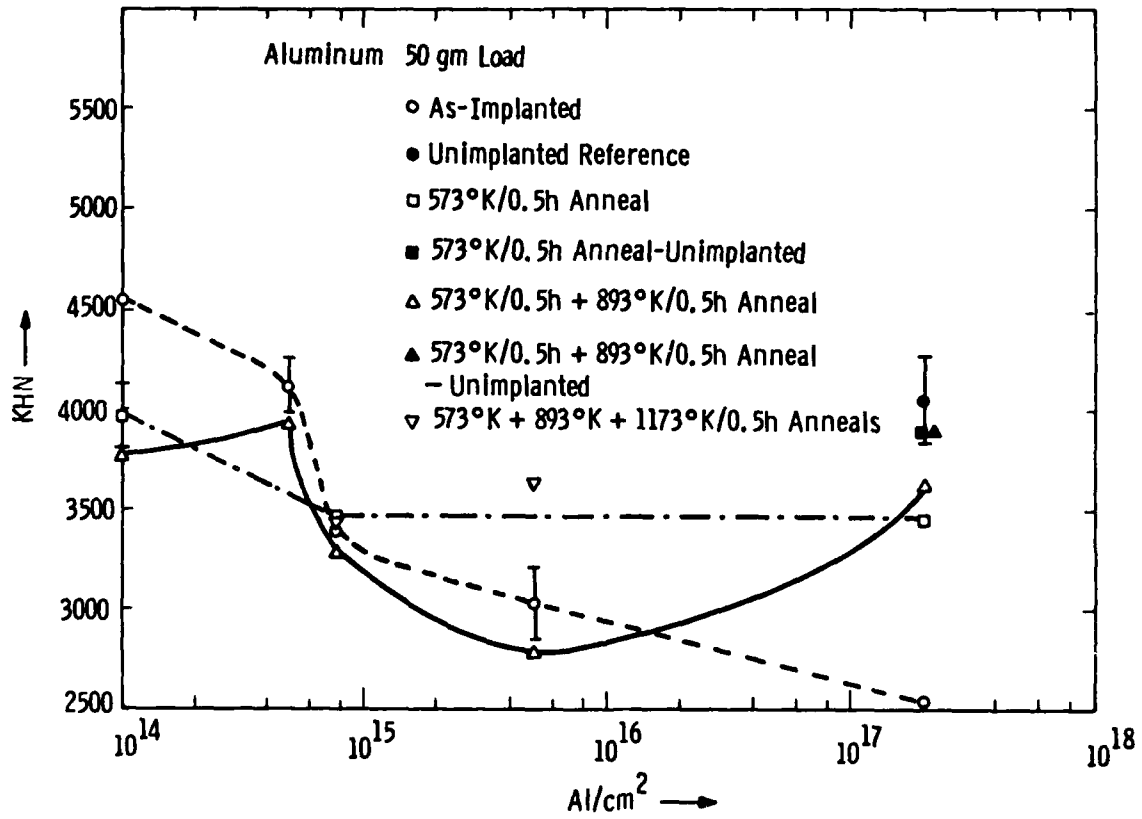


Figure 13 — Knoop hardness of implanted and annealed SiC.

significant changes in hardness were observed only for fluences $> 4 \times 10^{17} \text{ N}_2^+/\text{cm}^2$ (80 keV). These latter implantations were performed with an estimated substrate temperature of 573 K. The 573 K annealing behavior reported in this paper suggests that, at low fluences, the as-implanted damage may be different for the two sets of experiments.

Annealing of the low fluence (still crystalline) N and Al implanted specimens produces a hardness decrease which may be related to the recovery observed in the RBS data. The 573 K/0.5 h anneal results in a ~33% decrease in hardness in the $5 \times 10^{14} \text{ N}^+/\text{cm}^2$ SiC sample. The hardness then increases after the subsequent 893 K anneal. Both values are below the non-implanted reference hardness, whereas the low fluence Al hardness recovers to the unimplanted reference value. Both the high fluence ($2 \times 10^{17} \text{ Al}^+/\text{cm}^2$) implant and the intermediate fluence implant ($5 \times 10^{15} \text{ Al}^+/\text{cm}^2$) also tend to recover their unimplanted hardness values as annealing progresses but after a 1233 K/0.5 h anneal, the highest fluence specimen exhibited severe exfoliation at loads ≥ 10 g. Figure 14 shows representative indents, after the various experimental stages. Up to 873 K, however, the structures responsible for the hardness decrease in SiC implanted with $7.7 \times 10^{14} \text{ Al}^+/\text{cm}^2$ and $5 \times 10^{15} \text{ Al}^+/\text{cm}^2$ appear stable and thus should be unaffected by high temperature processing.

With the exception of the high fluence ($5 \times 10^{17} \text{ N}^+/\text{cm}^2$) specimen, the annealing behavior after nitrogen implantation shows a general trend towards a constant hardness independent of implantation fluences after the 1173 K anneal. This hardness value is somewhat below unimplanted SiC reference hardness. After annealing at lower temperatures, some softening was observed in the $1 \times 10^{16} \text{ N}^+/\text{cm}^2$ specimen at loads ≤ 50 g. At higher loads indentation produced severe exfoliation and cracking not observed in the high fluence Al specimen. In the $5 \times 10^{17} \text{ N}^+/\text{cm}^2$ specimen, lateral cracking and exfoliation was pronounced at ≥ 10 g loads for as-implanted and all annealed specimens. After the highest temperature anneal (1233 K/0.5 h), a "pseudo-plasticity" was observed in SEM images, but it was still not possible to obtain accurate measurements on the indent dimensions. Scanning

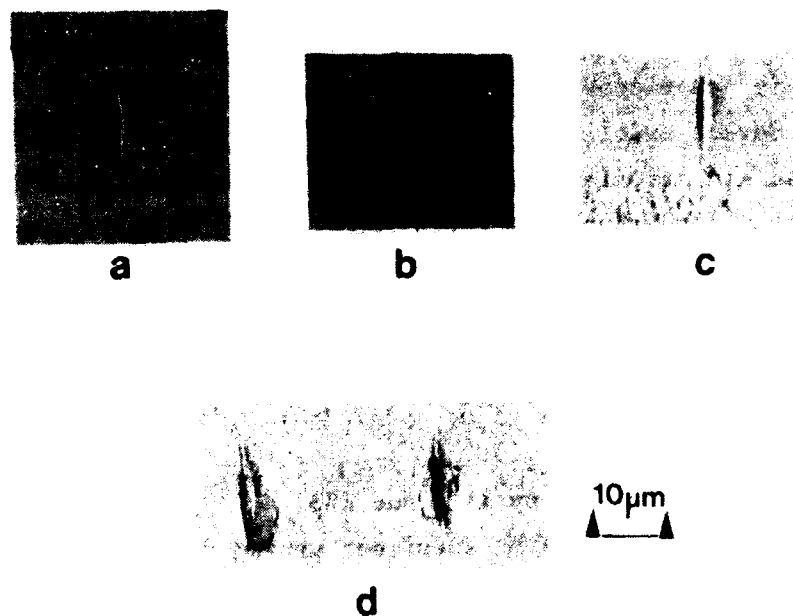


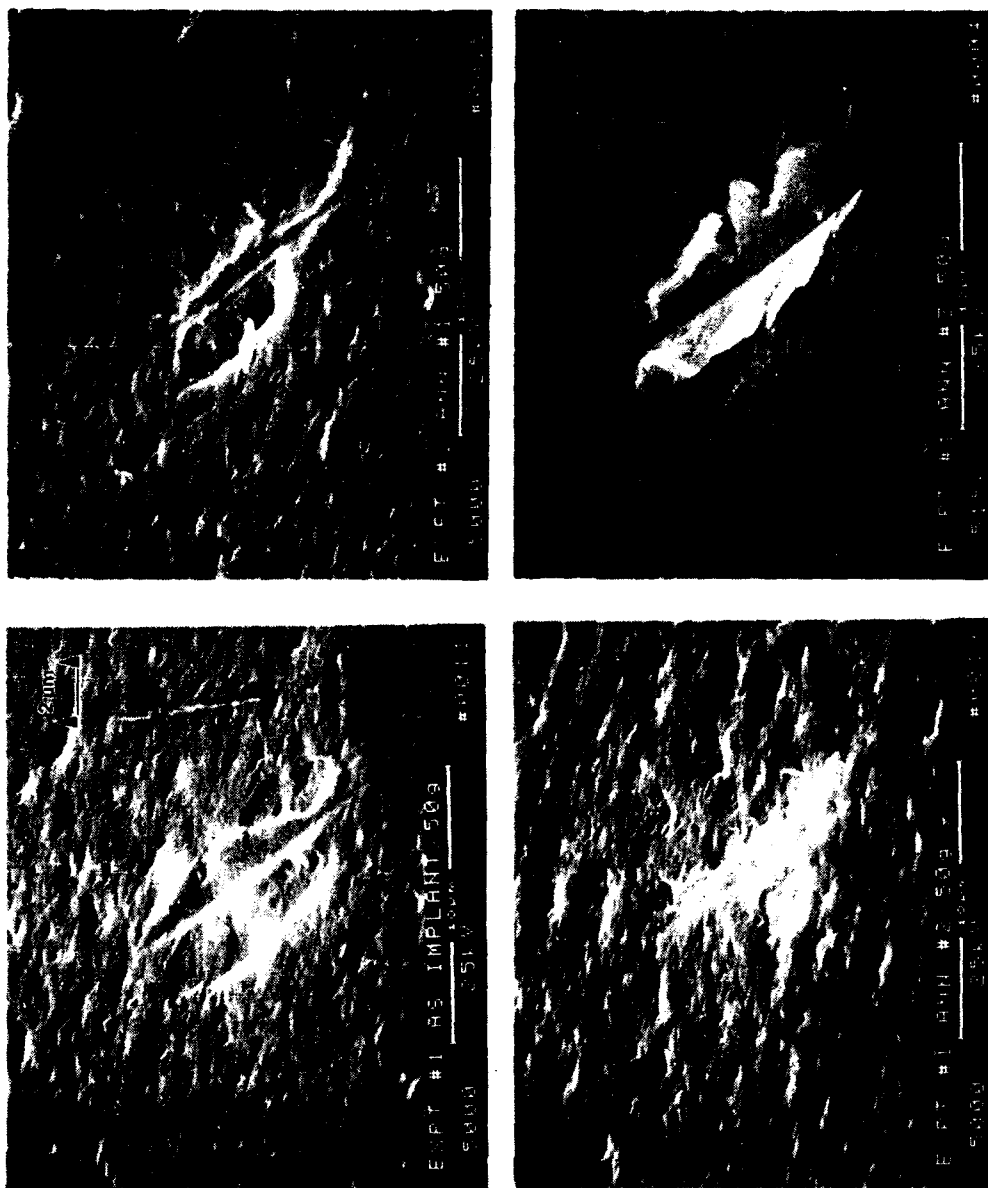
Figure 14 — Microhardness indents obtained using a 50 g load on a SiC single crystal implanted with $2 \times 10^{17} \text{ Al}^+/\text{cm}^2$ at 150 keV. All indents are parallel to a $[1210]$ direction:
a) as-implanted; b) after 573 K/0.5 h anneal; c) after 573 K/0.5 h + 893 K/0.5 h anneals; d) after 573 K/0.5 h + 893 K/0.5 h + 1233 K/0.5 h anneals.

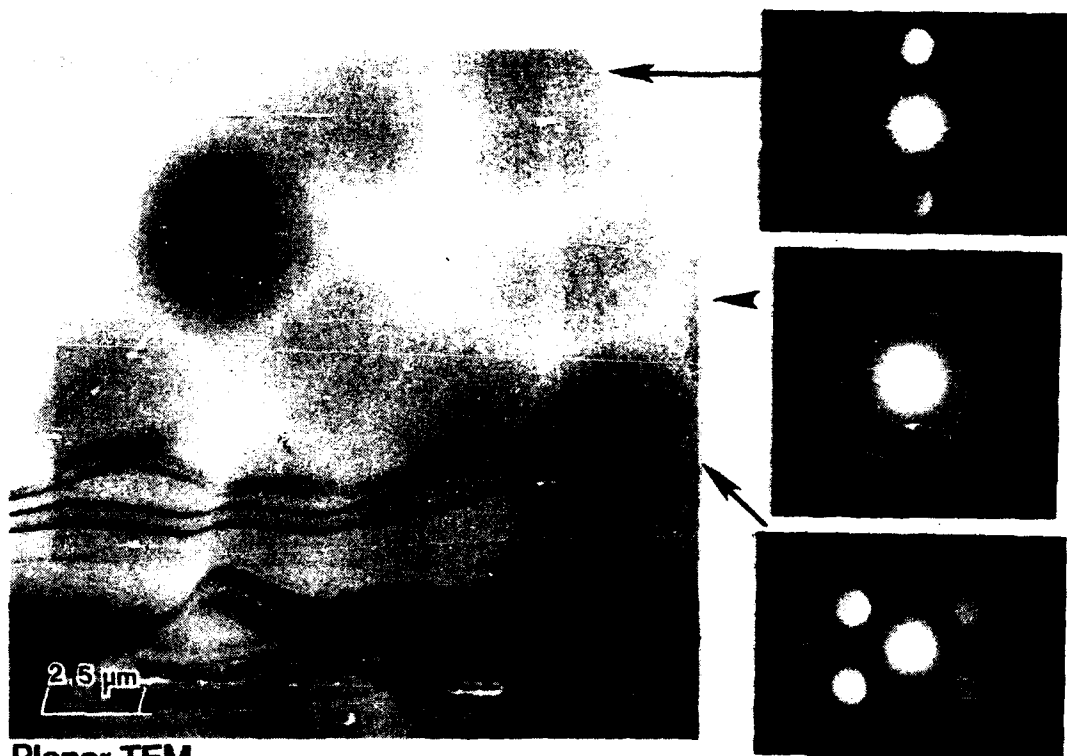
electron micrographs (SEM) presented in Figure 15 show microhardness indents using a 50 g load after the various experimental stages. The SEM also highlights the surface condition produced by the oxidation/acid etch process used for all Phase II surface sample preparation. Since the exfoliation behavior was observed in higher fluence specimens after both types of surface preparation (Phase I and Phase II), it is believed that differences in residual compressive stress and surface morphology did not impact microhardness properties.

Severe exfoliation and indent morphologies in the nitrogen implanted and annealed SiC crystals at loads higher than 50 g are similar to those which have been recorded for higher fluence H-implanted SiC (see reference 16 and Appendix A). The data suggest that the property changes are linked to the chemical nature of the dopant atoms as well as the atomic displacement damage in the temperature regime of the intermediate anneal.

3.1.3 Characterisation by XTEM and AES

Preparation of XTEM specimens proved difficult because of excessive edge milling during the final stage of the thinning process and so, some additional work was initiated on planar sections. Unfortunately, since suitable TEM specimens could be included in only a limited number of implantation experiments, and several were lost during sample preparation, TEM could not be utilized as a major characterization technique to follow annealing and recovery behavior. It was used, however, as a cross-reference with the RBS/channeling data to assess the validity of the amorphization criterion used in the original fluence selection, for example. These data are specifically discussed in Reference 16 (Appendix A). TEM analysis of the SiC specimen implanted with $7.7 \times 10^{14} \text{ Al}^+/\text{cm}^2$, Figure 16, determined by microdiffraction (a) that a very thin (probably $> 10 \text{ nm}$) residual crystalline layer was still present at the front surface, and (b) that the remainder of the implanted layer was predominantly amorphous. These observations indicate that the saturated damage zone, predicted by the





Planar TEM

6H<0001> SiC; 7.7×10^{14} Al/cm²; As-implanted

Figure 16 — Plan view Brightfield TEM micrograph and diffraction patterns of 6H <0001> SiC crystal as implanted with 7.7×10^{14} Al⁺/cm². Top) narrow crystalline layer at bombarded surface; Middle) amorphous implanted region; Bottom) crystalline region beyond R_p .

amorphization criterion of $S_D(x) = 2 \times 10^{21} \text{ keV/cm}^3$ did not quite extend to $x = 0$. Evaluation of SiC implanted with $5 \times 10^{15} \text{ Al}^+/\text{cm}^2$ (a fluence calculated to be well in excess of that required to produce amorphicity from $x = x_m$ to the surface at $x = 0$) is shown in Figure 17. The crystal is indeed amorphous from the front surface to a depth of $\sim 230 \text{ nm}$, in agreement with the RBS/channeling data in Figure 7d.

An XTEM image of a sample of N-implanted SiC bombarded with $1 \times 10^{15} \text{ N}^+/\text{cm}^2$ and annealed at 573 K and 893 K for 0.5 h is shown in Figure 18. This fluence was calculated to produce amorphization at $x = x_m$. After the anneals, microdiffraction analyses showed that the entire damage zone is crystalline, although the crystal quality is poorer than that of the virgin SiC. This is consistent with the recovery observed by RBS/channeling (Figure 6b) and microhardness measurements (Figure 11). Residual black spot damage, similar to that observed after hydrogen implantation in SiC⁽¹⁷⁾ was present.

Because of the extreme changes in microhardness behavior exhibited by the very high fluence nitrogen and aluminum implants ($5 \times 10^{17} \text{ N}^+/\text{cm}^2$ and $2 \times 10^{17} \text{ Al}^+/\text{cm}^2$, respectively) after the third, high temperature anneal, it was decided that AES profiling studies should provide valuable insight into the distribution of dopant species and, hopefully, into the understanding of the surface mechanical property modification. The concentration profiles for both implanted and non-implanted portions of annealed SiC are presented in Figures 19-22. For specimen D149 $\mu 1$ (Expt. 1 in Table 2.3), comparison of the carbon profiles in the implanted and unimplanted portions of the crystals clearly shows that the former has considerable surface carbon enrichment which does not decrease to the stoichiometric value until a depth of $\sim 160 \text{ nm}$ has been reached. In fact, the first 60 nm, appears to be almost 100 At% carbon. This may well explain the "pseudo-plasticity" observed in SEM images of the microhardness indents on this specimen, after the third anneal. Interestingly, the nitrogen dopant profile exhibits a reasonable, Gaussian-like shape and indicates that the nitrogen probably has very little mobility and is trapped in the damage

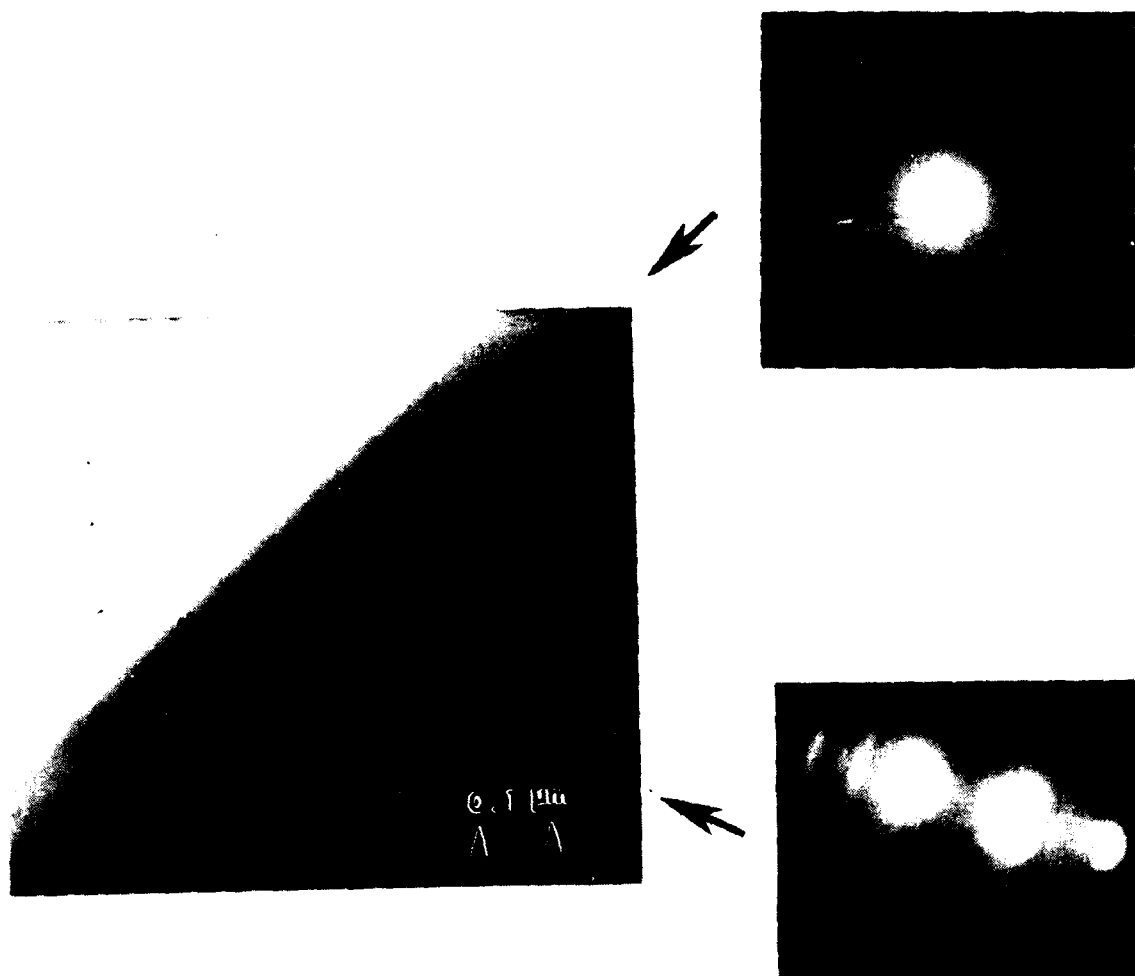


Figure 17 — Cross-section TEM micrograph and diffraction patterns of 6H <0001> SiC crystal as-implanted with $5 \times 10^{15} \text{ Al}^+/\text{cm}^2$; Top) 230 nm wide band of amorphous SiC extending to bombarded surface; Bottom) Crystalline SiC beyond R_p .

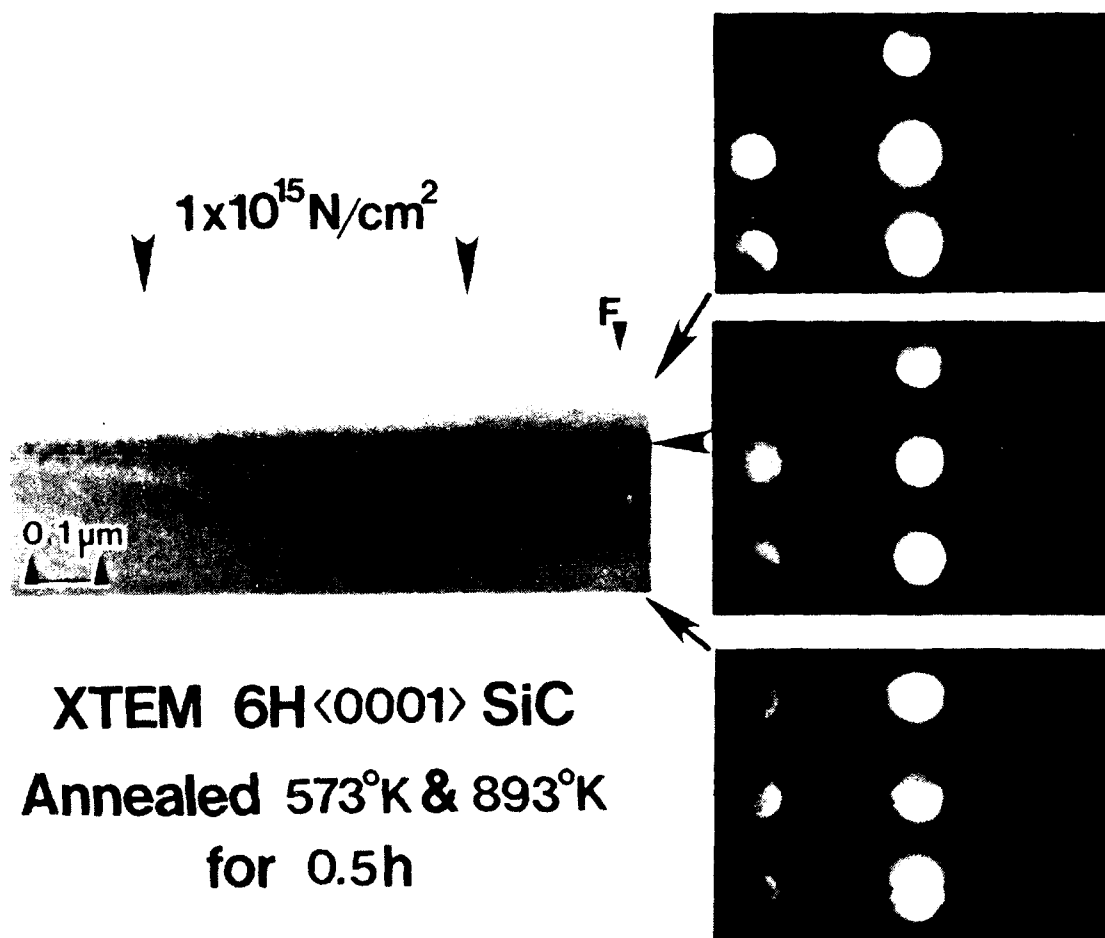


Figure 18 — Cross-section Brightfield TEM image and diffraction patterns of 6H <0001> SiC crystal implanted with $1 \times 10^{15} \text{ N}^+/\text{cm}^2$ and annealed at 573 K/0.5 h + 893 K/0.5 h. Annealing has restored crystallinity in the damage zone.

Curve 754794-B

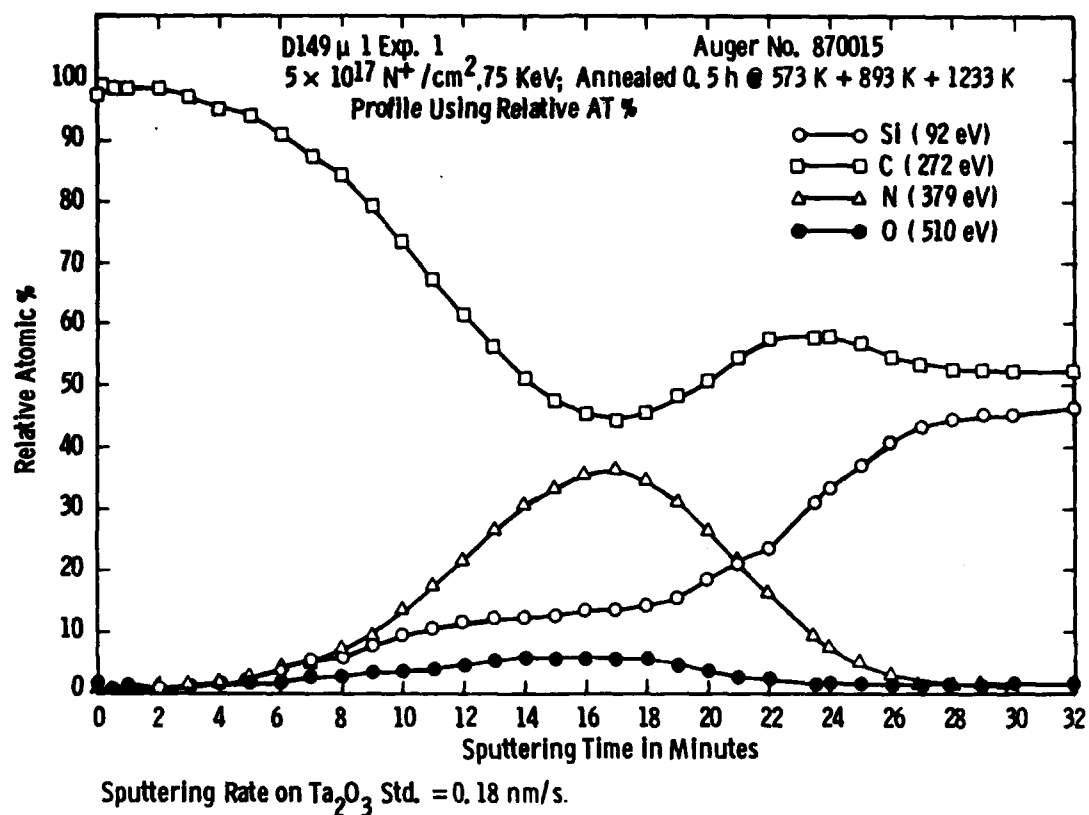


Figure 19 — Auger concentration profiles showing the distribution of Si, C, N, and O in specimen D149 μ l, Experiment #1, after implantation and annealing.

Curve 754791-A

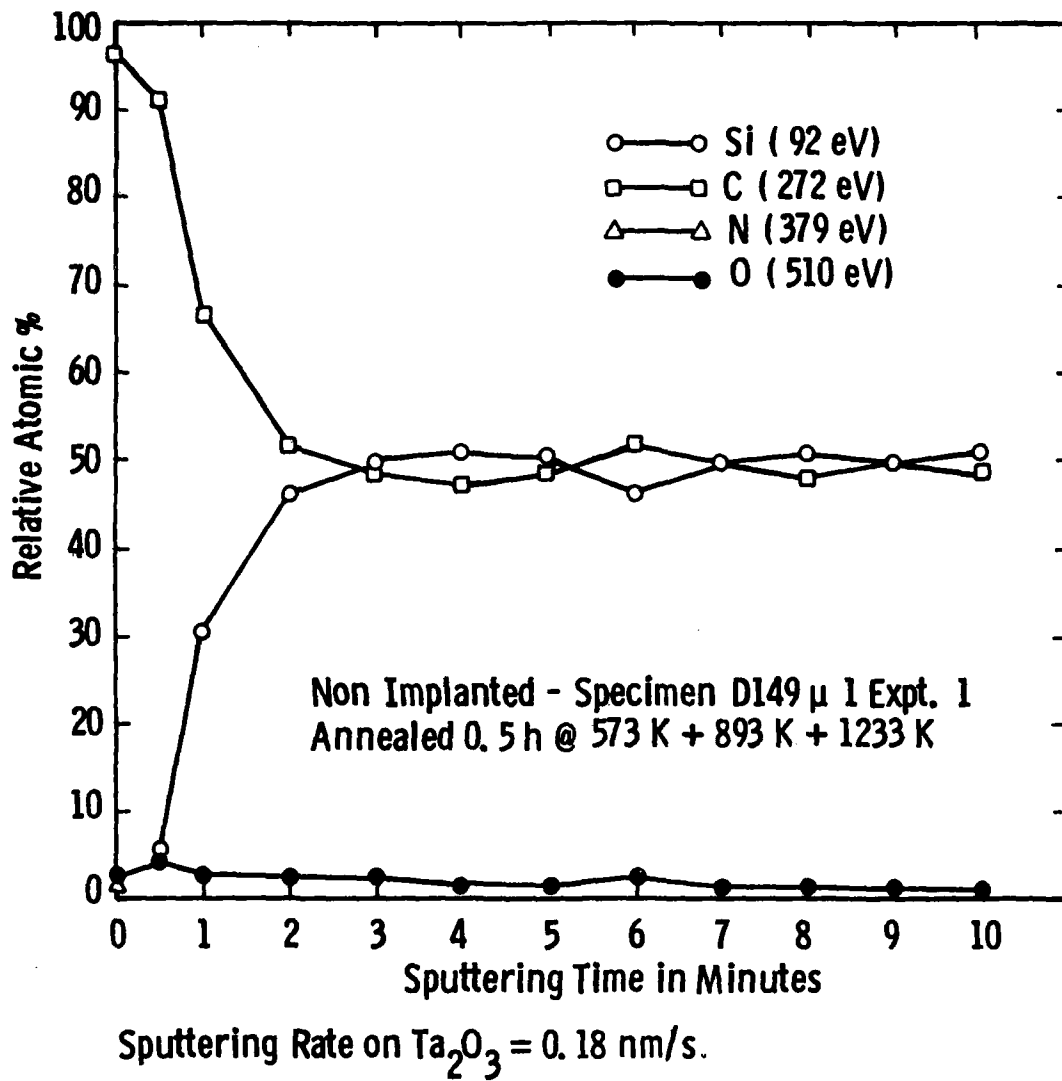


Figure 20 — Auger concentration profiles showing the distribution of Si, C, N and O in the unimplanted side of specimen D149 μ 1. Experiment #1.

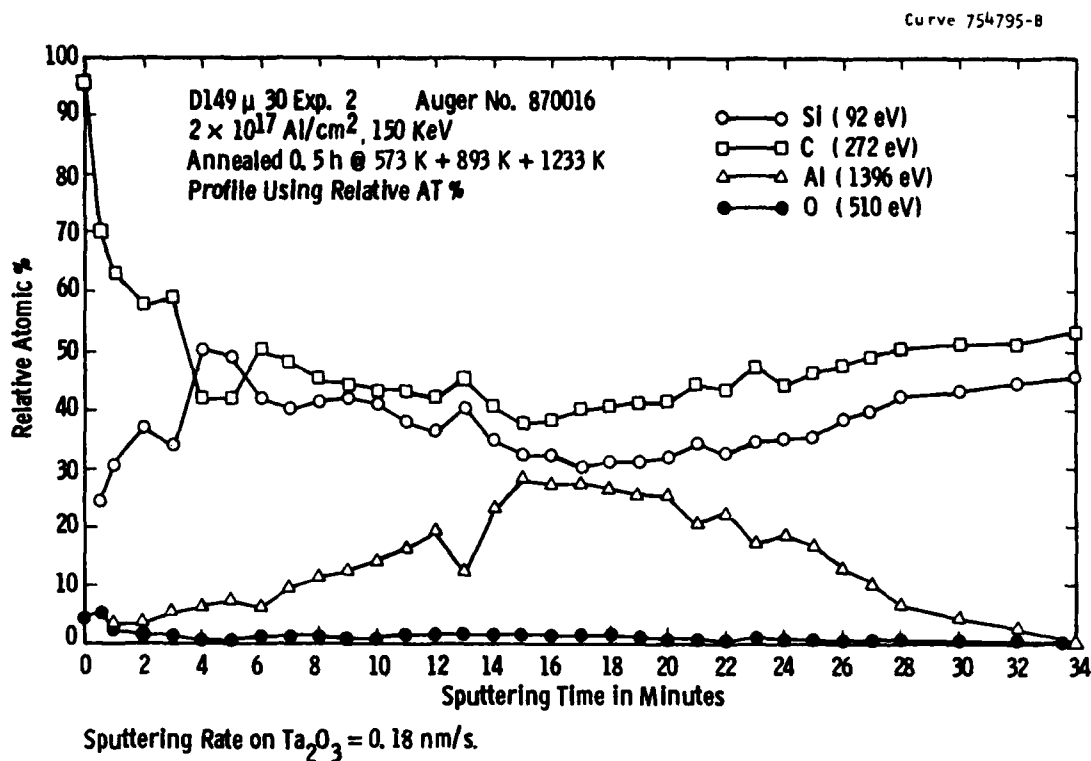
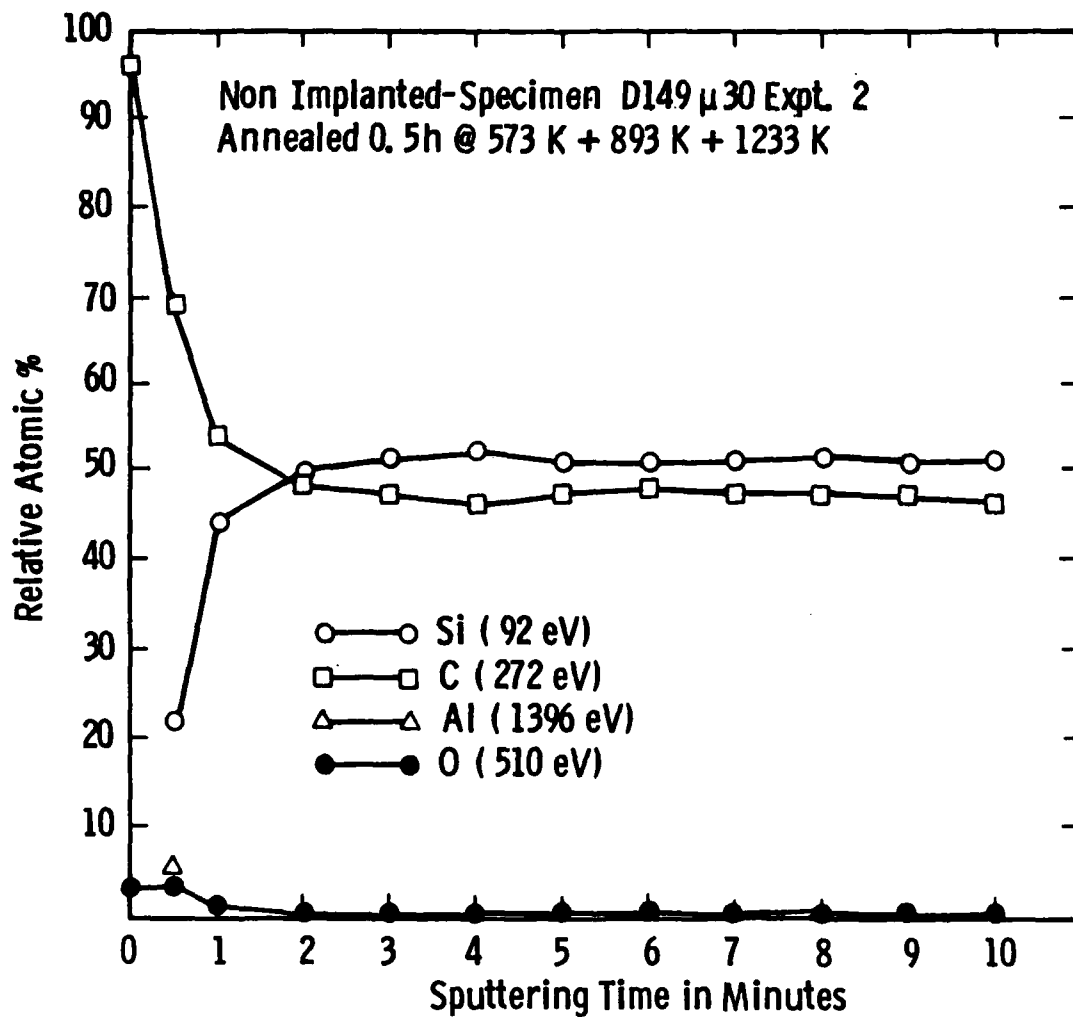


Figure 21 — Auger concentration profiles showing the distribution of Si, C, N and O in specimen D149 μ 30. Experiment #2.

Curve 754792-A



Sputtering Rate on Ta_2O_3 = 0.18 nm/s .

Figure 22 — Auger concentration profiles showing the distribution of Si, C, N and O in the unimplanted side of specimen D149 μ 30. Experiment #2.

structure. The profile is centered upon the predicted value of R_p (see Figure 8). The oxygen concentration is also enriched, relative to the baseline, unimplanted specimen concentration, in the region of high nitrogen concentration. Near stoichiometric concentrations of C and Si are observed at depths ≥ 300 nm. It should be noted that we have reasonable confidence in the Auger concentration measurements because, in the unimplanted reference portion of the crystal, stoichiometric compositions are consistently reached at depths ≥ 20 nm.

Formation of a near surface, carbon-rich layer, may have several implications for matrix-reinforcement bonding in MC and crack blunting or energy dissipation in CC. Further pursuit of this finding is warranted, but beyond the scope of the present investigation.

In contrast to the high fluence nitrogen implant, SiC implanted with 2×10^{17} Al⁺/cm² showed no extensive near-surface carbon enrichment after high temperature annealing (Figure 21). The implanted aluminum exhibits a very broad concentration profile which suggests that diffusion must have occurred both towards the crystal surface and into the bulk. The profile is, once, again, centered approximately upon the projected range, R_p , (see Figure 9). Stoichiometry is approached at a depth of ~ 340 nm. Data from the unimplanted portion of the crystal (Figure 22) suggest that its composition is slightly carbon enriched, but the Si/C ratios are consistent over the range of depth examined.

Unfortunately, the AES results from the Al-implanted SiC are not particularly helpful in explaining the transition from plastic to brittle behavior exhibited by the microhardness indents. The effect must be microstructurally, rather than chemically based and thus requires further effort (probably by TEM) to develop an explanation.

AES analyses were not performed on lower fluence samples because the implanted dopant concentrations were below Auger detectability limits. In retrospect, it is apparent that AES is a valuable tool for interpreting high fluence surface mechanical behavior. However, further use in the present study was precluded because the scope provided for

only limited crystal implants which could not be destructively analyzed until all annealing experiments were completed. Additional work could, for example, focus particularly on the high fluence N-implant annealing behavior and follow the specifics of the carbon enrichment more closely.

3.2 PHASE II: IMPLANTATION EXPERIMENTS

Results from experiments 1 and 2 listed in Table 2.3 were discussed in conjunction with the Phase I data because they were natural extensions of that work. The intent was to explore the effects of higher Al and N fluences, and to compare the results with the earlier University of Cambridge studies on nitrogen implantation into blue-black SiC crystals grown by the Atcheson Process and implanted at slightly higher temperatures. Results from experiments 3 - 8 will be reported in this section.

The primary objectives of this series of experiments were as follows:

- 1) To determine whether "passivation" of dangling Si bonds in a-SiC by hydrogen affects regrowth of the amorphous layer as has been observed in Si crystals
- 2) To determine whether the softening observed in Phase I was due solely to residual compressive stresses
- 3) To determine whether the electronic nature of the dopant (n-type, p-type, isovalent) affects the regrowth of the amorphous layer
- 4) To determine whether the point contact stresses and thermal cycle during powder processing of a aluminum alloy - SiC_p composite affect the ion beam modified surface

These issues were addressed by tailoring the implantation experiments as indicated by the different ion kinetic energies and fluences in Table 2.3. The ion implantation parameters were selected to permit comparisons at equal (calculated) numbers of atomic displacements.

3.2.1 Hydrogen Effects

Hydrogen is known to be effective in eliminating unwanted electronic states in amorphous, polycrystalline and crystalline silicon. The interaction of hydrogen with dangling Si bonds, grain boundaries and other impurity/dopant atoms is currently the focus of extensive investigation in a number of laboratories.⁽¹⁸⁾ In earlier studies we had shown that it is not possible to turn silicon crystals amorphous by proton bombardment at 300 K.⁽⁹⁾ SiC can be rendered amorphous at 300 K at proton fluences above $4 \times 10^{17} / \text{cm}^2$, but annealing of the damage during implantation occurs if the implantation temperature is above 800 K.⁽⁹⁾ The effects of post-implantation annealing were not known.

To determine whether the implantation induced softening and annealing effects in 6H SiC could be further controlled by the addition of hydrogen, two crystals were implanted with $5 \times 10^{15} \text{ Al}^+ / \text{cm}^2$ at 300 K. One of the crystals was then implanted with $5 \times 10^{17} \text{ H}^+ / \text{cm}^2$ at 300 K with the incident kinetic energy chosen to deposit the hydrogen within the region of the crystal damaged by the preceding aluminum ion bombardment, Table 2.3. The average concentration of implanted hydrogen calculated from equation 2-1 is $4.6 \times 10^{22} \text{ atoms/cm}^2$. This corresponds to approximately 50 atomic percent relative to SiC, or one hydrogen for each displaced Si atom in a totally amorphized damage zone. Both crystals were subsequently annealed at 1173 K for 0.5 h.

RBS/channeling measurements of the two crystals after implantation are shown in Figure 23. Both crystals exhibit a direct backscattering yield corresponding to a randomly oriented or amorphous Si sublattice. The hydrogen implantation has resulted in a slightly broadened damage peak. TEM observations, Figure 24, confirm the existence of an amorphous band extending approximately 260 nm from the

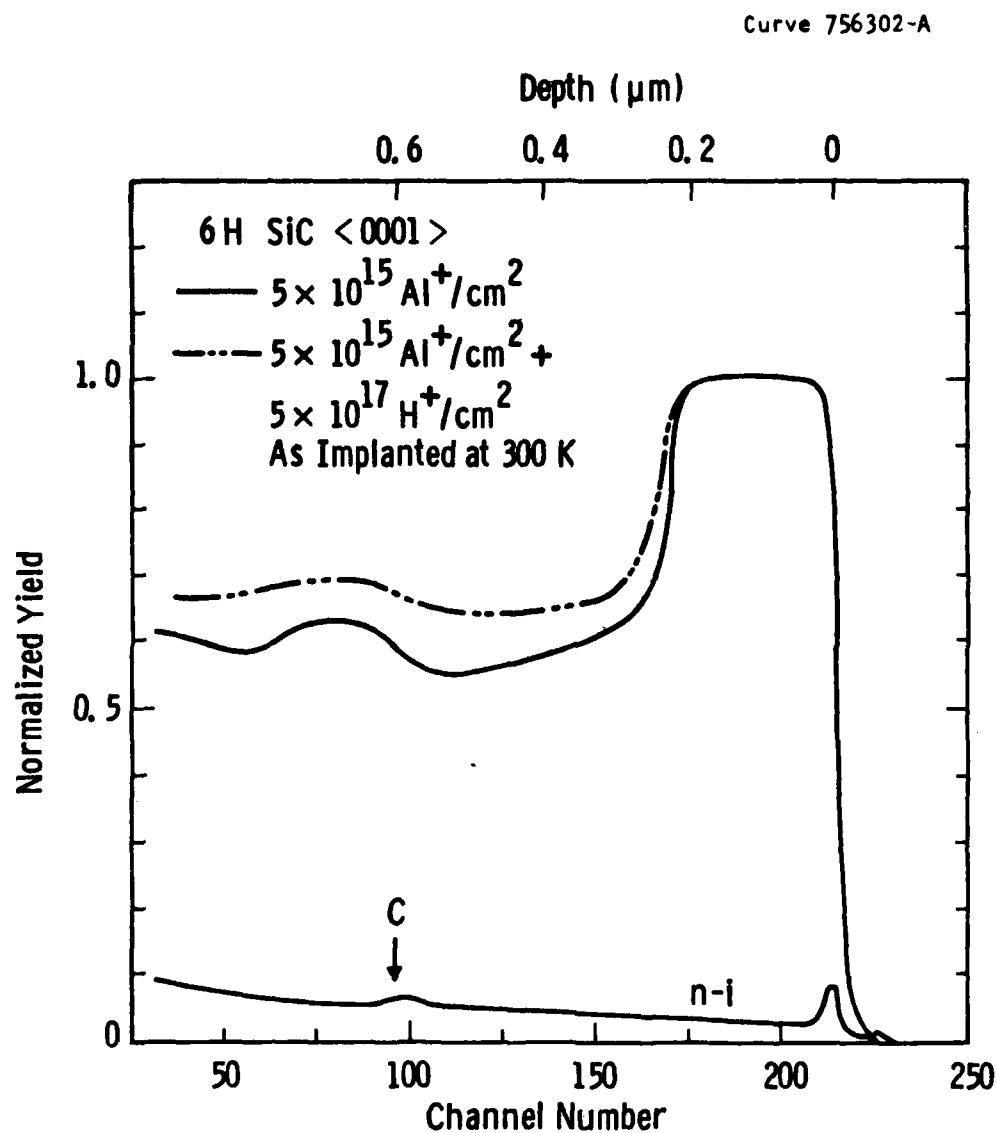


Figure 23 — RBS/channeling spectra of 6H SiC single crystals implanted with $5 \times 10^{15} \text{ Al}^+/\text{cm}^2$ and $5 \times 10^{15} \text{ Al}^+/\text{cm}^2 + 5 \times 10^{17} \text{ H}^+/\text{cm}^2$ at 300 K.

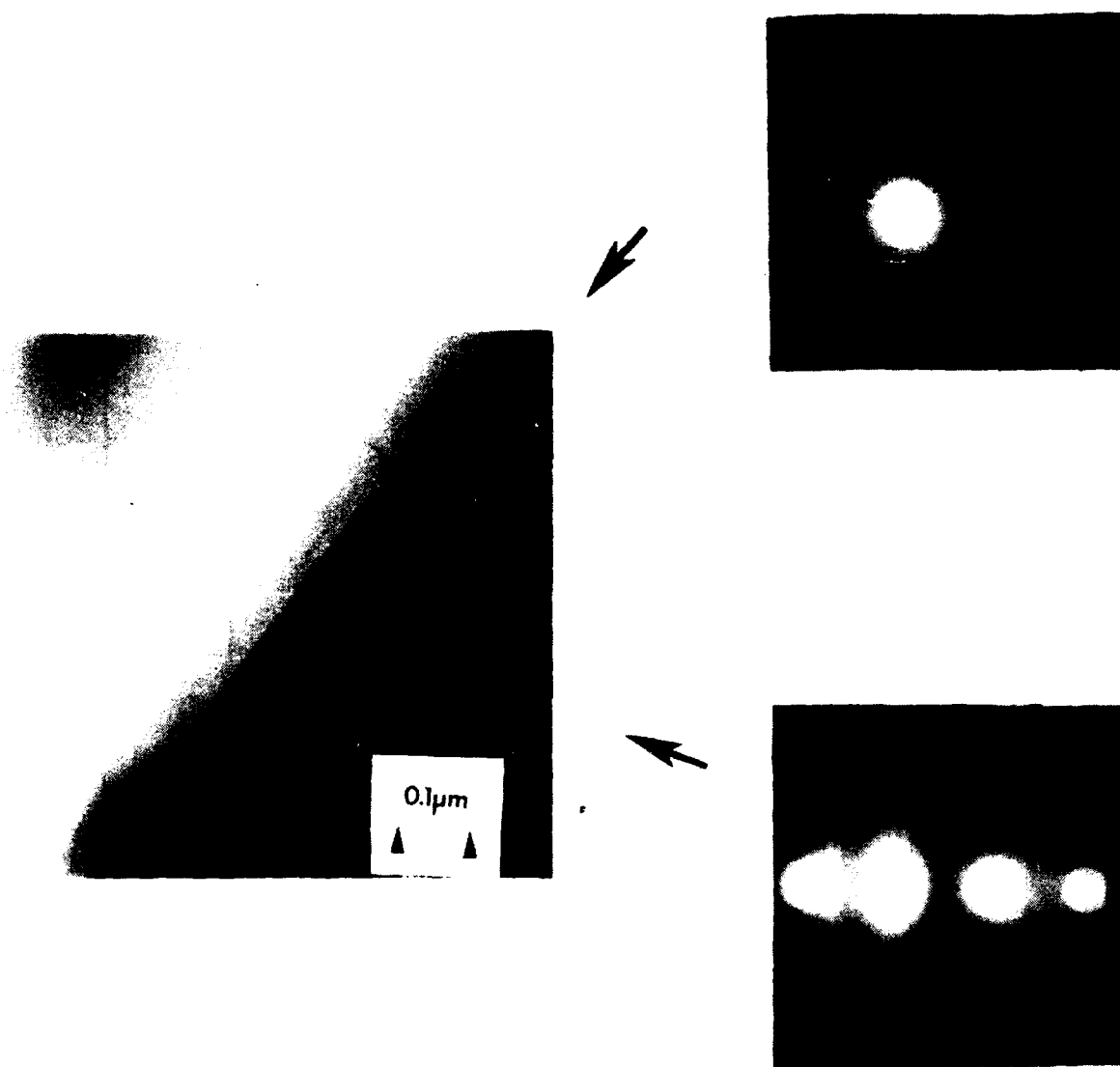


Figure 24 — Cross-section TEM micrograph and diffraction patterns of 6H <0001> SiC crystal as-implanted with $5 \times 10^{15} \text{ Al}^+/\text{cm}^2$ plus $5 \times 10^{17} \text{ H}^+/\text{cm}^2$ at 300 K; Top) 260 nm wide band of amorphous SiC extending to bombarded surface; Bottom) crystalline SiC beyond R_p .

bombarded surface. This is slightly wider than that measured after implantation with the aluminum ions, Figure 17, in agreement with the RBS/channeling data.

The effect of post-implantation annealing is shown in Figure 25. The presence of the hydrogen has had little effect on the recovery of the damaged region. The broadened "tail" in the direct backscattering peak resulting from the hydrogen implantation, Figure 23, has been eliminated. Annealing has been slightly retarded, however, by the addition of hydrogen over most of the wide band of atomically displaced silicon atoms. Comparison of the "dip" in the random backscattering curves for the as-implanted and annealed hydrogen-containing specimen (not shown) indicates that all of the implanted hydrogen has been retained in the crystal even after annealing at 1173 K. Microhardness values of as-implanted and annealed crystals were also independent of the presence or absence of hydrogen.

It is concluded that second stage hydrogen doping by energetic ion implantation at 300 K is not effective in promoting recovery to a crystalline or quasi-crystalline⁽⁹⁾ microstructure in a-SiC during post-implant annealing. Implantation of hydrogen at elevated temperature or introduction by other means such as exposure to RF plasmas, however, may have a significant effect.

3.2.2 Residual Compressive Stresses

Each implanted ion as it comes to rest introduces a center of dilatation in a crystal and thus gives rise to residual compressive stresses. Cantilever beam deflection experiments suggest that large residual stresses approaching the yield or fracture stresses of many materials can be reached at modest fluences.⁽¹⁹⁾ To determine the role of residual stresses on damage recovery and microhardness of the SiC crystals neon was used as the implant species. Inert gas atoms are insoluble in most solids but may interact with point defects to form small bubbles or clusters if there is sufficient atomic mobility.

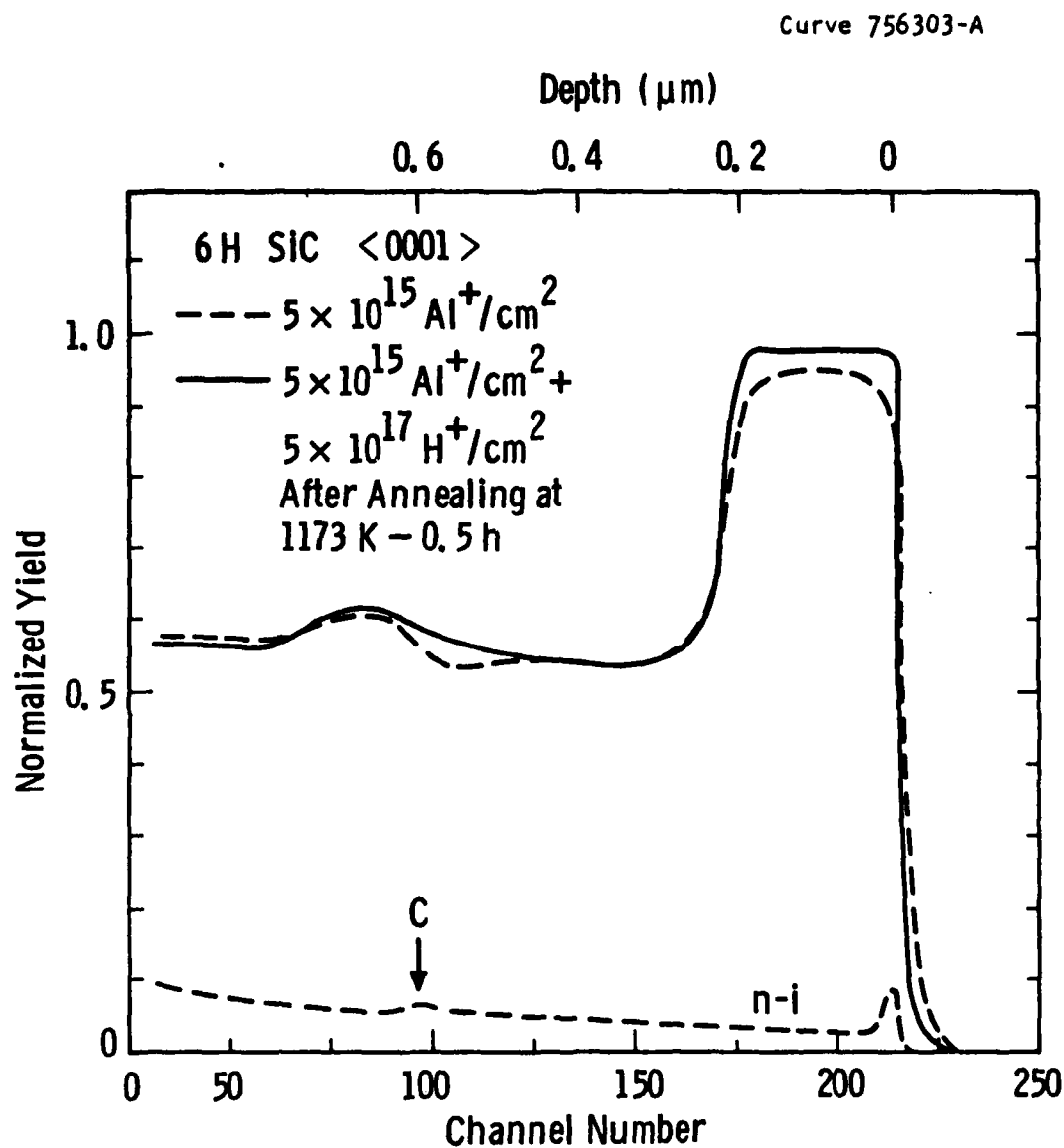


Figure 25 — RBS/channeling spectra for two 6H SiC crystals implanted with either $5 \times 10^{15} \text{ Al}^+/\text{cm}^2$ or $5 \times 10^{15} \text{ Al}^+/\text{cm}^2 + 5 \times 10^{17} \text{ H}^+/\text{cm}^2$ after annealing at 1173 K-0.5 h.

RBS/channeling spectra of a neon implanted and annealed SiC crystal are shown in Figure 26. The neon fluence, chosen on the basis of the amorphization criteria discussed in preceding sections, was sufficient to produce a randomized or metamict distribution of Si atoms from R_p to the front surface of the crystal. As described in Appendix A, similar atomic displacements have also occurred in the carbon sublattice. The direct backscattering carbon peak, however, cannot be readily unfolded from the composite dechanneling spectrum at low channel numbers because of the relative scattering efficiencies and signal to noise ratio. The displaced Si atoms are stable and very little lattice recovery occurs during successive 0.5 h anneals at increasing temperature up to 1173 K.

The corresponding effects on microhardness are given in Figure 27. Implantation at 300 K results in a measurable softening followed by a monotonic recovery to the as-grown hardness with isochronal annealing. Hardening in the as-implanted condition has only been observed in low fluence (sub-amorphization) experiments where crystallinity is maintained, Figures 11 and 13. Such hardening is due to the combined effects of the residual stresses, radiation produced defects, and, possibly, solid solution or precipitation hardening in the SiC crystals. In the current study, formation of a buried amorphous layer, or one extending to the front surface of the crystal generally results in appreciable softening prior to annealing. Boron appears to be a notable exception and will be discussed later.

The observations suggest that softening is due primarily to changes in deformation mode associated with the crystalline to amorphous transition. Mechanisms of plastic strain accommodation in amorphous materials, however, are not well understood. The recovery in KHN with annealing of the neon implanted specimen implies some concomitant change in microstructure of the ion beam modified layer. These changes may involve formation of small gas bubbles, molecular SiC clusters, islands with short range order or annealing of point defects, most of which are not detectable with RBS/Channeling or normal resolution TEM. Residual stresses may affect the propensity for radial cracking and lateral

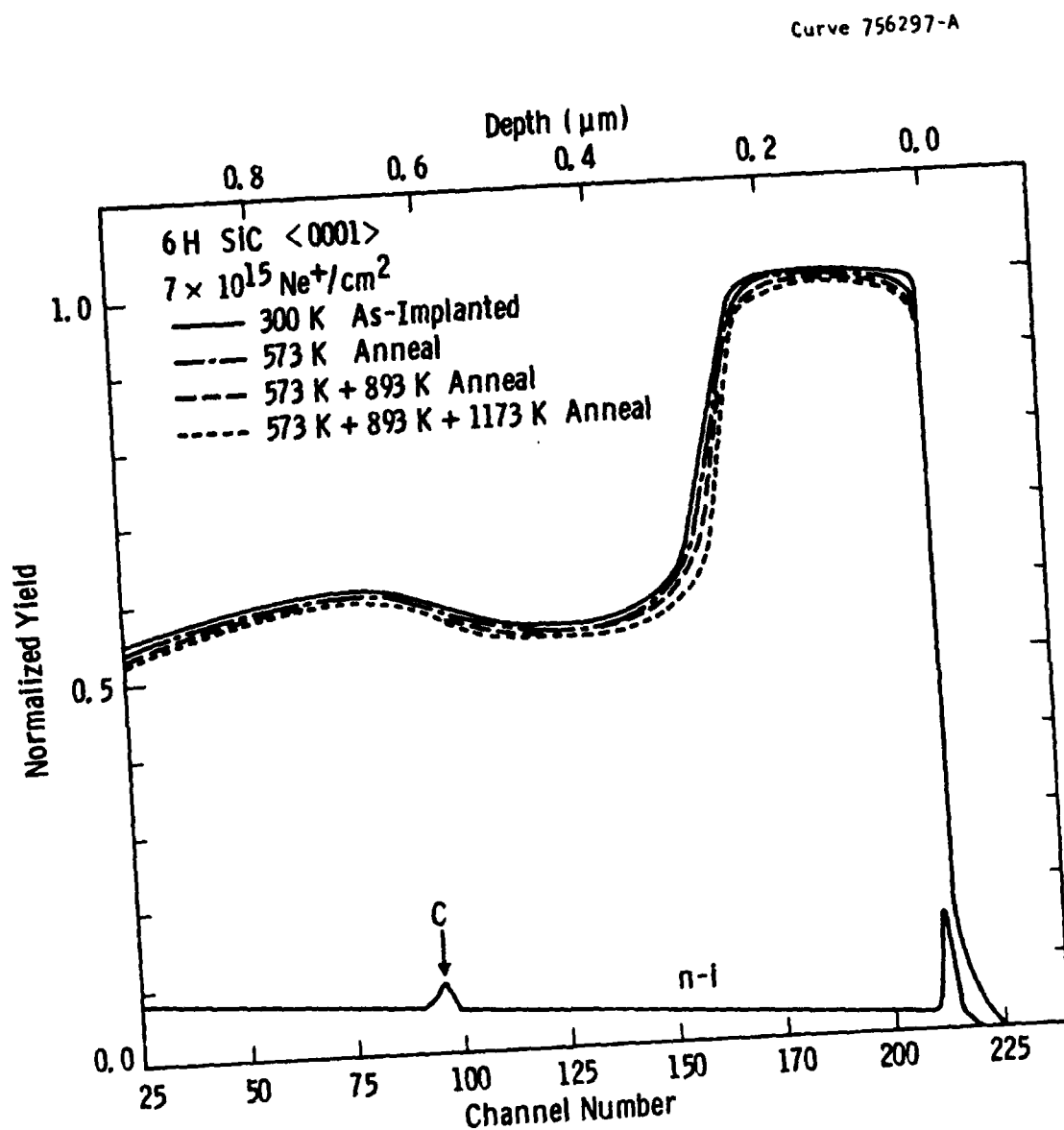


Figure 26 — RBS/channeling spectra from Ne^+ implanted and annealed SiC.

Curve 754793-B

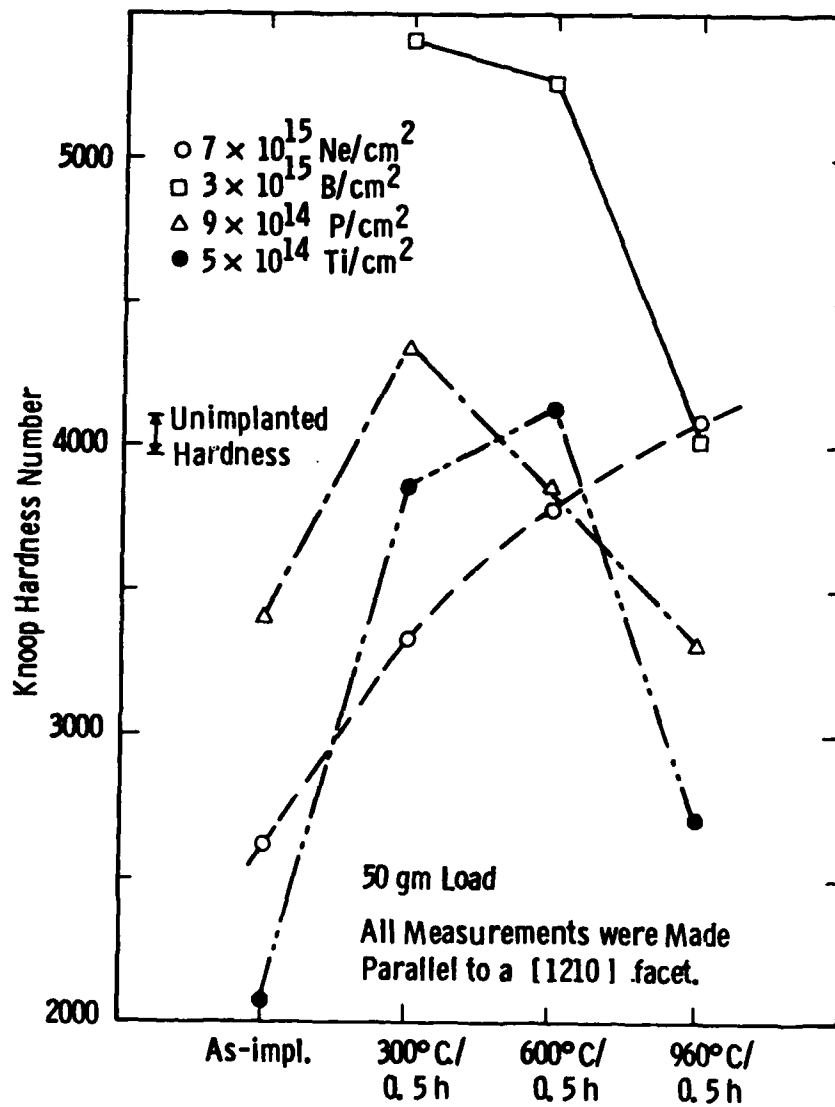


Figure 27 — Knoop microhardness measurements of Ne⁺, B⁺, P⁺ and Ti⁺ implanted and annealed 6H SiC.

fracture around hardness indentations in brittle crystalline and glassy materials, but it is unlikely that they are a principal determinant of the plastic strain accommodation observed in the high fluence implanted (randomized) and annealed SiC. This conclusion is consistent with those of earlier studies on Si and alumina crystals.⁽²⁰⁾ Definitive measurements of residual stresses (strains) by x-ray and beam deflection techniques, and atomic resolution microscopy are needed to further define the relevant phenomena.

3.2.3 Donor, Acceptor, Isovalent Dopant Effects

The motivation for conducting experiments to explore the possible effects of electrically active dopants was threefold:

- 1) Dislocation dynamics in ionic/covalently bonded materials are partially determined by charge transfer considerations;
- 2) Metal matrix composite processing parameters such as wetting, infiltration and bonding are all fundamentally associated with the electronic states of the phases involved in an interface;
- 3) Ion implantation doping and annealing to electrically activate dopants and to eliminate beam induced damage may be important in both composite material processing and development of a new class of high temperature, radiation hardened electronic devices based on SiC.

These experiments also provided an opportunity to further test the amorphization criteria discussed in Appendix A as well as the effects of atomic displacement profile on subsequent annealing response. Previous work on ion implantation of SiC, aimed principally at device applications,⁽²¹⁻³¹⁾ does not provide consistent and complete information. The annealing temperature at which considerable recovery of the lattice occurs ranges from 1023 K to 1973 K.⁽²¹⁻³¹⁾ A variety of ion species and implantation and annealing conditions were used. Frequently, the as-implanted damage profiles are either very different or are not reported at all.

RBS/channeling measurements of displacements in the Si sublattice after implantation of three dopants in the Phase II experiments are summarized in Figure 28. These experiments sought to compare the behavior of SiC implanted with boron (p-type dopant), phosphorus (n-type dopant) and titanium (isovalent dopant) at fluences calculated to produce amorphicity from $x = x_m$ to $x = 0$ and at energies corresponding to similar projected range values. While the phosphorus implant produced amorphicity over most of the expected depth range, the boron and titanium implants resulted in much narrower direct backscattering peaks. Also, the experimental x_m values show some variability. These differences are probably related, in part, to the efficiency of energy transfer for the three species. The efficiency of these ions for displacing either Si or C atoms is different because of significant mass differences with respect to both elements in the host lattice.

Table 3.1 gives the calculated maximum fraction of kinetic energy transferred in "hard sphere" collisions of ions employed in the Phase II Experiments with Si and C atoms. The calculations suggest the likelihood of different amounts of displacement damage on the two sublattices. It is not possible, however, to quantify the relative sublattice displacements without a detailed calculation of the energy transfers through multiple collisions of the "primary knock-on atoms" or PKA's and their progeny.⁽⁷⁾ This has not been performed in the current investigation. Qualitatively, B and N ions preferentially displace carbon atoms, while Al, P, and Ti ions should preferentially displace silicon atoms. Neon ions are expected to displace Si and C atoms approximately equally, and we note the excellent agreement between the predicted and observed damage profiles described previously in Figure 26. Examination of the collective RBS/channeling direct backscattering peaks and TEM data from both Phase I and Phase II as-implanted specimens indicates that the amorphization criterion holds for Al^+ , N^+ , P^+ , and Ne^+ , and but slightly underestimates the fluences required for B^+ and Ti^+ , Table 3.1. For the latter two ions, the mass of the implanted ion is either smaller than that for a carbon atom or

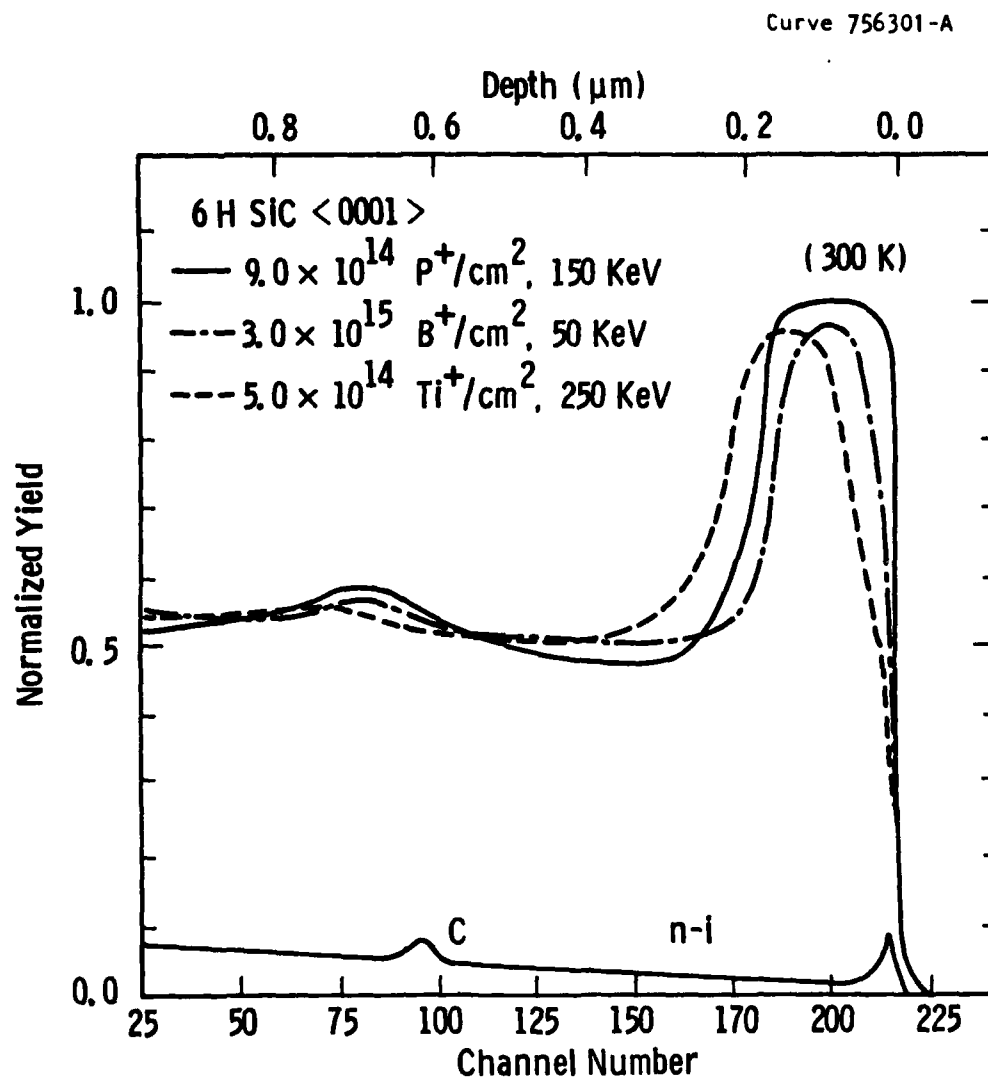


Figure 28 — RBS/channeling spectra from P^+ , B^+ or Ti^+ implanted (300 K) 6H SiC and non-implanted (n-i) masked portion of one of the crystals.

Table 3.1
CALCULATED MAXIMUM FRACTION OF KINETIC ENERGY
TRANSFERRED IN "HARD-SPHERE" COLLISIONS OF ION OF
MASS M_1 WITH SILICON AND CARBON ATOMS

Ion	M_1	Maximum Fraction ^{a)} of Kinetic Energy Transferred		Observed Extent of Amorphicity To $x = 0$
		T_{Si}	T_C	
B	10.8	0.80	0.99	No
N	14	0.89	0.99	Yes
Ne	20.2	0.97	0.94	Yes
Al	26.98	0.99	0.85	Yes
P	30.97	0.99	0.80	Yes
Ti	47.90	0.93	0.64	No

a) Calculated from $T = (4M_1M_2)/(M_1+M_2)^2$. See text Section 2.1.

larger than that for a silicon atom. The large difference in mass between the implanted ion and target atoms may cause a larger portion of the deposited damage energy to be spent in inelastic (electronic) energy loss. Consequently, less energy is spent in the elastic processes which lead to the displacement of target atoms. Therefore the critical energy densities for amorphization for these ions should be larger than for ions which have masses closer to or between Si and C.

Annealing/recovery behaviors are documented in Figures 29-31. It is interesting to note that, while some recovery was observed after the 573 K anneal for all three specimens, it accelerated at the higher temperatures for the B and Ti implants, with the latter showing the greatest reduction in damage. Clearly, the recovery behavior of the B and Ti implanted SiC specimens is not the same. This suggests that either the rearrangement of bonds to permit crystal regrowth is dependent upon the electronic nature of the dopant, or that the as-deposited damage structure was different for the two ion species. In

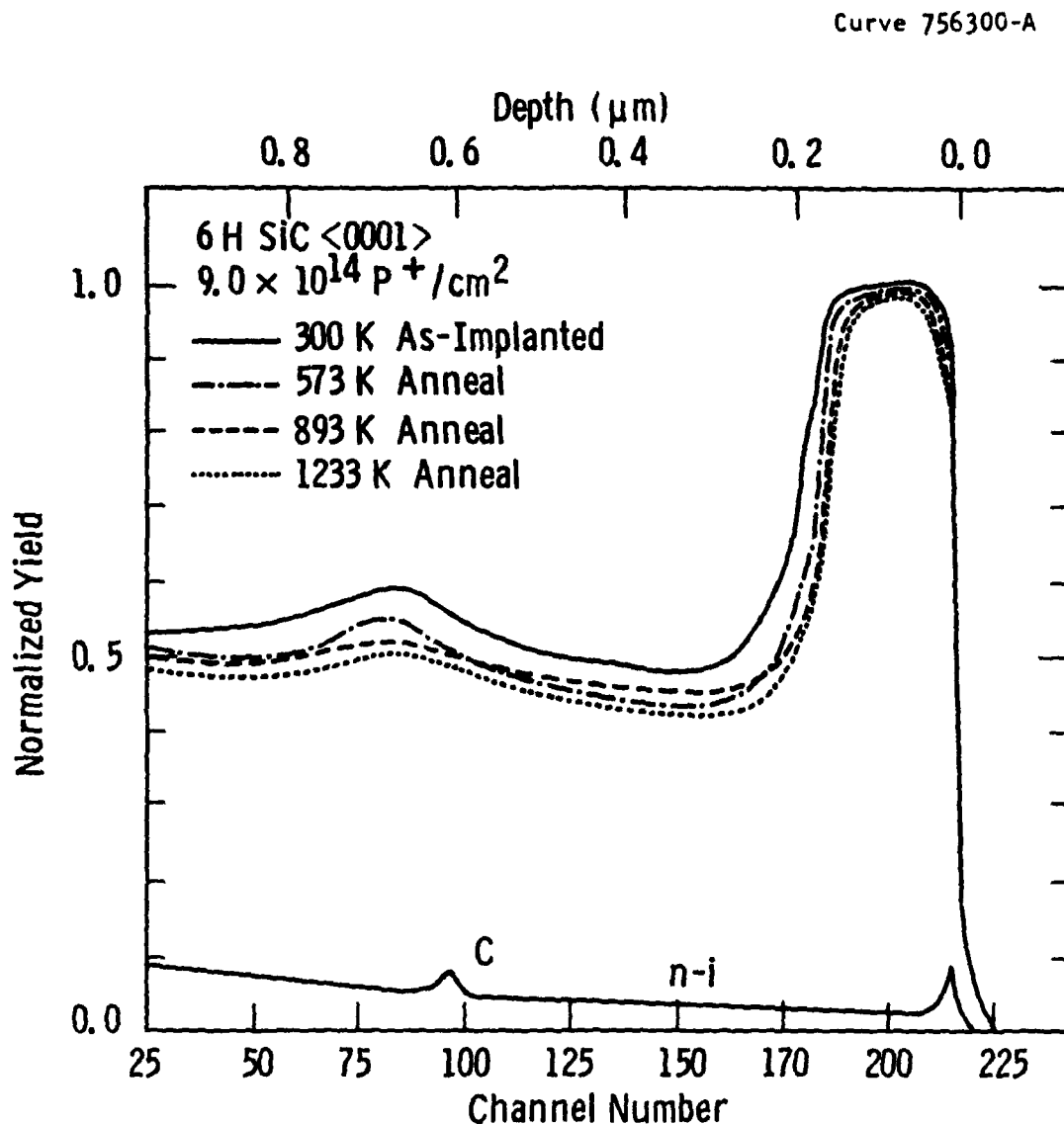


Figure 29 — RBS/channeling spectra from P^+ implanted and annealed SiC.

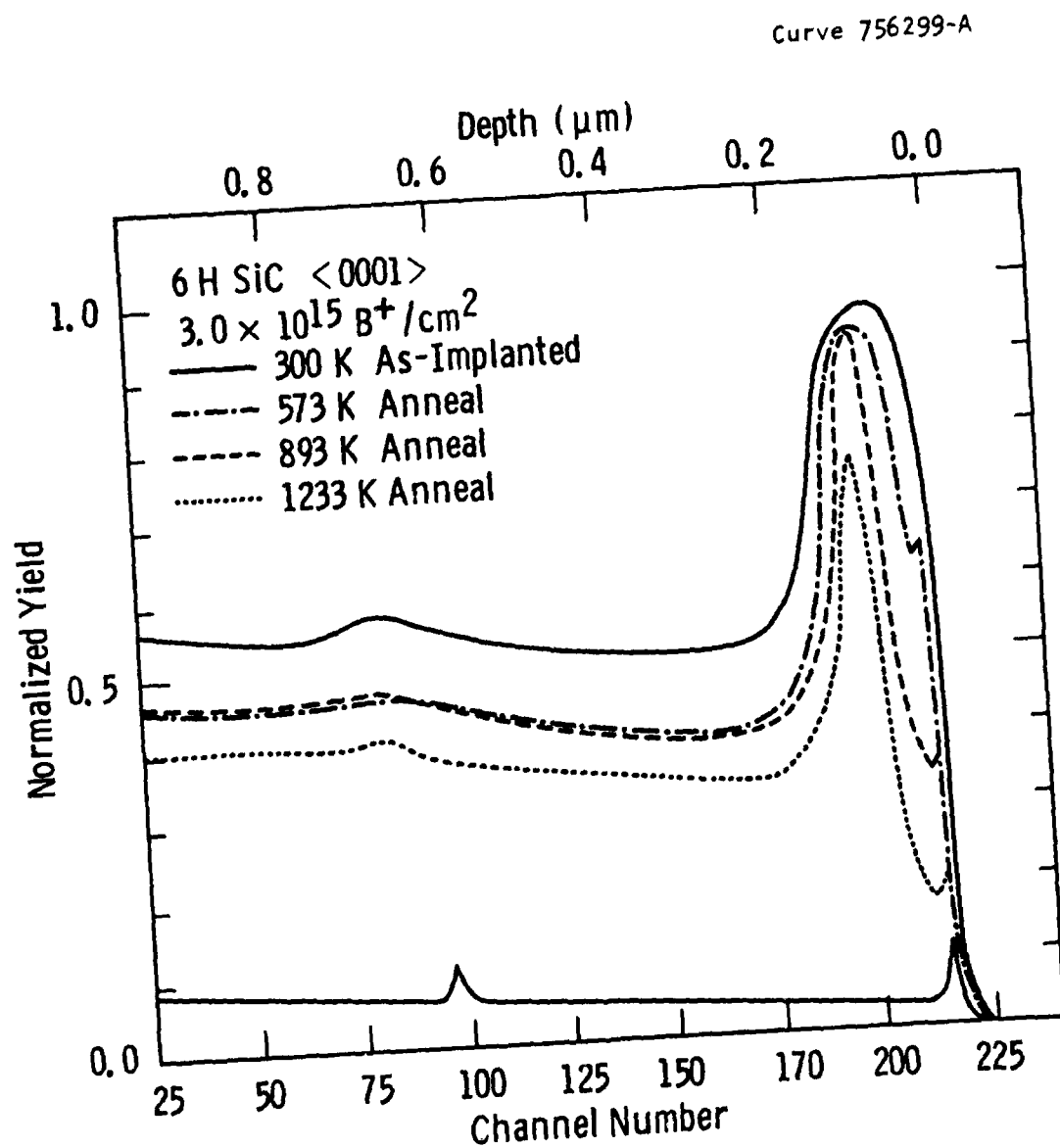


Figure 30 — RBS/channeling spectra from B^+ implanted and annealed SiC.

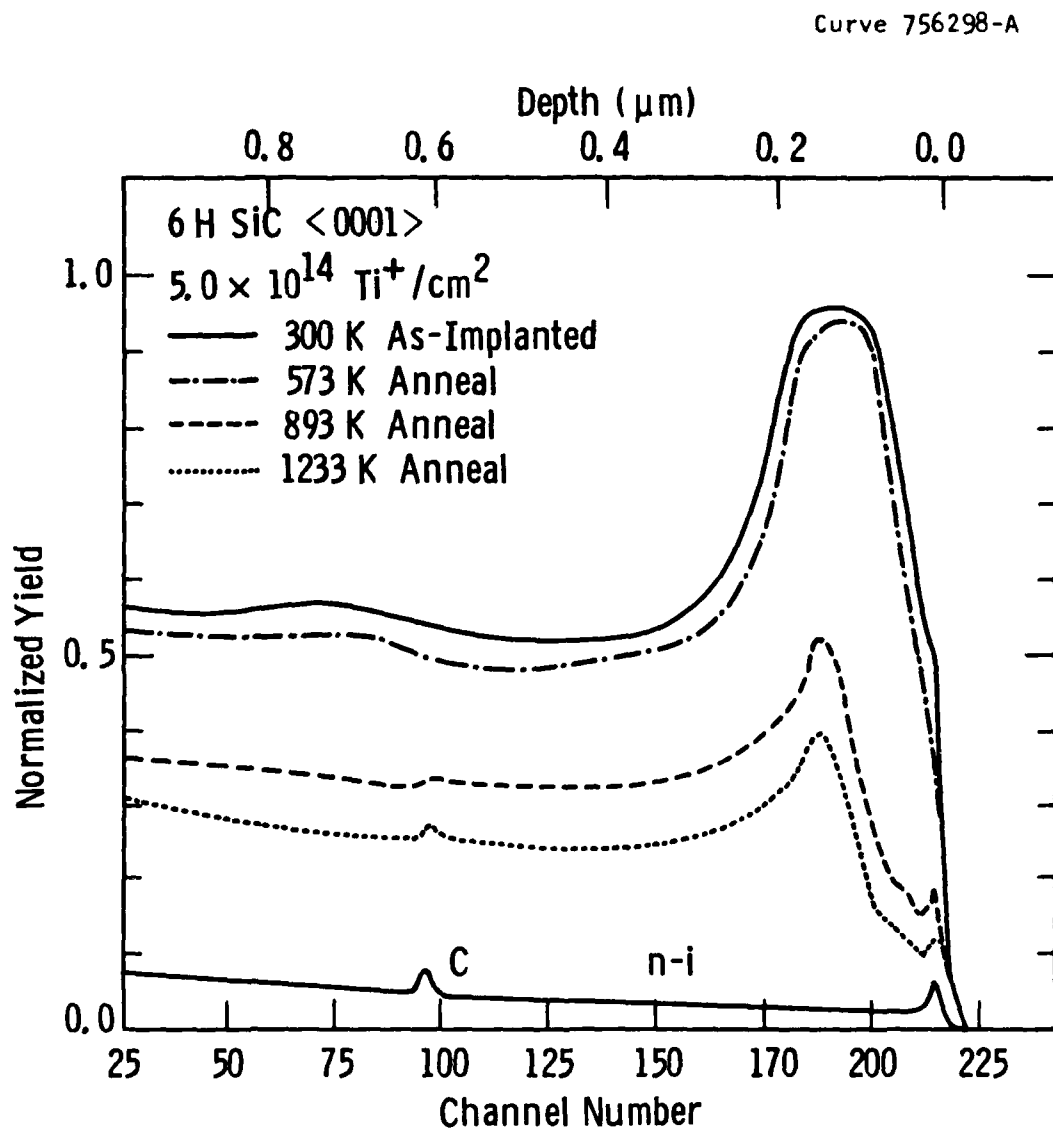


Figure 31 — RBS/channeling spectra from Ti^+ implanted and annealed SiC.

all three specimens, recovery (i.e., regrowth of single crystal SiC) occurs from both sides of the amorphous zone. However, in the P-implant, which had a broad a-SiC region extending almost to $x = 0$, minimal recrystallization is observed from the front surface. As discussed in Section 3.1.1, this lack of recovery is probably related to the absence of residual single crystal "seed" nuclei necessary for initiating the regrowth process.

As described in Appendix A, integration over the area under the Si direct backscattering peak gives the effective number of displaced silicon atoms projected per unit area of the implanted surface. The fractional damage recovery with annealing can also be described in terms of the change in area under the peak and provides an easy means for comparing effects for different ions and fluences. Figure 32 shows the results for the P^+ , B^+ , and Ti^+ implanted and annealed SiC specimens. Both the extent of recovery after the isochronal anneals and the rate of recovery are different for the three crystals. Comparison with Figure 33, however, indicates that some of the differences may be explicable entirely on the basis of different initial damage states prior to annealing. Figure 33 was obtained by applying the integration procedures to the data of Figures 6 and 7. The annealing behavior of the Ti^+ implanted sample is very similar to the Al^+ doped crystal which was also implanted to produce a buried amorphous layer near x_m , but insufficiently heavily for the amorphous region to reach the surface. Similarly, the annealing behavior of the P^+ implanted sample closely resembles the data for the Al^+ implant of highest fluence. For the B^+ implanted sample, the situation is less clear. The annealing behavior is consistent with an initial damage profile between those shown for an Al^+ implanted crystal with a amorphous region extending to the surface and a more heavily doped and damaged region. However, this does not agree with the RBS/Channeling curve for the as-implanted boron doped crystal in Figure 28. The possibility of chemical/electronic effects of the dopant on regrowth of the SiC crystal for the boron cannot be entirely ruled out.

Curve 756304-A

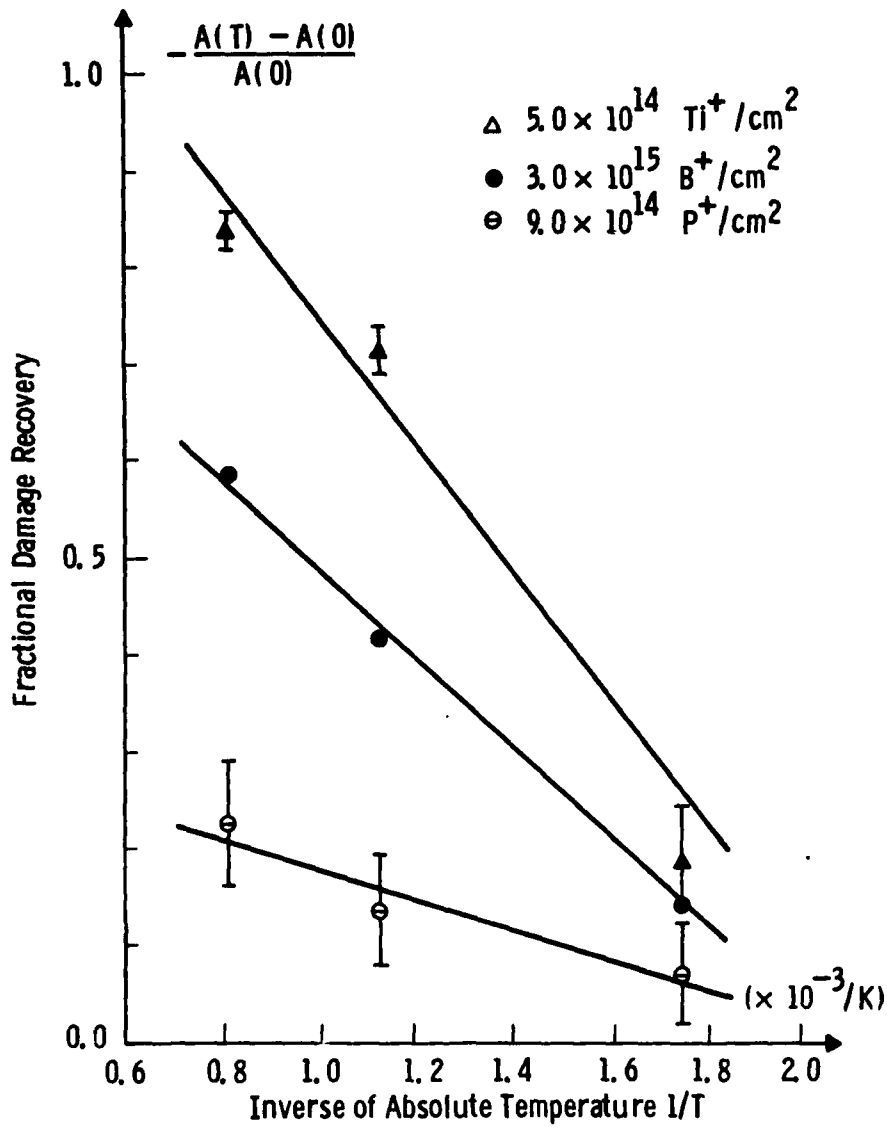


Figure 32 — Temperature dependence of damage recovery calculated from integration over the area under the Si direct back-scattering peak for B^+ , P^+ and Ti^+ implantation.

Curve 756305-A

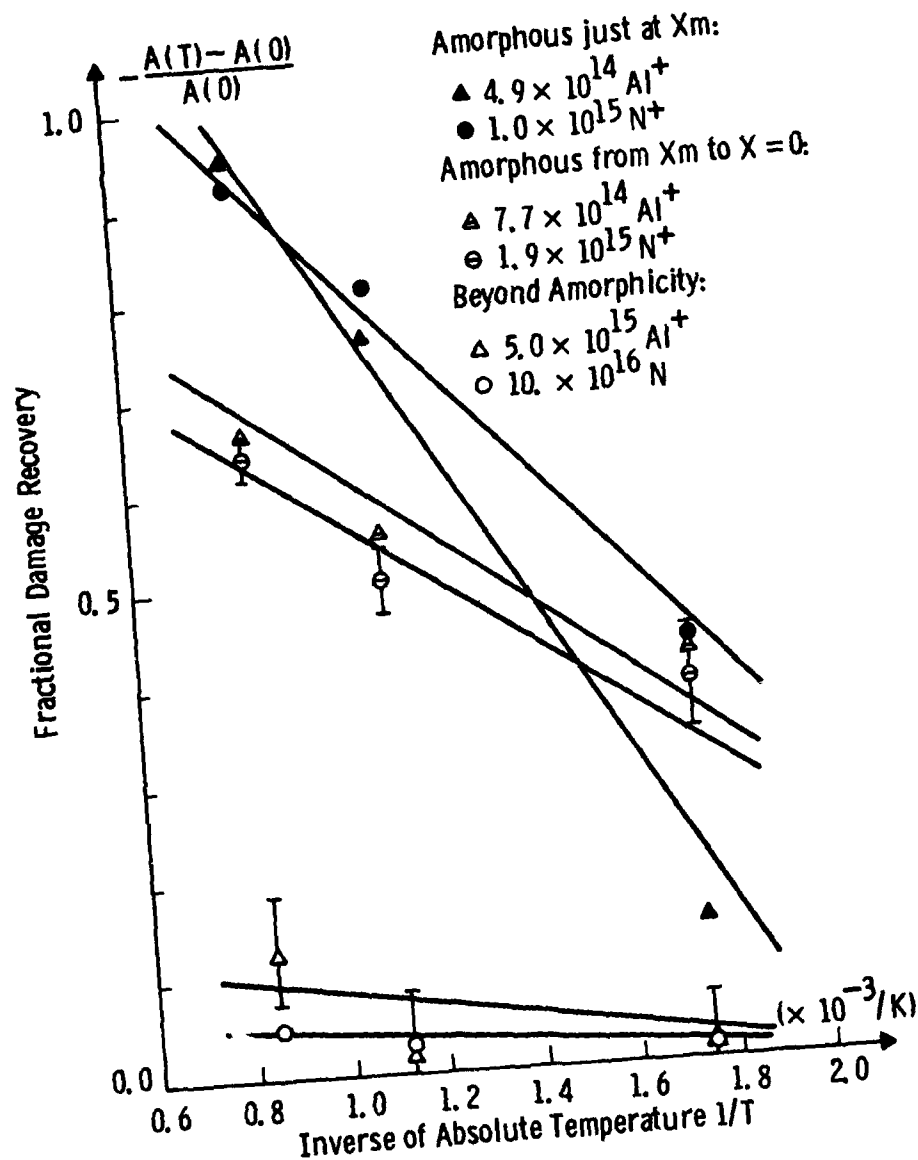


Figure 33 — Temperature dependence of damage recovery calculated from integration over the area under the Si direct back-scattering peak for Al^+ and N^+ implantation at different fluences.

A similar comparison can be made with the previous work on N^+ implants, Figure 33. Since Al and N are also p- and n-type dopants, respectively, most of the annealing kinetics appear to be determined mainly by the initial damage state rather than the nature of the implant species.

Although activation energies could be extracted from this data it is unlikely that a simple interpretation is possible, at present. A wide range of competing and overlapping processes including solid phase epitaxial regrowth, recrystallization and formation of polycrystals from remnant nuclei, annealing of point defects, etc., have been identified by high resolution TEM studies in ion implanted semiconductor grade silicon, for example.⁽¹⁸⁾ The key finding, here, is that the annealing behavior for SiC crystals with similar initial damage profiles is generally independent of implant species. The chemical/electronic properties of these dopants, with the possible exception of boron, apparently do not strongly affect the recovery rate for samples implanted at 300 K and subsequently annealed in vacuum.

Knoop microhardness measurements for the B^+ , P^+ and Ti^+ implanted and annealed SiC crystals are presented in Figure 27. It was not possible to obtain a valid hardness number for the boron doped crystal in the as-implanted condition because of extensive lateral fracturing due to the very brittle nature of the surface. The hardness data indicate a definite dependence of the near-surface mechanical properties on the dopant. Phosphorus and titanium (and neon) implantation produced softening. Boron implantation hardened and embrittled the surface. The boron effect is similar to the hardening observed in the low fluence implantation of aluminum in the Phase I experiments, but the effect is much larger for boron. The hardening is probably attributable to a combination of solid solution, precipitation and solute-defect strengthening mechanisms in the SiC crystals. Annealing at 1233 K results in complete recovery to the unimplanted hardness level.

As discussed in an earlier section, and demonstrated by the neon implantation effects on hardness, creation of an amorphized damage zone tends to soften the near surface region. Thus, on the basis of the RBS/channeling results, it was anticipated that the phosphorous implanted sample would have a lower KHN value than the titanium implanted crystal. The converse is true, Figure 27. Moreover, with post-implantation annealing, both the P^+ and Ti^+ doped samples first recover to the unimplanted hardness level then soften again at the highest annealing temperature. It is concluded that the near-surface mechanical properties, as reflected in indentation response, depend on the chemical/electronic nature of the implant species as well as on the number of atomic displacements.

In an attempt to understand these effects further, several tasks were initiated. Cross-section TEM, Raman spectroscopy and Secondary Ion Mass Spectroscopy (SIMS) studies were attempted at the Westinghouse R&D Center, the University of Pittsburgh and the Physical Electronics Laboratory of Perkin Elmer, Inc., in Edison, NJ, respectively. Difficulties in achieving "routine" preparation of XTEM specimens were described previously and could not be resolved within the time and funding limitations. Low signal to noise ratios in the Raman and SIMS measurements precluded definitive interpretation of the changes in atomic bonding and near surface chemistry. The data are confusing and are omitted for brevity. Additional development work is required for application of these techniques to ion implanted SiC crystals. Details of the experimental difficulties can be obtained directly from the authors of this report. In retrospect, AES measurements on the P^+ , B^+ and Ti^+ implanted crystals would have provided the best data for applications to processing of metal matrix composites. However, RBS and SIMS measurements (with sputtering to obtain depth profiles in SIMS) eliminated the possibility of conducting AES studies on pristine surfaces, without preparation and implantation of a new series of crystals.

Table 3.2 summarizes the calculated average concentrations of implanted solute for the Phase II samples and reference data for high temperature solubility. The implanted ion concentrations, although generally small from alloying considerations, are comparable to intrinsic carrier concentrations at elevated temperatures. Thus, by analogy with observed effects in Si,⁽³²⁾ one would anticipate effects on

Table 3.2
CALCULATED AVERAGE CONCENTRATIONS OF IMPLANTED SOLUTE^{a)}

Ion	Fluence ₂ Ions/cm ²	ΔR_p (μm)	Concentration Atoms/cm ³ , (a/o)	High Temp. Solubility Ref. 33	Ref. 34
N	5×10^{17}	0.0326	6.5×10^{22} (68)	2×10^{20}	$>10^{20}$
Al	2×10^{17}	0.0303	2.8×10^{22} (29)	$>2 \times 10^{19}$	10^{21}
B	3×10^{15}	0.0337	3.8×10^{20} (0.4)	8×10^{18}	10^{19}
P	9×10^{14}	0.0260	1.5×10^{20} (0.2)	1×10^{18}	10^{18}
Ti	5×10^{14}	0.0238	8.9×10^{19} (0.1)	--	--
Al	7.7×10^{14}	0.0303	1.1×10^{20} (0.1)	$>2 \times 10^{19}$	10^{21}
N	1.9×10^{15}	0.0326	2.5×10^{20} (0.3)	2×10^{20}	$>10^{20}$

a) Calculated using equation (2-1).

dislocation mobility in the SiC crystals. In addition, comparison of implanted concentrations and published solubility limits indicates that the dopants for both Phase I and Phase II experiments probably exceeded solubility limits at the low implant and anneal temperatures. Hence, both solid solution and precipitation effects could have contributed to the observed changes in indentation response and surface chemistry with implantation and annealing. The solubility data in Table 3.2 can only be used as a guideline because they apply to undamaged SiC crystals near thermodynamic equilibrium at high (1660 K to 2800 K) temperatures.

3.2.4 Response to Composite Fabrication

To evaluate the stability of an ion beam modified microstructure under point contact stresses and thermal cycling during hot pressing of a powder metallurgy aluminum matrix composite the following experiment was performed. One $\langle 0001 \rangle$ face of a 6H SiC crystal was implanted with $5 \times 10^{15} \text{ Al}^+/\text{cm}^2$ at 150 keV at 300 K. This fluence was sufficient to produce an amorphous damage zone extending from the peak damage depth, x_m , to the front surface. The damage profile and hardness were determined immediately after implantation by RBS/Channeling and microhardness measurements. The implanted crystal was then placed in a 2.5 cm I.D. graphite die on top of a 3 cm thick layer of -200 mesh 1100-0 aluminum powder. An additional 3 cm of powder was added to the die on top of the crystal. The die was placed in a hot pressing chamber which was then evacuated to $1.3 \times 10^{-2} \text{ Pa}$. A preprogrammed temperature-pressure cycle was imposed to consolidate the "composite". Maximum composite temperature during processing was 900 K and the maximum pressure was approximately 28 MPa. The cycle was sufficient to produce a composite Al/SiC "billet" with density greater than 99.5% of theoretical. Following consolidation, the billet was placed in concentrated HCl to dissolve the aluminum. The SiC crystal, which had not fragmented or cracked, was then recovered and re-examined by RBS/Channeling and microhardness techniques.

The RBS/channeling results are summarized in Figure 34. Data from a control crystal, implanted under identical conditions but subjected to the three step 0.5 h isochronal annealing sequence discussed in previous sections, are also shown. It is concluded that contact pressure from the powder particles and the thermomechanical cycle did not affect the stability of the microstructural modifications in the ion implanted crystal. Similar conclusions hold for the indentation hardness (not shown) which was nearly identical to that measured for thermally annealed control specimens. The results of this experiment suggest that similar ion beam modifications of SiC whiskers or crystalline particulate would provide stable, predictable properties for MC fabrication and processing.

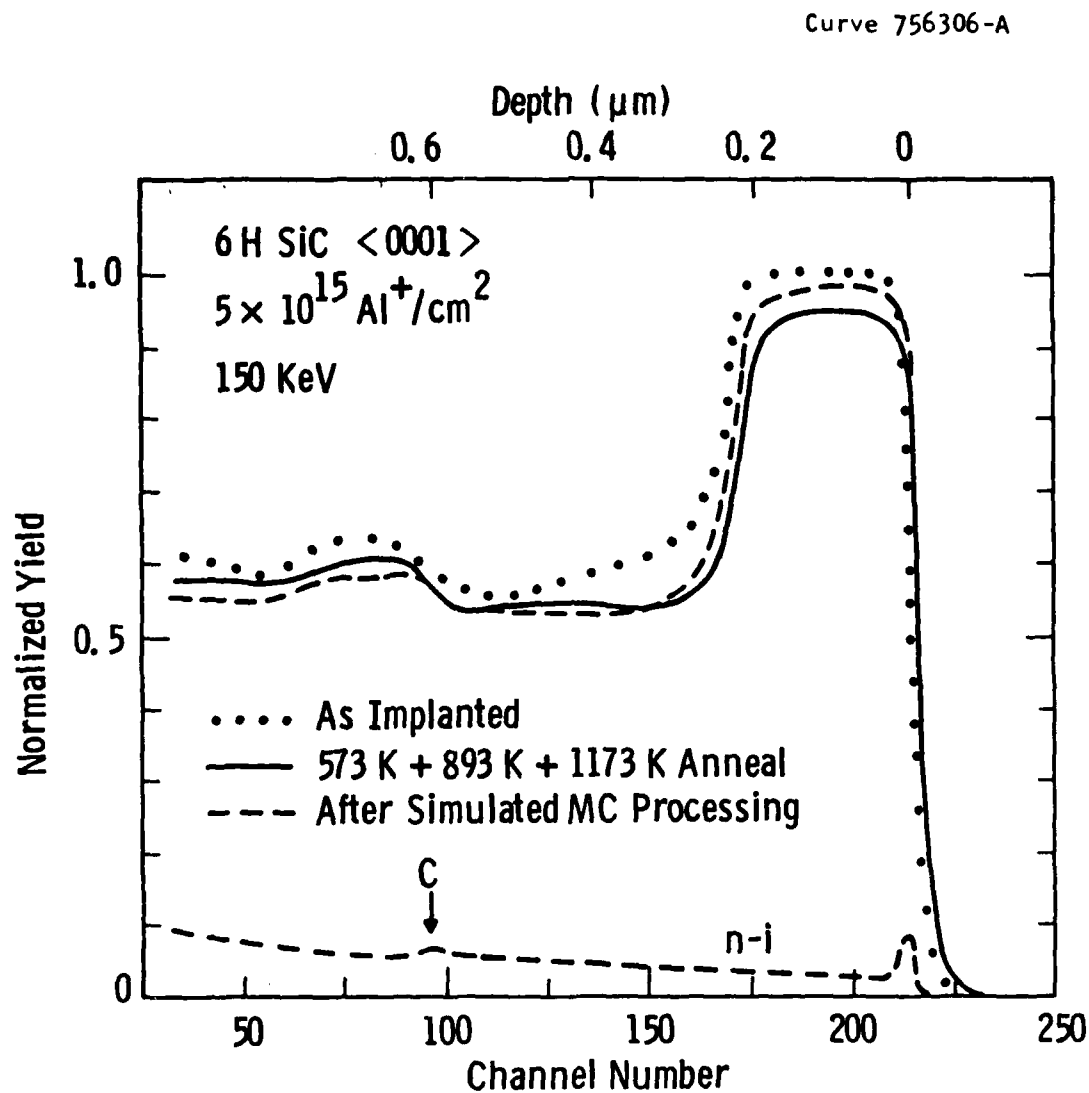


Figure 34 — Comparison of RBS/channeling spectra from Al^+ implanted 6H SiC crystals subjected to isothermal vacuum annealing or metal matrix composite fabrication (hot pressing) thermomechanical cycle.

3.3 MECHANICAL PROPERTIES AND WETTING OF ION IMPLANTED SiC WHISKERS

Two approaches were considered to evaluate effects of ion beam modified SiC surfaces on metal matrix composite properties. The first was to directly implant sufficient quantities of particulate or whisker material to permit fabrication of Al alloy/SiC_p or Al alloy SiC_w composites for tensile, fatigue and fracture toughness testing. The second was to take a more fundamental approach to the relevant issues of fiber strength, wettability, bonding, etc., by carefully selecting a small number of fibers, implanting them, and subjecting them to a series of studies. Sufficient experimental capabilities had been developed at the Westinghouse R&D Center under previous funding to achieve the necessary implantation(s) for either approach. However, the amount of material required for the first option corresponded to several square meters of implanted surface. For the desired fluence ranges and low flux levels required to control beam heating, these experiments would have required expenditures of time and funds in excess of remaining program resources. In addition, optimization of processing variables, e.g., controlling build-up of a surface charge and ensuring uniform average exposure to the incident beam, would have required appreciable effort. Thus, it was decided to pursue evaluation of implantation effects on individual fibers.

Two sets of SiC whiskers were available. One was a lot of ARCO fibers provided by our Contracting Officer, Dr. Stephen Fishman of ONR. The second was one batch of material grown by the vapor-liquid-solid (VLS) process at Los Alamos National Laboratory and supplied by Dr. John Petrovic of LANL. Characterization of several dozen whiskers from each set by optical microscopy and SEM indicated that the high purity crystalline material grown by the VLS process was the better choice for these experiments. In addition, LANL had conducted extensive microtensile tests on VLS whiskers and expressed interest in collaborative efforts to evaluate the effects of ion implantation on this material. Figure 35 demonstrates the range of variability in thickness and triangular cross-section of the VLS whiskers in this lot.

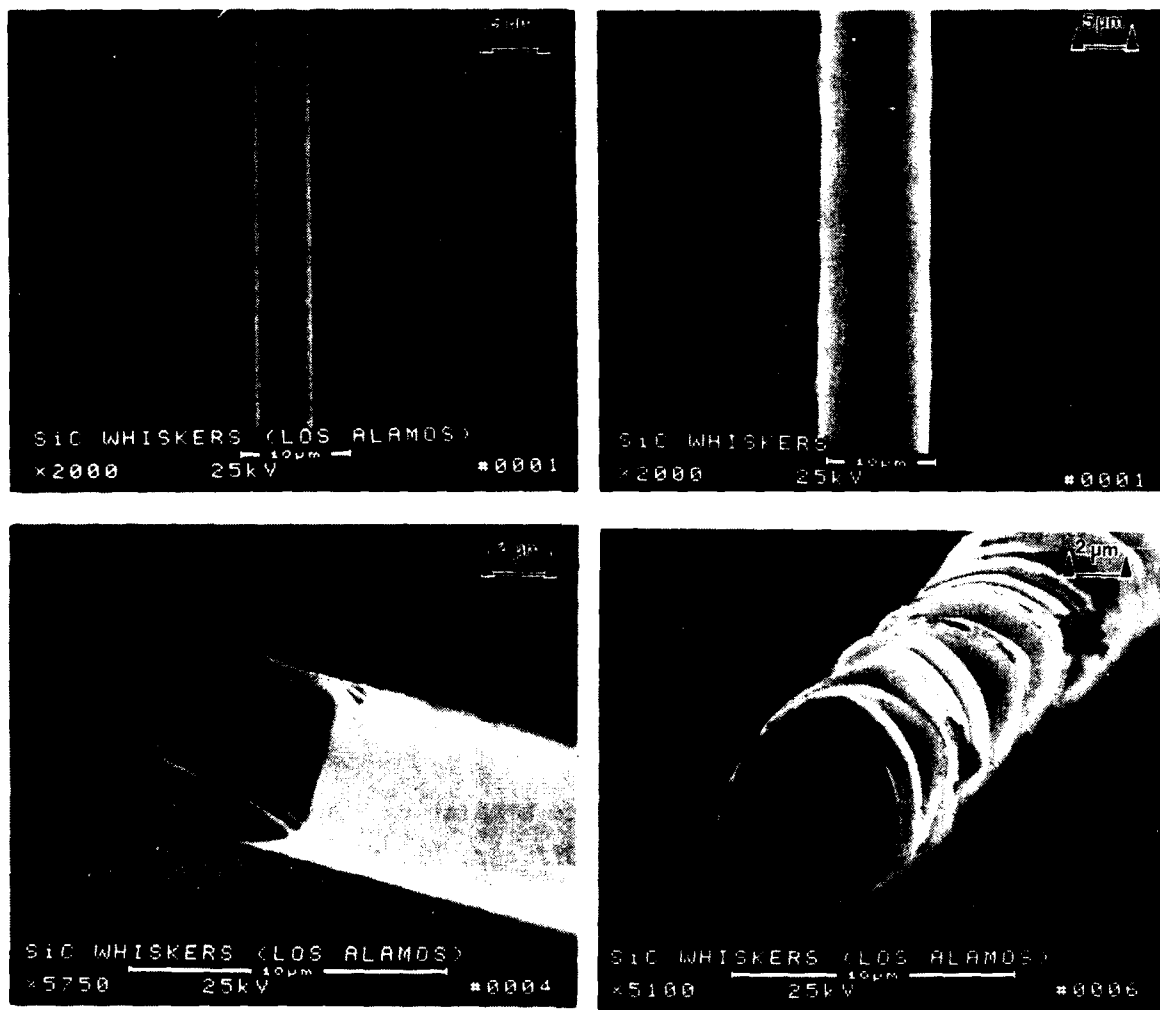


Figure 35 — Morphology variability in as-received Los Alamos whiskers.

Dr. Petrovic, aware of the variability, suggested that fibers for the experiments be selected on the basis of their uniformity by SEM characterization. Most of the whisker specimens were selected on the basis of this screening.

Based on the single crystal 6H SiC results it was decided to implant several whisker batches with B^+ , P^+ , Al^+ or N^+ . The fluences and incident kinetic energies selected have been summarized in Table 2.4. As described in previous sections, boron resulted in anomalous hardening of the surface. Phosphorus resulted in softening characteristic of an amorphized zone extending from the peak damage region to the front surface. Aluminum and nitrogen also resulted in different indentation hardness and lateral cracking/fracture in as-implanted and annealed conditions. Moreover, formation of a C-rich (Si poor) region and formation of a buried nitrogen affected region adjacent to the implanted $\langle 0001 \rangle$ surface of the SiC crystal was observed for high fluence N^+ implantation but not for high fluence Al^+ implantation. Thus, selection of these ions was expected to permit studies of the principal microstructural and microchemical effects induced by ion beam modification.

The experimental techniques for positioning the fibers during implantation, controlling beam heating effects, etc. have been described in Section 2.4. Several batches of implanted fibers have been sent to LANL for mechanical testing. It is anticipated that results will become available when time and funding permit further evaluation. Additional mechanical studies of effects on bonding using David Marshall's (Rockwell) "Fiber Driveout" technique would have been valuable and, hopefully, will be conducted in the future. Additional studies at the Westinghouse R&D Center have focused on development of a suitable means to evaluate the magnitude of the ion implantation effects on wetting of the whisker surfaces. Several preliminary attempts using a variety of techniques, which will be described briefly, have been undertaken. However, no definitive data are yet available because additional technique development will be required.

Since no facilities exist within the laboratory for conducting quantitative sessile drop experiments with the flat 6H SiC single crystals, efforts have been directed toward a phenomenological evaluation of wetting of the VLS whiskers. Two approaches have been tried to date. The first entailed evaporation of aluminum onto the fiber surfaces in high vacuum followed by short heating cycles to a maximum temperature of 973 K to melt the aluminum. Evaporated film thicknesses ranged from 0.05 μm to 0.2 μm to ensure coverage beyond the "island" stage. SEM characterization techniques were used in an attempt to determine the degree of wetting. Figures 36 and 37 show typical micrographs of the deposited and annealed film structure, respectively, for an unimplanted whisker. Plan views in Figures 36b and 37a indicate some smoothing of the as-deposited granular film after annealing. At 50° tilt, Figure 37b, some granularity can be seen. Several difficulties with this approach quickly became apparent. Film structure was very dependent on film thickness and varied considerably from area to area on a given whisker. No clear evidence of a lack of wetting was ever observed making it difficult to quantitatively and qualitatively describe the subtle effects. Finally, it is suspected that the film response was dominated by formation of a stable, thin, reacted metal oxide overlayer.

A second phenomenological approach involved direct submersion of unimplanted and implanted whiskers in a superheated melt pool of Al 2024 alloy. The whiskers were first mounted in V-shaped, 0.8 mm deep grooves electro-discharge machined into stainless steel plates. Other substrates were tried but the low thermal conductivity of the steel and the ease of wetting with molten aluminum minimized the amount of superheating required. Whiskers were "tacked down" at both ends in each groove with Saueriasen 350 Cement, and the assembly was preheated in a protective argon atmosphere. The aluminum alloy was melted under the same protective atmosphere. Just prior to dipping the stainless steel plate into the molten pool, oxide "scum" was scraped off the pool surface exposing clean molten metal. Bath temperature was maintained at

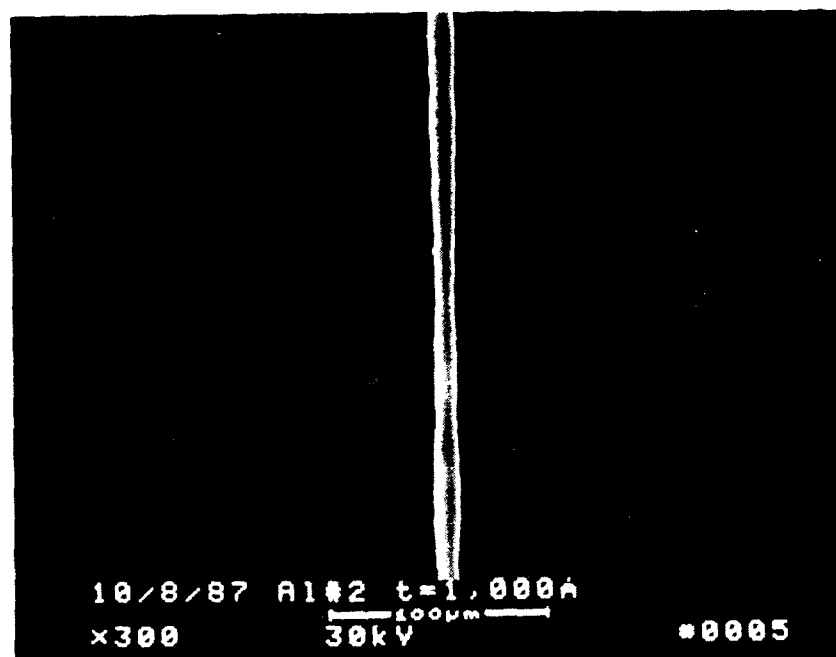


Figure 36 — Los Alamos VLS SiC whisker (unimplanted) with as-deposited 100 nm thick Al film (plan view).

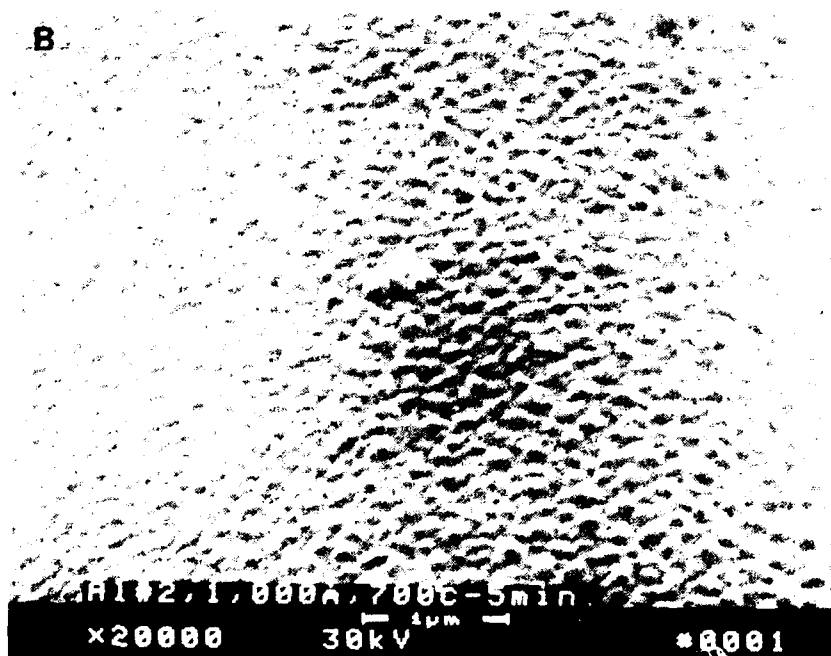
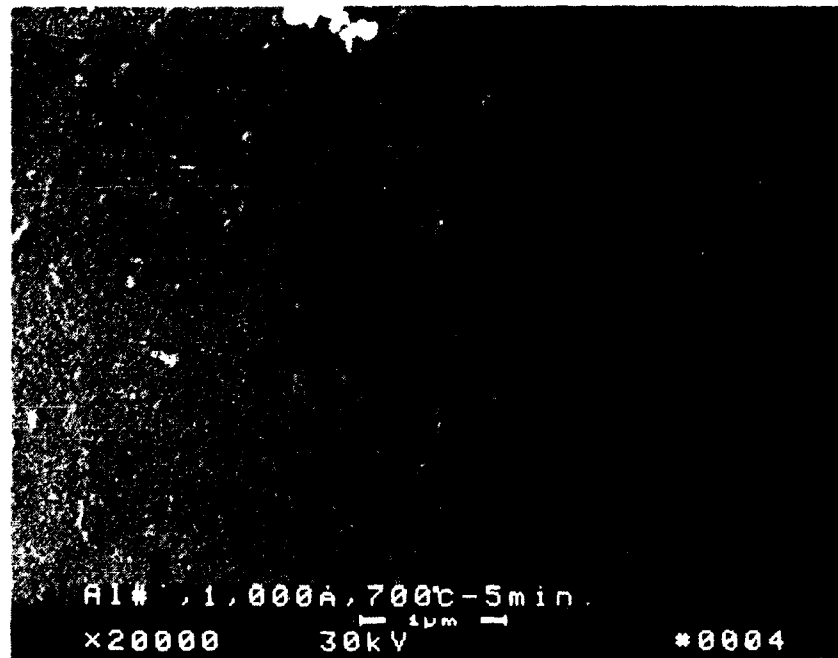


Figure 37 — Los Alamos VLS SiC whisker (unimplanted) with 100 nm Al film after 973 K-0.5 min vacuum anneal. a) plan view; b) 50° tilt.

968 K to 973 K \pm 5 K. Superheating was required to facilitate wetting within the grooves and around the fibers without freezing a "bridge" over the top of the channels. The plate was immersed at the optimal contact angle to the melt and held for approximately 1 minute while the pool was lightly agitated by stirring with the plate to enhance liquid penetration into the grooves. After solidification the plates were sectioned. Cross-sections were mounted and polished for metallographic observations. Reliable, reproducible data on wetting of whisker surfaces using this approach have not yet been demonstrated. Freeze-over or "bridging" of the channels has not been entirely eliminated. In addition, thermal stresses during solidification and cooling cause severe contraction of the Al film. This, in turn, causes fracturing and, usually, loss of unwetted or poorly wetted whiskers. It is recommended that further studies be directed at obtaining wetting angles on larger ion implanted SiC crystals and examination of fiber "pullouts" on fracture surfaces of bulk specimens fabricated with implanted whiskers or particulate as the reinforcing phase.

4. SUMMARY AND CONCLUSIONS

High purity single crystals of 6H SiC and VLS whiskers of SiC have been implanted at 300 K with a variety of ions including H, B, N, Ne, Al, P, and Ti. Changes in microstructure, mechanical properties and composition in the near-surface region following implantation and isochronal annealing in stages up to 1173 K have been selectively examined with a combination of RBS/channeling, TEM, SEM, microhardness and AES techniques. Additional characterization efforts involving microtensile measurements of whisker strength, SIMS profiles, Raman Spectroscopy and wetting of implanted and annealed crystals and fibers were initiated but have not been completed owing to experimental difficulties and funding limitations.

Principal conclusions of this study are:

1. The critical deposited damage energy to produce a metaminct (randomized or amorphous) state in SiC is 2×10^{21} keV/cm³ for N, Al, P, and Ne ions. A slightly higher deposited damage energy is required for B and Ti ions which are lighter or heavier than C and Si atoms, respectively.
2. Annealing of the metaminct structure and recovery of the crystalline Si sublattice is suppressed for annealing temperatures up to 1173 K for all implanted ions if the metaminct structure extends from the peak damage region, x_m to the front surface at $x = 0$.

3. Regrowth occurs from both the underlying undamaged substrate and from remanent crystalline nuclei near $x = 0$ at fairly low annealing temperatures (> 573 K) if the metaminct microstructure is not achieved at $X = X_m$ or does not extend to the front surface.
4. The implanted dopant atoms are immobile at 300 K but interact with the defects produced by atomic displacement thus stabilizing the damage. Because of this, the peak damage region coincides with the calculated projected range.
5. The average concentrations of some of the implanted ions are comparable to intrinsic carrier concentrations at elevated temperatures and exceed extrapolated solubility limits for the respective solutes.
6. Annealing mechanisms and recovery rate depend on the number of atomic displacements but are relatively insensitive to the chemical/electronic characteristics of the implanted ions with the possible exception of boron.
7. Al and B implantation increases the indentation microhardness at low fluences. P, Ne and Ti reduce the hardness. Nitrogen implantation dramatically alters radial cracking and lateral fracture response to indentation loads.
8. Fluences required to induce significant hardness changes in these high purity single crystals are two orders of magnitude lower than previously reported.
9. Residual stresses may affect radial cracking and lateral fracture but are small compared with the measured hardness effects.
10. Implanted hydrogen does not promote bond reconstruction or alter dopant effects on indentation hardness.

11. With the exception of the Ne implanted samples which show a monotonic recovery in hardness with isochronal annealing steps, hardness effects are complex and depend on the chemical/electronic nature of the implanted ion.
12. Hardness can recover without any discernible recovery in the direct backscattering Si peak measured by RBS/channeling.
13. High fluence nitrogen implantation results in pronounced changes in surface composition. A 100% carbon layer is produced which extends approximately 60 nm into the crystal. Carbon and silicon stoichiometry are affected over a large depth. Oxygen enrichment in the nitrogen doped region is also observed. High fluence Al ion implantation does not produce measurable changes in C, Si or O profiles.
14. AES and preliminary SIMS measurements suggest that the implanted ions have widely different mobilities at annealing temperatures up to 1173 K.
15. Thermomechanical processing and point contact stresses accompanying fabrication of a powder based aluminum/SiC composite do not significantly perturb the predicted microstructural and microchemical changes in ion implanted SiC.
16. Results of 300 K implantation and vacuum anneals can probably be used to model SiC/Al interface properties expected after elevated temperature fabrication of a composite microstructure.
17. It is possible to predict and control beam heating effects to permit direct implantation of SiC whiskers.

18. SiC whiskers grown by the vapor-liquid-solid process at Los Alamos National Laboratory have been successfully implanted with B, N, Al, and P to cover the range of phenomena described above. The whiskers have been sent to LANL for microtensile tests as time and funds permit.
19. Further evaluation of the effects of implantation and annealing on wetting of SiC surfaces by molten metal should focus on sessile drop experiments and quantitative analysis of fiber pullouts.

5. ACKNOWLEDGMENT

We gratefully acknowledge the assistance provided by our colleague, Professor W. J. Choyke, of the Physics and Astronomy Department at the University of Pittsburgh, in the planning and execution of this program. The ion implantation was conducted by Mr. N. J. Doyle at the Westinghouse R&D Center. RBS/channeling measurements were made possible through the diligent efforts of two graduate students, J. Bradshaw and J. Ruan, at the University of Pittsburgh. Critiques by Professor R. P. Devaty (Physics Department, University of Pittsburgh) were most helpful. The assistance of Dr. Mehmet Gungor, Mr. E. Martin and Mr. R. Blackburn of the Westinghouse R&D Center in the fiber wetting experiments are also gratefully acknowledged.

6. REFERENCES

1. J. W. Mayer, L. Eriksson, and J. A. Davies, Ion Implantation in Semiconductors, Academic Press: New York (1970).
2. G. Dearnaley, J. H. Freeman, R.S. Nelson, and J. Stephen, Ion Implantation, Vol. 8, Defects in Crystalline Solids, North Holland: Amsterdam (1973).
3. G. Carter and J. S. Colligon, Ion Bombardment of Solids, American Elsevier Publishing Co., Inc.: New York (1968).
4. J. Lindhard, M. Scharff, and N. E. Schiott, Mat.-Sys. Medd Dan. Vidensk Selsk., Vol. 36, No. 14 (1963).
5. I. Manning and G. P. Mueller, Computer Physics Communications, 6 (1973).
6. J. N. McGruer, D. S. Croft, R. B. Irwin, J. A. Rabel, J. H. Sheehan, W. J. Choyke, and N. J. Doyle, Proc. of the Fourth International Conf. on Ion Implantation: Equipment and Techniques, Berchtesgaden, Federal Republic of Germany, 13-17 September 1982, H. Ryssel and H. Glaweschung, editors, Springer-Verlag: Berlin (1983).
7. R. M. More and J. A. Spitznagel, Radiation Effects, 60: 27 (1982).
8. E. Dartyge, Radiation Damage Processes in Materials, C. H. S. Dupoy, ed., NATO Advanced Study Institute, Series E, Applied Sciences, No. 8, p. 389, Noordhoff International: Leyden, The Netherlands (1975).
9. W. J. Choyke, R. B. Irwin, J. N. McGruer, J. R. Townsend, K. Q. Xia, W. J. Doyle, B. O. Hall, J. A. Spitznagel and S. Wood, Proc. of the Thirteenth International Conference on Defects in Semiconductors, Coronado, CA, Edited by L. C. Kimerling and J. M. Parsey, Jr., p. 789 (1984).
10. W. J. Choyke, Proc. International Conf. on Radiation Effects in Semiconductors, 6-9 September 1976, Dubrovnik, Yugoslavia; Institute of Physics Conf. Series No. 31, p. 58 (1977).

11. R. S. Nelson, op. cit., Ref. 9.
12. P. J. Burnett and T. F. Page, J. Mat. Sci., 19: 845 (1984).
13. S. G. Roberts and T. F. Page, Ion Implantation into Metals, edited by V. Ashworth, W. A. Grant and R. M. Porter (Pergamon, Oxford, 1982), p. 135.
14. P. J. Burnett and T. F. Page, Proc. Brit. Cer. Soc., 34 (1984).
15. P. J. Burnett and T. F. Page, J. Mat. Sci. 19: 3524 (1984).
16. J. A. Spitznagel, Susan Wood, W. J. Choyke, N. J. Doyle, J. Bradshaw, and S. G. Fishman, Nucl. Instr. and Methods B16: 237-243 (1986).
17. Susan Wood, J. A. Spitznagel, W. J. Choyke, J. Bradshaw, J. Gregg, Jr., and N. J. Doyle, Mat. Res. Symp. Proc., Vol. 60, 459 (1986).
18. J. C. Mikkelsen, Jr., S. J. Pearton, J. W. Corbett, and S. J. Pennycook, Proc. of MRS Symposium on Oxygen, Carbon, Hydrogen and Nitrogen in Crystalline Silicon, Vol. 59 (1985).
19. E. P. Eernisse and S. T. Picraux, J. Appl. Phys. 48, 9 (1977).
20. P. J. Burnett and T. F. Page, submitted to J. Fab. Sci. (1984).
21. W. J. Choyke and Lyle Patrick, Phys. Rev. B4, 1843 (1971).
22. V. V. Makarov, T. Tuomi, K. Naukkarinen, M. Luomajavi, and M. Riihonen, Appl. Phys. Lett. 35, 922 (1979).
23. D. A. Thompson, M. C. Chan, and A. B. Campbell, Can. J. Phys. 54, 626 (1976).
24. V. V. Makarov, Sov. Phys. Solid State 13, 1974 (1972).
25. R. R. Hart, H. L. Dunlap, and O. J. Marsh, Rad. Eff. 9, 261 (1971).
26. A. Addamiano, G. W. Anderson, J. Comas, H. L. Hughes, and W. Lucke, J. Electrochem. Soc. 119, 1355 (1972).
27. R. B. Wright and D. M. Gruen, Rad. Eff. 33, 133 (1977).
28. R. B. Wright, R. Varma, and D. M. Gruen, J. Nucl. Mater. 63, 415 (1976).

29. A. B. Campbell, J. B. Mitchell, J. Shewchun, D. A. Thomson, and J. A. Davies, Silicon Carbide 1973, Proc. 3rd Int. Conf. on SiC, edited by R. C. Marshall, J. W. Faust, Jr., and C. E. Ryan (South Carolina Press, 1974), p. 486.
30. A. B. Campbell, J. Shewchun, D. A. Thomson, and J. B. Mitchell, in Ion Implantation in Semiconductors, edited by S. Namba (Plenum, New York, 1975).
31. H. G. Bohn, J. M. Williams, C. J. McHargue, and G. M. Begun, J. Mater. Res. 2, 107 (1987).
32. J. R. Patel and A. R. Chaudhuri, Phys. Rev. 143, 601 (1966).
33. R. F. Davis, H. J. Kim, J. W. Palmow, J. A. Edmond, H. Kong, and J. T. Glass, "Epitaxial Growth and Doping of and Device Development in Monocrystalline Beta-SiC Semiconductor Thin Films," in 1st Inter. Conf. on Amorphous and Crystalline SiC, Dec. 10-11, Washington, D.C. (1987).
34. Y. A. Vodakov and E. N. Mokhov, "Diffusion and Solubility of Impurities in Silicon Carbide," in Proc. of 1973 SiC Conference, University of South Carolina Press, Columbia, SC, p. 508 (1974).

APPENDIX A

ION BEAM MODIFICATION OF 6H/15R SiC CRYSTALS *

J.A. SPITZNAGEL **, Susan WOOD, W.J. CHOYKE ** and N.J. DOYLE

Westinghouse R&D Center, Pittsburgh, PA 15235, USA

J. BRADSHAW

Department of Physics, University of Pittsburgh, Pittsburgh, PA 15260, USA

S.G. FISHMAN

Office of Naval research, Arlington, VA 22203, USA

Large single crystals of silicon carbide consisting predominantly of 6H polytype have been implanted with hydrogen, nitrogen, or aluminum ions at 300 K. Rutherford backscattering-channeling techniques have been used to characterize atomic displacement effects resulting from implantation and postimplantation annealing at 573 K. Amorphization fluences for all three ions correspond to deposition of a critical damage energy of 2×10^{21} keV/cm². Annealing of N⁺ or Al⁺ implanted crystals for 0.5 h at 573 K produces appreciable recovery in damaged but crystalline regions. Defect annealing is inhibited in amorphous and heavily doped areas of the crystals.

I. Introduction

Composite materials are of considerable interest because of their excellent structural properties. Although the majority of composites now being used have organic matrices, much work is being carried out to develop carbon, metal and ceramic matrix composites for high temperatures and other operating environments too stringent for organics. In the past, materials scientists have concentrated their endeavors on composite processing and properties of the fiber and matrix, when developing a composite. Although the importance of the composite interfacial zone was recognized in this early work, model systems, such as silver reinforced with aluminum oxide, were chosen for the compatibility of fiber and matrix and the ease of load transfer from one constituent of the composite to the other [1]. More practical metal systems have matrices of common metals such as aluminum [2]. When using such matrices, special care has to be taken to avoid fiber degradation or to promote fiber wetting, depending upon the fiber/matrix combination. The high reactivity and strength of matrices such as aluminum, magnesium, titanium, nickel, etc, makes control of the interfacial zone more difficult

and makes it carry greater loads than in the model systems. In metal composites, conventional "wisdom" calls for a strong interfacial zone to insure stress transfer between fiber and matrix. An unfortunate ramification of such interfacial strength is low ductility, toughness, impact strength and crack propagation resistance.

In ceramic matrix composites, the goal has been to improve the material's toughness and resistance to impact and crack propagation. By fabricating composites such as graphite-reinforced glass ceramics, it has been possible to achieve order of magnitude enhancement of toughness in ceramic materials [3]. The key to this increased toughness has been attributed to low strength in the fiber-matrix interfacial zone which permits extensive fiber pullout and frictional sliding of the fiber along the matrix [4]. In ceramic composites where strong interfacial bonding is achieved, such toughness has not been observed.

One of the main advantages of composite materials, is the ability to tailor their properties for specific applications. For example, some structural applications call for a high level of vibrational damping. There is evidence that enhanced vibrational damping can occur at the interfacial zone in graphite-reinforced metal composites [5]. As advanced composite systems become closer to reality, it becomes critical to understand and learn to control interfacial zones. In order to tailor interfacial zones to achieve optimum composite mechanical properties and/or resistance to environmental degradation, it will probably be necessary to modify the

* Work supported in part by the Office of Naval Research under Contract No. N00014-85-C-0021 and by the National Science Foundation under Contract No. DMR84-03596.

** Also University of Pittsburgh.

surface of fiber reinforcement in a controllable manner.

The ability to change the near-surface structure, mechanical properties and, independently, the surface chemistry of composite reinforcements by ion beam modification offers a highly controllable and reproducible means of achieving superior matrix-fiber interfacial behavior. Additional merit from surface modification can be achieved by altering *processing parameters* which are sensitive to the nature of the surface of the fiber. Wetting, infiltration, and bonding are all fundamentally associated with the electronic states of the phases involved in an interface. Electron transfer across a particular interfacial zone establishes a contact potential, and the magnitude of that potential is thought to relate to the strength of the bond [6].

With ion beam modification, the bombarding ion, which can be reactive or inert, loses energy through electronic interactions and elastic collisions. The concentration profile and extent of the doped region in the surface can be altered independently and thus can produce marked changes in the microstructure, chemistry, and mechanical properties of the ion beam doped/damaged zone of the surface of the fiber. Consequently, ion beam modification is a flexible tool, which when combined with theoretical investigations, can provide valuable fundamental understanding of the nature of the interfacial zone in composite materials.

Since one of the most promising materials for fiber reinforcement in advanced composites is SiC, it is desirable to understand the nature of the physical and chemical modifications occurring when SiC crystals and fibers are subjected to ion beam bombardment. In this paper the irradiation effects associated with implantation of hydrogen, nitrogen and aluminum into high purity single crystals of 6H SiC are described. Selection of these species is based on previous observations of large changes in hardness and fracture behavior for hydrogen [7] or nitrogen [8] implanted Si or SiC. The effects of p-type or n-type dopant ions, e.g. Al or N, respectively, on damage production, annealing and chemistry of the near surface region is also of interest for composite materials applications.

2. Experimental procedures

Silicon carbide (0001) crystals were selected from two sublimation growth runs, D143 and D149 [9]. Transmission Laue photographs verified that the crystals were of mixed polytype but mostly 6H SiC. These samples are completely transparent, roughly 1 cm \times 0.5 cm and approximately 1 mm thick. They are compensated, slightly N-type, with an impurity concentration of $\approx 5 \times 10^{17}/\text{cm}^3$.

One face of each crystal parallel to the basal plane was lapped to 0.1 μm diamond finish. Both low load

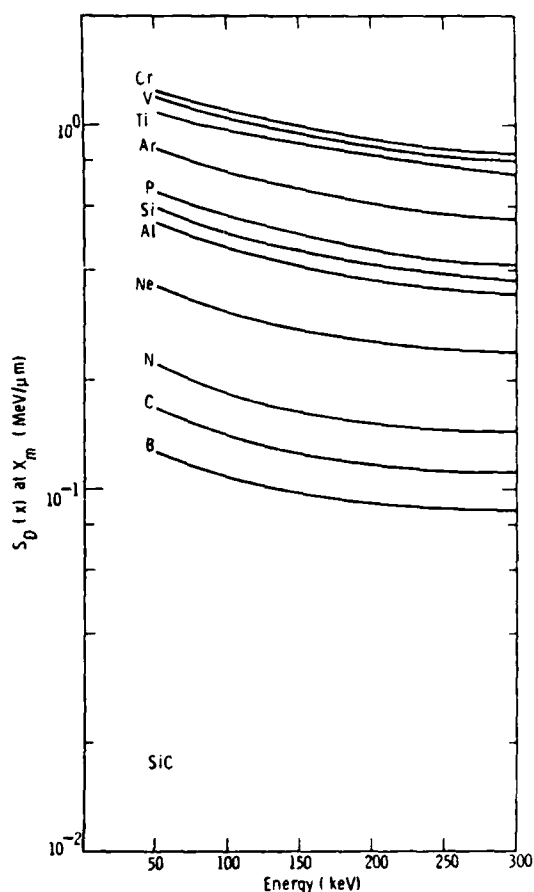


Fig. 1. Calculated damage energy per ion at the peak damage depth for various ions implanted into SiC at the energies indicated; EDEP-1 Code.

microhardness and Rutherford backscattering/channeling measurements on as-grown and as-polished crystal surfaces showed no significant debris layer effects. The basal plane, which is perpendicular to the hexagonal c axis, was cleaned with HF and solvents prior to implantation.

Each large crystal to be implanted was covered with a tantalum mask over less than one-half its area to provide a virgin-sample reference for the channeling measurements. Implants were made with a 200 kV implanter equipped with post acceleration magnetic mass separation. Samples were implanted at pressures of 10^{-7} Torr. A 1.5 MeV He beam from a 2 MV Van de Graaff was used to conduct the channeling experiments. Beam currents were normally 15 nA and the spot size was 0.8 mm. The beam divergence was normally less than 0.03 degrees and backscattering measurements were made at 168 degrees. Postimplantation annealing was conducted in vacuum at a pressure of 2×10^{-6} Torr.

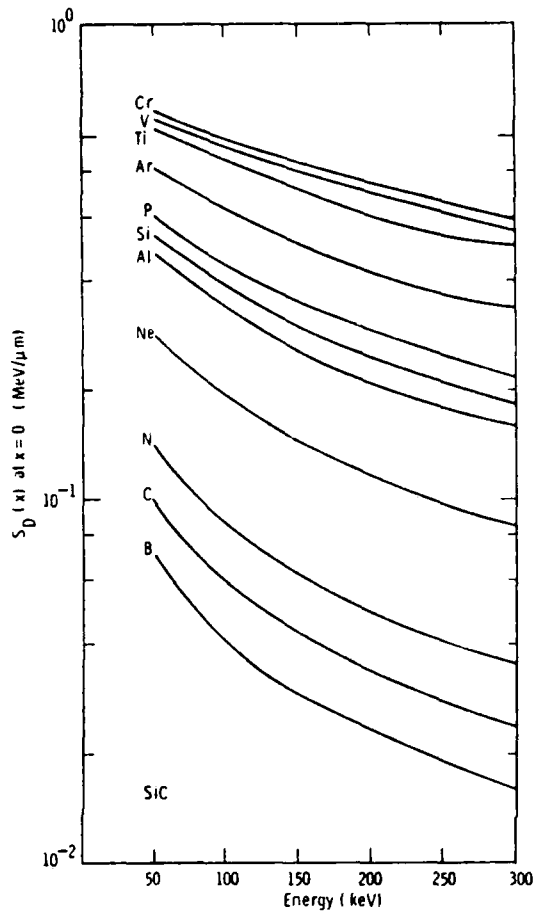


Fig. 2. Calculated damage energy per ion at the surface of SiC for various ions and energies indicated; EDEP-1 Code.

2.1. Calculation of deposited damage energy

Figs. 1 and 2 show the damage energy, $S_D(x)$, for various ions implanted into SiC as a function of incident ion energy. The curves were calculated using a modified version of the EDEP-1 [10] code. The damage energy (energy loss due only to atomic displacements) is shown for the surface ($x = 0$) and the peak damage depth ($x = X_m$). Accelerating voltages for the N and Al ions were chosen to produce peak damage at a depth of approximately 0.1 μm . The calculated $S_D(x)$ curves were then used to determine the fluences of 75 keV N^+ and 150 keV Al^+ required to produce equal numbers of displaced atoms in the SiC crystals. This results in different concentrations of implanted dopant and slightly different values of projected range, R_p . For the hydrogen implants, the incident ion energy (80 keV) had to be chosen so as to avoid an overlap of the Si and C backscattering peaks in the RBS measurements as described previously [11].

Table 1

Experimentally determined fluences required to produce amorphicity at the peak damage depth in hydrogen implanted silicon and silicon carbide ^{a1}

Material	Implantation temperature (K)	Fluence ions/cm ²	$S_D(X_m)^*$ (keV/cm ³)	DPA ^{b1}
Si	300	$> 10^{18}$	—	—
Si	95	8×10^{16}	1.1×10^{21}	0.59
SiC	95	8×10^{16}	2.0×10^{21}	0.34

^{a1} 50 keV H^+ into Si and 80 keV H^+ into SiC.

^{b1} Displacement energy $E_d = 25$ eV.

2.2. Amorphization criteria

Christel et al. [12] have suggested criteria for amorphization of crystalline silicon based on the total deposited damage energy. Above a critical value of $S_D(X_m)^* = 10^{21}$ keV/cm³, Si is rendered amorphous by implantation of ions with atomic mass equal to or greater than that of boron. This criterion corresponds to a displacement of approximately 10% of the lattice or 0.1 dpa for room temperature implantation in the absence of defect annealing. No general criteria are available for light ions such as H^+ or for compound covalently/ionically bonded ceramics with widely differing masses. Estimates of the value of $S_D(X_m)^*$ for hydrogen implanted Si and SiC were obtained from RBS measurements of the direct backscattering peak after implantation at 95 K and normalization with respect to the random spectrum as described in the following section. Table 1 summarizes the H^+ ion fluences and corresponding calculated values of $S_D(X_m)^*$ at which the normalized direct backscattering peak is equal to the backscattering from a randomly oriented crystal. In general it is not possible to assume that amorphization has occurred at this point since small atomic displacements on the order of 0.02 nm can block the channels. Bond distortions of this magnitude can result from incorporation of solute or crystalline phase transformations. Cross-section TEM has verified, however, that H^+ implantation into Si or SiC at 95 K does result in formation of amorphous phases [13]. It is not possible to drive Si amorphous with proton implantation at 300 K. Silicon carbide, however, can be amorphized by 80 keV H^+ ions at temperatures up to 1000 K [14].

Based on the results shown in table 1 we have assumed a critical deposited damage energy of 2×10^{21} keV/cm³ to estimate the fluences of N and Al ions required to produce an amorphous region at X_m and a amorphous zone extending from X_m to the front surface using the following equation:

$$\text{Critical fluence} = \frac{2 \times 10^{21} \text{ keV/cm}^3}{S_D(x) \times 10^7}$$

III AMORPHIZATION AND CERAMICS

Table 2

Implantation conditions and calculated fluences based on achieving amorphization at $S_D(x) = 10^{21}$ keV/cm³ ^{a)}

Condition	Fluence (ions/cm ²)	
	Nitrogen	Aluminum
No amorphicity	5×10^{14}	1×10^{14}
Amorphous at peak damage depth ($X = X_m$)	1×10^{15}	4.9×10^{14}
Amorphous from peak damage depth to surface	1.9×10^{15}	7.7×10^{14}
Beyond amorphicity	1×10^{16}	5×10^{15}

^{a)} 75 keV N⁺ or 150 keV Al⁺ into 6H SiC <100> at 300 K.

where $S_D(x)$ is given by figs. 1 and 2.

Table 2 summarizes these calculated values and the additional fluences chosen to produce doping beyond complete amorphicity and a damaged but crystalline microstructure for each ion.

3. Results and discussion

3.1. Damage production

As the fluence of N or Al ions increases, the channels of the SiC crystal are littered with displaced Si/C atoms and implanted dopant atoms. This disorder is expected to be at a maximum in a region centered either about the projected range, R_p , or the peak damage depth, X_m , depending on whether or not the damage is stabilized by the dopant atoms and whether the dopant atoms can diffuse at the implantation temperature. Because the concentrations of implanted N or Al atoms are small (< 1 at.%) the implanted atoms make a negligible contribution to the number of backscattered He ions. Hence, the observed backscattering is determined entirely by the distribution of displaced Si/C atoms. We denote by $\chi_R(x)$ that fraction of the He channeling beam which has been dechanneled when the sample is positioned in an aligned low index direction. The backscattered yield from such an aligned crystal divided by the backscattered yield from the same crystal in a randomly oriented position is denoted by $\chi(x)$. Following Rimini [15] the number of "equivalent displaced atoms" per unit volume, N_D , can be determined from

$$\frac{N_D(x)}{N_{SiC}^{Si}} = \frac{\chi(x) - \chi_R(x)}{1 - \chi_R(x)}$$

$N_D(x)$ represents the equivalent density of Si atoms (as seen by the channeled He ions) required to produce the observed direct backscattering. The divisor N_{SiC}^{Si} is the density of Si atoms in the SiC lattice.

While $\chi(x)$ is directly measured, the determination of $\chi_R(x)$ involves a numerical procedure [15]. For

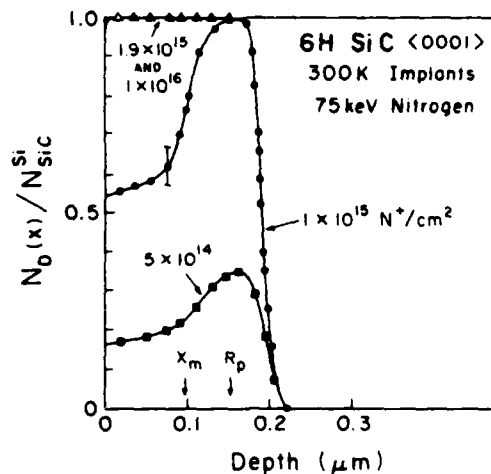


Fig. 3. Measured damage distributions for 75 keV N implants into 6H SiC <0001> at 300 K.

various fluences of 75 keV N ions and 150 keV Al ions figs. 3 and 4 show the resulting $N_D(x)$ distributions which we obtain in this manner for implantation at 300 K. The nitrogen ion fluence required to reach the random yield, $N_D(x)/N_{SiC}^{Si} = 1$, at $X = X_m$ agrees well with the calculated value, table 2. Similarly the fluence at which the saturated damage zone extends to the surface compares favorably with that based on depositing 2×10^{21} keV/cm³ into atomic displacements. The agreement between experimental and calculated values is slightly less satisfactory for the heavier Al ion.

In both fig. 3 and fig. 4 the low fluence damage region appears to be more closely centered on R_p than X_m . Similar results have been obtained for low tempera-

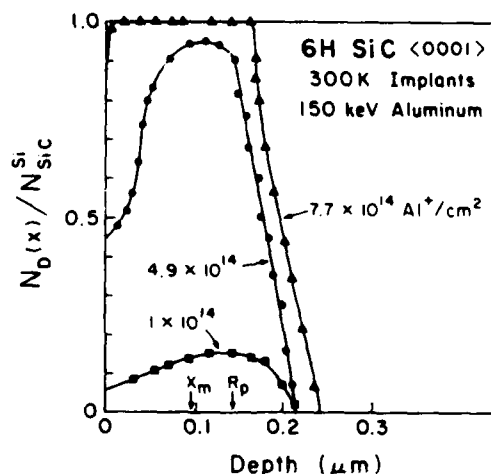


Fig. 4. Measured damage distributions for 150 keV Al implants into 6H SiC <0001> at 300 K.

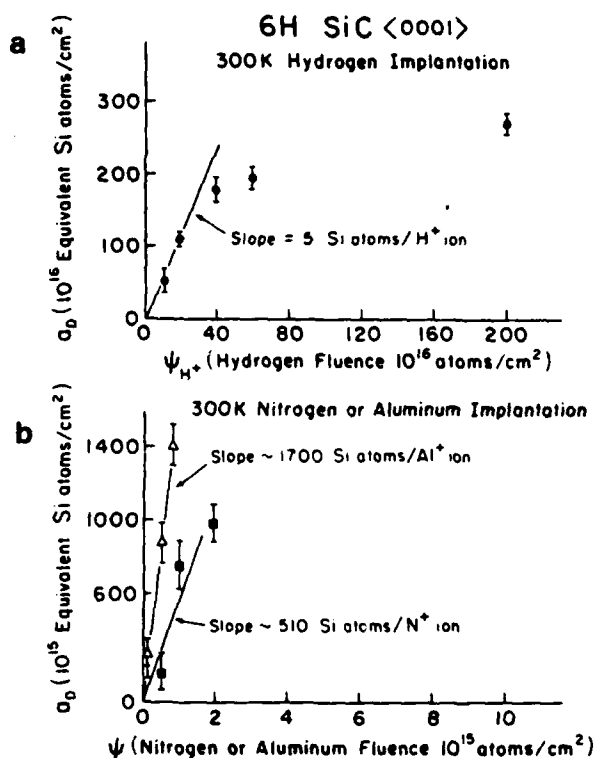


Fig. 5. The number of equivalent displaced Si atoms projected per unit area of the sample surface as a function of: a) hydrogen fluence [ref. 16] and b) nitrogen and aluminum fluences.

ture (< 1000 K) hydrogen implantation in 6H SiC [11] whereas in H-implanted Si, at temperatures where the hydrogen can diffuse and decorate its own damage, the $N_D(x)$ curves are centered around X_m [7]. This suggests that the implanted N and Al atoms are immobile but that they may stabilize the irradiation produced defects against recombination or annealing.

The integral of $N_D(x)$ will give the number of equivalent displaced atoms projected per unit area of the sample surface; this projected number we call a_D . Calculation of a_D has been described previously [7]. Fig. 5 shows the number of equivalent displaced Si atoms per unit area as a function of H, N and Al fluences. Fig. 5a was obtained from ref. [16]. Nitrogen ions are approximately 100 times more efficient and aluminum ions 340 times more efficient than protons in producing Si atom displacements in 6H SiC at 300 K. The position of the direct backscattering peak due to carbon introduces uncertainties in the normalization procedures required to obtain $N_D(x)$ for the carbon sublattice and this has not been attempted at present.

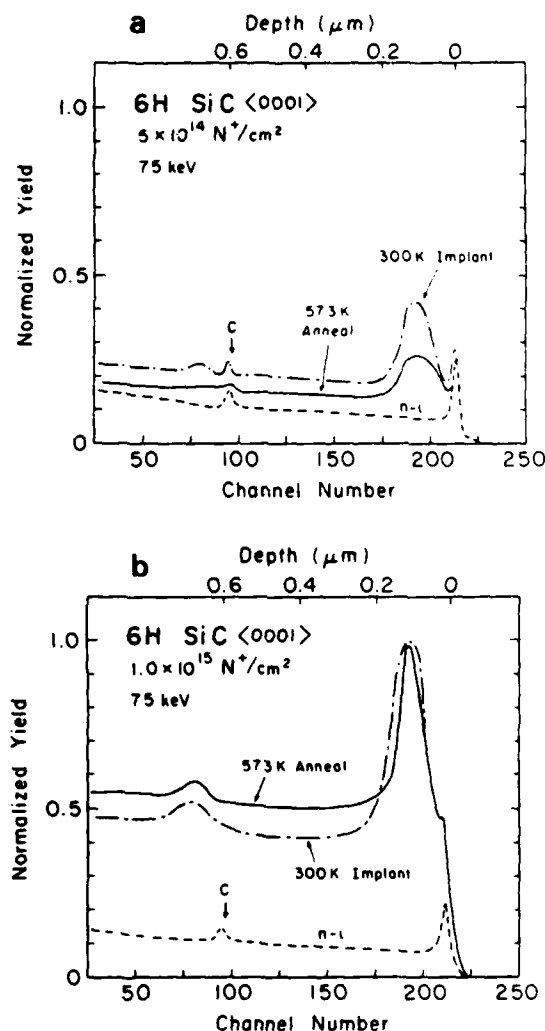


Fig. 6. Channeling spectra at a fixed fluence of implanted nitrogen in 6H SiC. Comparisons are made between an implant at 300 K and subsequent annealing at 573 K for a) $5 \times 10^{14} \text{ N}^+/\text{cm}^2$ and b) $1 \times 10^{15} \text{ N}^+/\text{cm}^2$.

3.2. Postimplantation annealing

RBS spectra for aligned, unimplanted (n-i), implanted, and annealed specimens are given in figs. 6 and 7. The backscattering yield from a randomly oriented crystal is not shown, but corresponds to a depth independent normalized yield of 1.0. Appreciable annealing of the low fluence (damaged but crystalline) SiC is observed. Estimates of the amount of recovery, based on reduction in the area under the direct backscattering Si peak, suggest that approximately 87% of the number of equivalent displaced Si atoms have been restored to lattice sites for the Al ion irradiated sample. Less re-

III. AMORPHIZATION AND CERAMICS

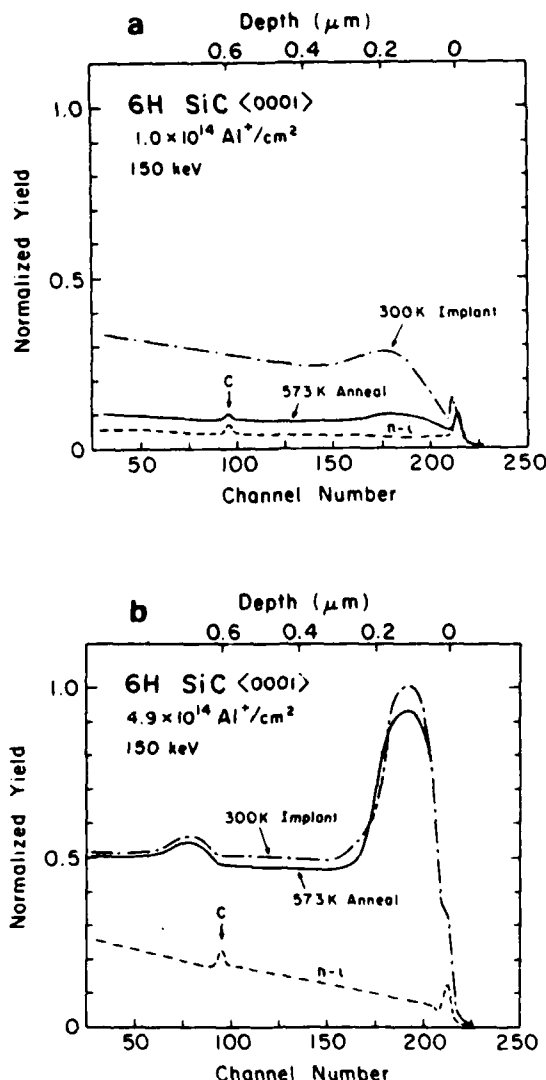


Fig. 7. Channeling spectra at a fixed fluence of implanted aluminum in 6H SiC. Comparisons are made between an implant at 300 K and subsequent annealing at 573 K for a) $1 \times 10^{14} \text{ Al}^+/\text{cm}^2$ and b) $4.9 \times 10^{14} \text{ Al}^+/\text{cm}^2$.

covery (approximately 40%) has occurred for the N ion bombarded crystal. Changes in the backscattering peaks for carbon, while difficult to detect, appear to parallel those for the Si peaks. Little recovery is seen for specimens where the direct backscattering peak reaches the random yield for both ions. This is in agreement with previous observations for 6H SiC implanted with hydrogen at low temperatures and suggests a lack of nuclei for regrowth of the crystalline structure [11].

4. Conclusions

Amorphization of 6H SiC crystals by implantation of H, N, or Al ions at 300 K requires the deposition of at least $2 \times 10^{21} \text{ keV/cm}^2$ of energy loss to atomic displacements. On the average, the equivalent number of displaced Si atoms projected per unit area of the sample surface is 5 per hydrogen ion, 510 per incident nitrogen ion and 1700 per incident aluminum ion. The damage regions from N or Al ion implantation at 300 K in 6H SiC are centered about a depth commensurate with the projected range of each ion. Post implantation annealing at 573 K results in appreciable recovery of irradiation damage from N or Al implantation at 300 K if the amount of deposited damage energy is less than the critical value.

References

- [1] W.H. Sutton, J. Chrone and A. Gatti, Development of composite structural materials for high temperature applications, Rep. 1-16, Contract Now-60-0465d (General Electric Co. 1960-64).
- [2] R.T. Pepper, R.C. Rossi, J.W. Upp and W.C. Riley, in: The room temperature mechanical behavior of aluminum-graphite composites (ASM, Cleveland, Ohio, 1970).
- [3] K.M. Prew and J.F. Bacon, in: Proc. of Second Int. Conf. on Composite Materials, Toronto, Canada (AIME, New York, 1978) p. 64.
- [4] D.B. Marshall and A.G. Evans, in: Failure mechanisms in ceramic-fiber/ceramic-matrix composites, Annual Report to Office of Naval Research, Contract N00014-81-K-0362 (1984).
- [5] M.S. Misra, Metallurgical characterization of the interfaces and the damping mechanisms in metal matrix composites, Progress Rept. No. 1, to Office of Naval Research, Contract N00014-84-C-0413 (1985).
- [6] H. Czichos, J. Phys. D5 (1972) 1890.
- [7] W.J. Choyke, R.B. Irwin, J.N. McGruer, J.R. Townsend, N.J. Doyle, B.O. Hall, J.A. Spitznagel and S. Wood, Nucl. Instr. and Meth. 209/210 (1983) 407.
- [8] S.G. Roberts and T.F. Page, in: Proc. 3rd Int. Conf. on Modification of Surface Properties of Metals by Ion Implantation, Manchester UK (Pergamon New York, 1982) p. 135.
- [9] W.J. Choyke, Inst. Phys. Conf. ser. no. 31 58/69 (1977) 58.
- [10] I. Manning and G.P. Mueller, Comput. Phys. Commun. 7 (1974) 85.
- [11] W.J. Choyke, R.B. Irwin, J.N. McGruer, J.R. Townsend, K.O. Xia, N.J. Doyle, B.O. Hall, J.A. Spitznagel and S. Wood, 13th Int. Conf. on Defects in Semiconductors (TMS-AIME, Coronado, CA, 1984) 789.
- [12] L.A. Chnstel, J.F. Gibbons and T.W. Sigmon, J. Appl. Phys. 52(12) (1981) 7143.
- [13] S. Wood, J. Gregg Jr, J.A. Spitznagel, N.J. Doyle, R.B. Irwin, J.R. Townsend and W.J. Choyke, Inst. Phys. Conf. Ser. No. 67 (1983) 247.

- [14] S. Wood, J. Gregg Jr, W.J. Choyke, J.A. Spitznagel, N.J. Doyle and R.B. Irwin, *Inst. Phys. Conf. Ser.* (1985) in press.
- [15] E. Rimini, in: *Materials characterization using ion beams*, eds. J.P. Thomas, A. Cachard, (Plenum, New York, 1978).
- [16] R.B. Irwin, *RBS/channeling analysis of hydrogen implanted single crystals of FZ silicon and 6H silicon carbide*, Ph.D. thesis, University of Pittsburgh (1984).

APPENDIX B

459

SURFACE MODIFICATION OF SiC BY ION IMPLANTATION

Susan Wood*, J. A. Spitznagel*, W. J. Choyke*, J. Bradshaw**,
J. Gregg, Jr.* and N. J. Doyle.*

*Westinghouse RAD Center, 1310 Reulah Road, Pittsburgh, PA 15235

**University of Pittsburgh, Pittsburgh, PA 15260

*Westinghouse RAD Center and University of Pittsburgh

ABSTRACT

Predominantly 6H <0001> SiC single crystals have been implanted with nitrogen and aluminum at 300°K. The effects of implantation and post-implantation annealing at 573-1173°K have been characterized by Rutherford backscattering/channeling, microhardness measurements and transmission electron microscopy. Even at 1173°K, defect annealing was inhibited in amorphized regions. Progressive damage recovery as the anneal temperature was increased was otherwise generally observed. Fluences predicted by the critical damage energy of 2×10^{-1} keV/cm² did not quite produce amorphization to $x = 0$. In the as-implanted specimens, decreasing hardness was observed with increasing fluence. Significant surface softening (~ 33% hardness reduction) was achieved at the highest aluminum fluence (5×10^{15} Al/cm²) and was stable at temperatures < 893°K.

INTRODUCTION

Ion implantation is an advanced processing technique currently being considered for particle, fiber and whisker surface modification. An obvious application of such modified materials is as the reinforcing phase in metal or ceramic matrix composites. Metal composites (MC) generally require a strong interfacial zone to ensure stress transfer between fiber and matrix. Unfortunately, such interfacial strength is often accompanied by low ductility, toughness, impact strength and crack propagation resistance. In ceramic composites (CC), the key to increased toughness has been related to low strength in the fiber-matrix interfacial zone. This permits extensive fiber pullout and frictional sliding of the fiber along the matrix [1]. Thus, in both types of composite systems, the understanding and ability to control the structure and properties of interfacial zones is critical to achieving optimum composite properties. Furthermore, since advanced fabrication schemes for both MC and CC often require liquid infiltration (e.g., of liquid metal for MC and sol gel processing for CC), fiber wettability is also an important factor. Both fabricability and mechanical properties of composites can be controlled by modification of the fiber surface.

Energetic ions deposit energy in a solid substrate via electronic interactions and elastic collisions which can selectively alter anion and cation sublattices. The concentration and damage profiles can be altered independently. Thus, ion beam modification provides a flexible means of fiber surface tailoring. The initial choice of this study was to perform experiments on single crystal specimens large enough to permit post implantation diagnostics in order to determine the nature of ion implantation (and post implantation anneal) induced structure changes. This understanding will then be applied to the problem of interfacial zone control in composite systems prior to large batch fiber implantation.

The selection of aluminum and nitrogen ions was made in part because previous work had shown that nitrogen implantation could introduce near surface plasticity in silicon and silicon carbide [2-5] while aluminum

implantation modified crack propagation behavior in silicon [4,5]. Similar observations were made in Al_2O_3 and MgO implanted with other species [4,5]. Additionally, Al and N are p- and n- type dopants, respectively, in SiC, plus Al is expected to more efficiently damage the Si sublattice whilst N should be more efficient in displacing carbon. The effects of implantation are assessed by a combination of Rutherford Backscattering (RBS)/Channeling, transmission electron microscopy (TEM) and microhardness measurements.

EXPERIMENTAL

Silicon carbide $\langle 0001 \rangle$ crystals were selected from the D149 sublimation growth run [6] and shown by transmission Laue patterns to be $> 95\%$ 6H SiC. All samples were completely transparent, but slightly yellow in color. Those utilized for RBS/channeling measurements were approximately $1 \text{ cm} \times 0.5 \text{ cm}$ and 1 mm thick. Crystal faces were lapped flat and parallel to the $\langle 0001 \rangle$ direction, with the face utilized for the implantation experiments having a 0.1 micron diamond finish. Separate TEM specimens were cut to approximately $2.5 \text{ mm} \times 2.5 \text{ mm}$ and were $< 1 \text{ mm}$ thick. No polishing and grinding procedures were performed on these samples. All crystals were cleaned thoroughly in HF followed by distilled water and solvent rinses prior to implantation.

Reference samples for the channeling studies were provided by placing a tantalum mask over $\sim 1/3$ specimen surface during implantation. TEM specimens were not masked. Implants were made at $\sim 295^\circ\text{K}$ and pressures of 10^{-7} torr with a 200 kV implanter equipped with post acceleration magnetic mass separation. Current densities were $0.5 \text{ } \mu\text{A}/\text{cm}^2$ and $0.25 \text{ } \mu\text{A}/\text{cm}^2$ for N and Al, respectively. A 1.5 MeV He beam from a 2 MV Van de Graaff was used to conduct the channeling experiments. Beam currents were normally 15 nA and the spot size was 0.8 mm , with a beam divergence of < 0.03 degrees. RBS measurements were made at 168° . Post-implantation annealing was performed at $300\text{--}900^\circ\text{C}$ ($573\text{--}1173^\circ\text{K}$) at a pressure of $2 \times 10^{-6} \text{ torr}$. The 1173°K temperature was selected as an upper anneal limit because it corresponds to possible processing temperatures for MC.

Implantation conditions and calculated fluences are listed in Table I. Accelerating voltages for the N and Al ions were chosen to produce peak damage at a depth of approximately $0.1 \text{ } \mu\text{m}$. The calculation of deposited damage energy and the amorphization criterion for SiC are discussed extensively by Spitznagel, et al., [7]. Fluences of 75 keV N^+ and 150 keV Al^+ were selected to produce equal damage levels in the SiC crystals. A critical deposited damage energy of $2 \times 10^{21} \text{ keV}/\text{cm}^3$ was used to calculate the fluences required to produce an amorphous region at x_m and an amorphous zone extending from x_m to the front crystal surface ($x = 0$). Additional fluences were chosen to produce doping beyond complete amorphicity and a damaged but crystalline microstructure for each ion.

Hardness indentations were obtained on a Tukon hardness tester calibrated for loads $> 10 \text{ g}$. A Knoop indenter was used with loads of $10\text{--}300 \text{ g}$. Initial measurements on as-polished crystals indicated no significant orientation dependence of the hardness so no fixed orientation was maintained. An additional check was performed on D149 $\mu\text{-}33$ ($5 \times 10^{15} \text{ Al}/\text{cm}^2$) after annealing at $900^\circ\text{C}/0.5 \text{ h}$ by taking measurements with the long diagonal of the indenter parallel to the $\langle 10\bar{1}0 \rangle$ and $\langle 12\bar{1}0 \rangle$ directions, but no hardness differences were detected. Actual KHN were calculated from micrographs of the indents taken on a Reichert optical microscope at $1000\times$ under constant illumination conditions by the same operator. Indents were too small to be accurately measured with the microscope/filar eye piece.

Table I
 Implantation Condition and Calculated Fluences Based
 on Achieving Amorphization at $S_D(x) = 10^{21}$ keV/cm³

Condition	Fluence (ions/cm ²)	
	Nitrogen	Aluminum
No Amorphicity	5×10^{14}	1×10^{14}
Amorphous at Peak Damage Depth ($x = x_m$)	1×10^{15}	4.9×10^{14}
Amorphous from Peak Damage Depth to Surface	1.9×10^{15}	7.7×10^{14}
Beyond Amorphicity	1×10^{16}	5×10^{15}

75 keV N⁺ or 150 keV Al⁺ into 6H SiC <0001> at 300°K.

attachment on the Tukon tester. Data are reported showing representative standard deviations. Indentations were placed towards the edge of the specimen so that adequate indent-free area remained for the RBS experiments.

Preparation of cross-section TEM specimens has been described previously [R]. Due to excessive edge milling effects in some samples, planar specimens were also prepared by thinning from the backside to the implanted surface using a procedure essentially identical to that used for cross-sections, apart from the use of a single ion gun in the milling process. All TEM studies were performed on a Philips 400T electron microscope operating at 120 kV.

RESULTS AND DISCUSSION

RBS/Channeling

RBS spectra for aligned, unimplanted (n-i), implanted and annealed specimens are given in Figures 1 and 2 for the nitrogen and aluminum implants, respectively. The backscattering yield from a randomly oriented crystal is not shown, but corresponds to a depth-independent normalized yield of 1.0. Since the concentrations of implanted N or Al atoms are small (< 1 At%) the implanted atoms make a negligible contribution to the number of backscattered He ions. Thus, the observed backscattering is determined entirely by the distribution of displaced Si/C atoms. Spitznagel, et al. [7] previously discussed the as-implanted curves in some detail and showed that the low fluence damage region is more centered upon R_0 than x_m . This suggests that the implanted N and Al atoms are immobile but that they may stabilize the irradiation produced defects against recombination or annealing. The nitrogen ion fluence required to reach random yield at $x = x_m$ agreed well with the calculated value, Table I. The fluence at which the saturated damage zone extends to the front surface (i.e., $x = 0$) was also comparable to that predicted by the amorphization criterion of $S_D(x) = 2 \times 10^{21}$ keV/cm³. For the heavier Al ion, agreement is reasonable but not as close as that for N.

Comparison of as-implanted and annealed spectra show that appreciable annealing has occurred in the low fluence implanted (damaged but crystalline) SiC after a 573°K/0.5h anneal (Fig. 1a, 2a). After a further anneal of 893°K for 0.5h significant recovery is also observed in the specimens implanted to produce amorphization at x_m (Fig. 1b, 2b).

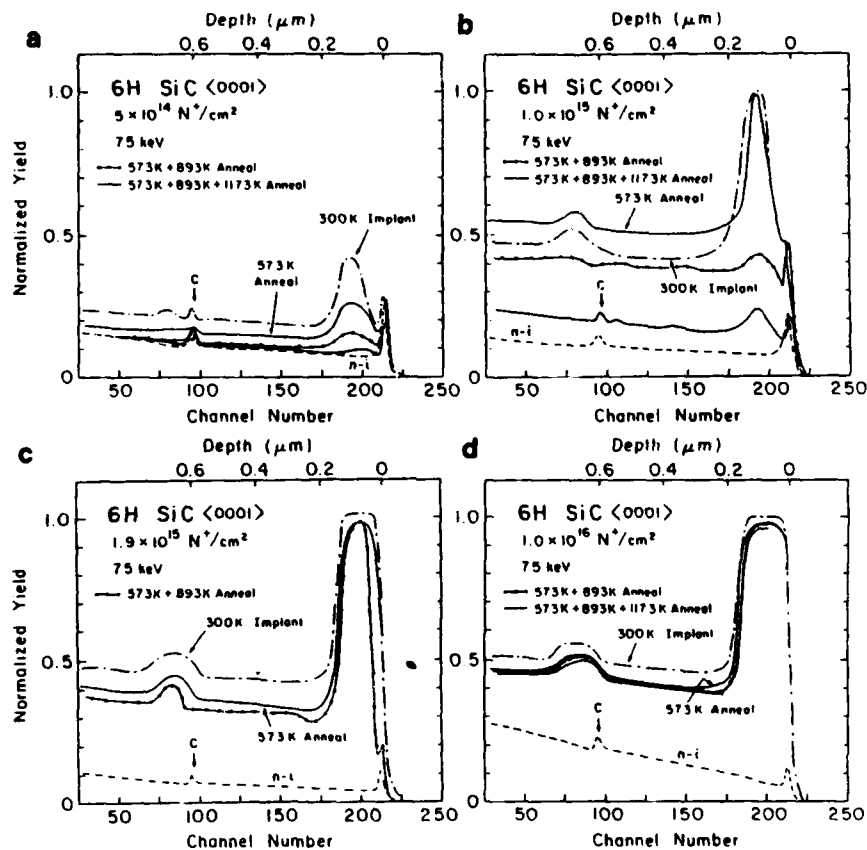


Figure 1 -- RBS/Channeling spectra from N-implanted and annealed SiC.

Dechanneling is further decreased after the 1173°K/0.5h anneal, but a small direct backscattering peak still remains. After the same 1173°K/0.5h anneal, the lowest fluence Al implant appears to show total damage recovery (not shown), whilst the spectrum from the N-implanted specimen ($5 \times 10^{14} \text{ N}^+/\text{cm}^2$) is approaching that of the non-implanted crystal (Fig. 1a). For the higher fluence implants, such dramatic recoveries are not observed. Spectra obtained from specimens implanted to fluences calculated to produce amorphization at $x = 0$ do show a progressive narrowing and intensity decrease of the direct backscattering peak, as the anneal temperature is increased (Fig. 1c, 2c). The results indicate that annealing is progressing from both the front and back of the highly damaged region and may, therefore, suggest the presence of a very narrow residual crystalline layer at the front surface after implantation. In contrast, the highest fluence implants show no recovery at $x = 0$, only a marginal reduction in the direct backscattered intensity, and minimal recovery at the back of the damaged zone (Fig. 1d, 2d). The lack of recrystallization at $x = 0$ is probably related to the lack of residual single crystal "seed".

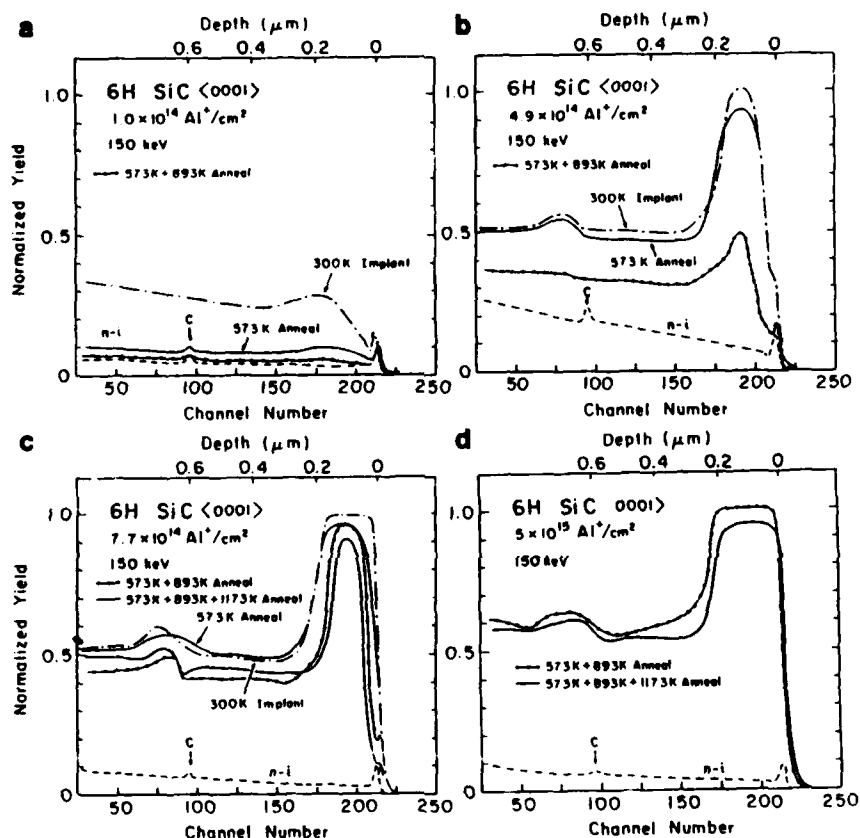


Figure 2 -- RBS/Channeling spectra from Al-implanted and annealed SiC.

It is interesting to note that after annealing the highest fluence Al-implanted specimen at 1173°K, an aluminum deposit was observed on the slightly cooler end of the porcelain boat used to hold the SiC sample. Carter [9] has reported similar (ion-implanted) solute rejection from SiC, but at much higher temperatures. The aluminum film thickness was sufficient to account for most of the originally implanted Al. Similar out-diffusion of Al may have occurred while annealing the lower fluence specimens. These observations suggest that aluminum stabilized defects are not responsible for the direct backscattering observed in the specimens implanted to $7.7 \times 10^{14} \text{ Al}^+/\text{cm}^2$ and $5 \times 10^{15} \text{ Al}^+/\text{cm}^2$ after the 1173°K anneal.

Microhardness Measurements

In previous work by Roberts and Page [3], microhardness data were standardized to a chosen indentation diagonal length using the Meyer analysis. The approach addressed the issue of measuring hardness on a

composite specimen consisting of a thin surface layer and a substrate expected to have differing mechanical responses. This methodology was considered but not applied to the data obtained in this study because the depth of the damaged zone was $< 0.24 \mu\text{m}$. This is smaller than the indent depths produced by using a 25 gm load which was the smallest load yielding measureable indent diagonals (10 gm load indents could not be photographed sufficiently well, presumably because of their shallow depth, $\sim 0.15 \mu\text{m}$). Thus, the hardness data reported herein always reflect a combination of both implanted layer and substrate properties.

Knoop hardness numbers obtained using a 50 gm load are plotted as a function of ion fluence in Figures 3a, b. Unimplanted reference data are included for comparison. Utilization of a 25 gm load produced similar trends in hardness change, but incompleteness of the data precluded its incorporation here. Figure 3c presents hardness obtained from the Al-implanted SiC using a 200 gm load, which samples a much larger substrate volume. Some evidence of the trends apparent in Figure 3a are still present, but in general, the hardness values are universally converging towards the unimplanted reference values, as expected.

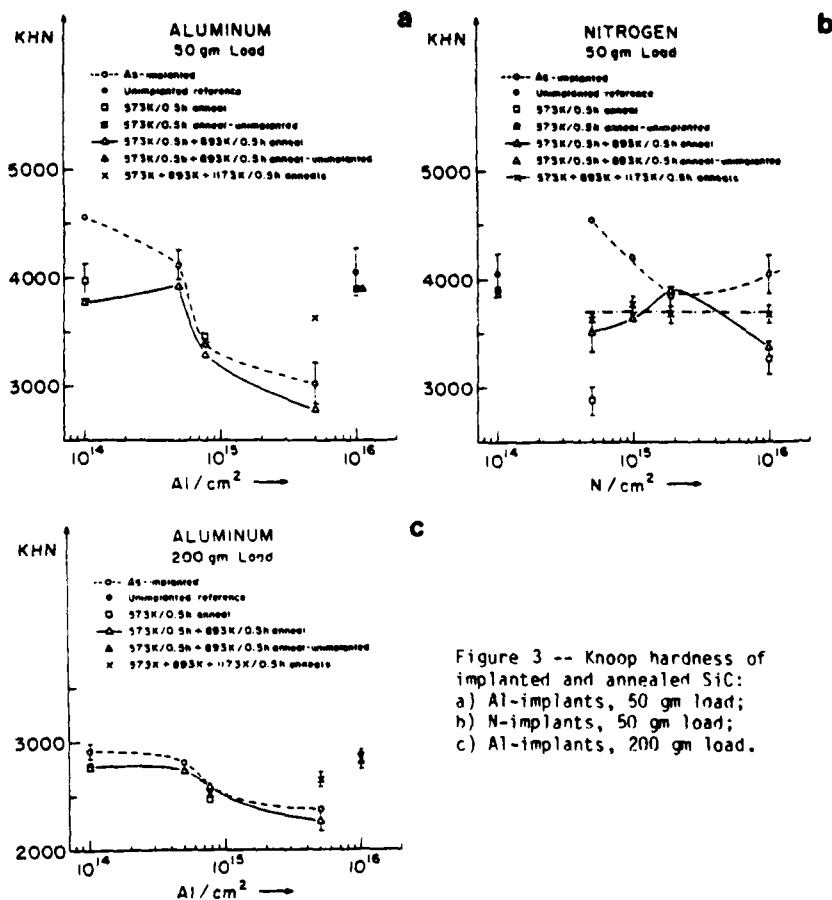


Figure 3 -- Knoop hardness of implanted and annealed SiC:
 a) Al-implants, 50 gm load;
 b) N-implants, 50 gm load;
 c) Al-implants, 200 gm load.

SiC implanted with Al shows an initial increase in surface hardness followed by a decrease over the fluence range corresponding to the development of a highly damaged and predominantly amorphous surface layer. The N-implanted SiC exhibits similar, but smaller hardness changes. These results are contrary to those reported previously [3] where significant changes in hardness were observed only for fluences $> 4 \times 10^{17} \text{ N}_2/\text{cm}^2$ (80 keV). These latter implantations were performed with an estimated substrate temperature of 300°C. The 300°C annealing behavior reported in this paper suggests that, at low fluences, the as-implanted damage may be different for the two sets of experiments.

Annealing of the low fluence N and Al implanted specimens produces a hardness decrease which may be related to the recovery observed in the PRR data. It is not understood why the 573°C/0.5h anneal yields ~ 33% decrease in hardness in the $5 \times 10^{14} \text{ N/cm}^2$ SiC sample which then increases after the subsequent 893°K anneal. Both values are below the non-implanted reference hardness, whereas the low fluence Al hardness recovers to the unimplanted reference value. All other annealed Al implants show no significant hardness change, with the exception of the $5 \times 10^{15} \text{ Al/cm}^2$ specimen annealed at 1193°K. Its hardness increase may correlate with the observed out-diffusion of aluminum. Up to 873°K, however, the structure(s) responsible for the hardness decrease in SiC implanted with 7.7×10^{14} and $5 \times 10^{15} \text{ Al/cm}^2$ appear stable.

Annealing behavior of the N-implanted specimens shows a general trend towards a constant hardness independent of implantation fluences after the 1173°K anneal. This hardness value is somewhat below unimplanted SiC reference hardness. At the lower temperature anneals, some softening was observed in the highest fluence specimen at loads $< 50 \text{ gm}$. At higher loads, indentation produced severe exfoliation and cracking not observed in the high fluence Al specimen. Indent morphologies are similar to those which have been recorded for higher fluence H-implanted SiC (e.g., Figure 4). The data clearly suggest the development of different microstructures during the intermediate temperature anneal. Further TEM studies are in progress to elucidate this issue.

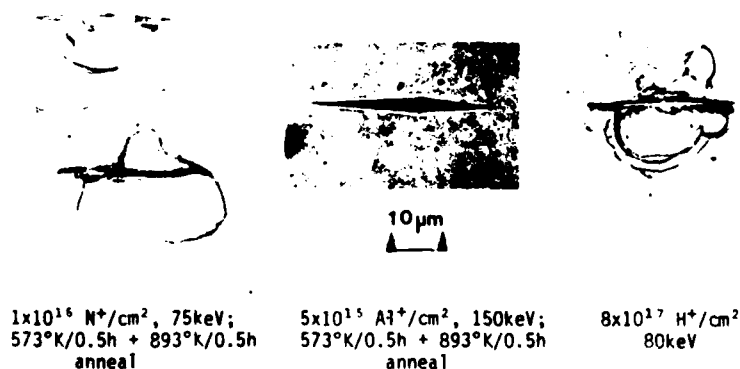


Figure 4 -- Optical micrographs of Knoop hardness indentations obtained using a 200 gm load.

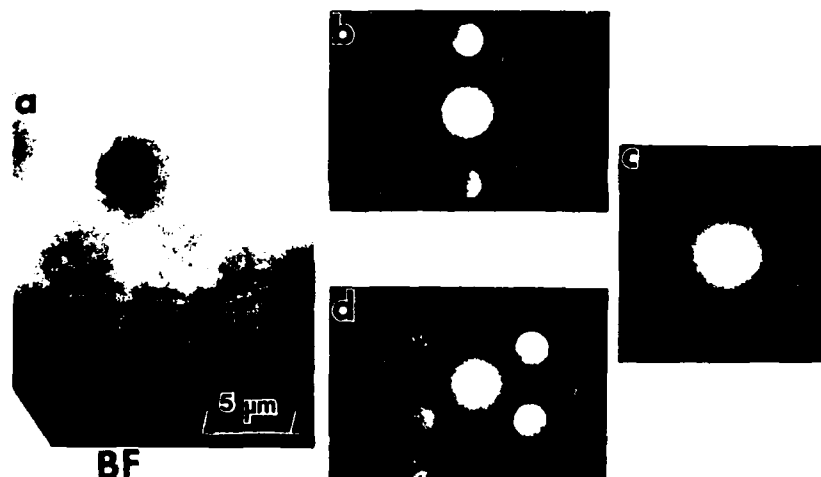


Figure 5 -- Low Magnification BF TEM micrograph (a) and μ SAO patterns from (b) near surface crystalline region; (c) predominantly amorphous region extending almost to the front surface and (d) thicker region showing bend contours. As-implanted specimen, 7.7×10^{14} Al/cm².

Transmission Electron Microscopy

TEM analysis of the SiC specimen implanted with 7.7×10^{14} Al/cm² is presented in Figure 5. By obtaining μ SAO patterns at various foil thicknesses it was determined (a) that a very thin (probably < 10 nm) residual crystalline layer was still present at the front surface and (b) that the remainder of the implanted layer is predominantly amorphous. The bend contours indicate the transition to thicker, unimplanted crystal. These observations indicate that the saturated damage zone, predicted by the amorphization criterion of $S_D(x) = 2 \times 10^{21}$ keV/cm³ did not quite extend to $x = 0$.

Figure 6 shows a XTEM micrograph of the 1×10^{15} N/cm² implant after annealing at 573°K and 893°K for 0.5h. This fluence was calculated to produce amorphization at $x = x_m$. After the anneal, the entire damage zone is crystalline, although the crystal quality is poorer than that of the virgin SiC. Residual black spot damage, similar to that observed after hydrogen implantation in SiC [10] is present.



Figure 6 -- XTEM micrograph of 6H <0001> SiC implanted to 1×10^{15} N⁺/cm² and annealed at 573°K and 893°K for 0.5h. μ SAO is from the residual damage zone.

SUMMARY

The agreement between RBS/Channeling data and predicted implantation state of the single crystal SiC indicates that the damage structure development can be reasonably well predicted. However, additional TEM studies are required for a more complete understanding of the microstructures formed and the RBS data are being analyzed to determine specific sublattice recovery effects. The observed microhardness changes suggest that ion beam processes can cause near surface mechanical property changes at relatively low ion fluences and doping. Stability of such property changes, with respect to composite processing temperatures, for example, requires further investigation--the present data show a progressive recovery with increasing temperature. Activation energies for recovery will be obtained by considering the areas under the direct RBS peaks. Hardness indentation produces complex states of stress and material deformation. Interpretation of the hardness data in terms of the SiC/composite matrix property changes and the flow and fracture behavior of the SiC reinforcing phase needs additional study, culminating in the testing of composites fabricated with ion-implanted fibers.

REFERENCES

1. D. B. Marshall and A. G. Evans, Annual Report to ONR, Contract N00014-81-K-0367, January 1, 1984-December 31, 1984.
2. P. J. Burnett and T. F. Page, J. Mat. Sci. 19, 845 (1984).
3. S. G. Roberts and T. F. Page, *Ion Implantation into Metals*, edited by V. Ashworth, W. A. Grant and R. M. Porter (Pergamon, Oxford, 1982), p. 135.
4. P. J. Burnett and T. F. Page, Proc. Brit. Cer. Soc. 34, (1984).
5. P. J. Burnett and T. F. Page, J. Mat. Sci. 19, 3524 (1984).
6. W. J. Choyke, Inst. Phys. Conf. Ser., No. 31 (1977). p. 58.
7. J. A. Spitznagel, Susan Wood, W. J. Choyke, N. J. Doyle, J. Bradshaw and S. G. Fishman, to be published in J. Nucl. Instr. and Meth. (1986).
8. Susan Wood, J. Gregg, Jr., J. A. Spitznagel, N. J. Doyle, R. B. Irwin, J. R. Townsend and W. J. Choyke, Inst. Phys. Conf. Ser. No. 67 (1983) p. 247.
9. C. H. Carter, Jr., J. A. Edmond, J. W. Palmour, J. Ryu, H. J. Kim and R. F. Davis, Mat. Res. Soc. Symp. Proc., Vol. 46 (1985) p. 593.
10. S. Wood, J. Gregg, Jr., W. J. Choyke, J. A. Spitznagel, N. J. Doyle and R. B. Irwin, Inst. Phys. Conf. Ser. No. 76 (1985) p. 139.

ACKNOWLEDGMENTS

The authors wish to thank J. Ruan for assistance with the RBS/channeling experiments. This work was supported in part by the Office of Naval Research under Contract No. N00014-85-C-0021 and by the National Science Foundation under Contract No. DMR 84-03596.